論文 / 著書情報
Article / Book Information

題目(和文)	
Title(English)	Molecular Design of Bent-Shaped Dimeric Molecules to Adapt Low Temperature Ferroelectric Phase with High Spontaneous Polarization and Dielectric Strength
著者(和文)	中杉茂正
Author(English)	Shigemasa Nakasugi
出典(和文)	学位:博士(工学), 学位授与機関:東京工業大学, 報告番号:甲第12579号, 授与年月日:2023年9月22日, 学位の種別:課程博士, 審査員:柘植 丈治,曽根 正人,石崎 博基,戸木田 雅利,林 智広,CHANG TSO-FU
Citation(English)	Degree:Doctor (Engineering), Conferring organization: Tokyo Institute of Technology, Report number:甲第12579号, Conferred date:2023/9/22, Degree Type:Course doctor, Examiner:,,,,,
学位種別(和文)	博士論文
Type(English)	Doctoral Thesis

Molecular Design of Bent-Shaped Dimeric Molecules to Adapt Low Temperature Ferroelectric Phase with High Spontaneous Polarization and Dielectric Strength

Doctor of Engineering

Department of Materials Science and Engineering,

Tokyo Institute of Technology

Shigemasa Nakasugi

2023

Table of Contents

CHAPTER 1

General Introduction

1.1. Liquid Crystals (LCs)

When most people hear the word of the liquid crystals (LCs), they think of LC televisions. In addition to LC televisions, LC displays have been adopted and widely used in devices such as mobile phones, laptop computers, automobiles, and other scientific equipment. LCs are recognized as a new fourth state of matter apart from the solid, liquid, and gaseous three states of matter. LCs are roughly classified into lyotropic LCs formed by dissolving in a solvent and thermotropic LCs formed at various temperatures. In this thesis, the thermotropic LCs is focused because the thermotropic LCs are dealt with. Thermotropic LCs come in a wide variety of forms. A solid, i.e., crystal (Cr) phase has three-dimensional order of molecules, and a liquid, i.e., isotropic (Iso) phase has no order at all in all directions. The LC phases exist between the Cr phase and the Iso phase, and the transition mainly from the 3 dimensional (D) order to the 0 D order involves a transition from 3 D → 2 D → 1 D → 0 D and a transition from 3 D → 1 D → 0 D. There are various transitions from the 3 D order to the 0 D order, and various LC phases exist depending on the intermediate state. Figure 1-1(a) shows a typical rod-shaped LC

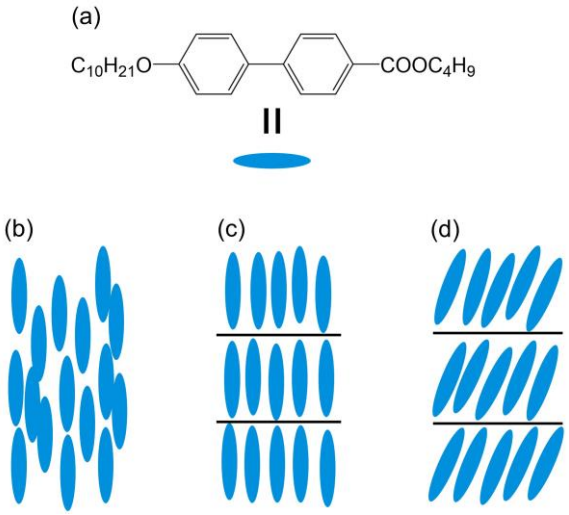

Figure 1-1. (a) Molecular structure of rod-shaped LCs. Schematic view of representative LC phases; (b) nematic, (c) SmA, and (d) SmC phases.

molecular structure.[1] This rod-shaped molecule is composed of a mesogenic group, which is a hard segment, and an alkyl chain, which is a soft segment, and forms various LC phases. Figure 1-1(b)-(d) show typical alignment structure of this rod-shaped molecule. The Cr phase with 3 D order transforms into the smectic-C (SmC) and smectic-A (SmA) phases with 1 D positional order as the temperature increases. Here, the smectic phase is classified into the SmC phase in which the molecules are tilted from the direction perpendicular to the plane of each layer and the SmA phase in which the molecules are perpendicular to each layer. Furthermore, with increasing temperature, a nematic (N) phase with a loss of positional order appears. There are various other LC phases such as the discotic and cubic phases, and all of which appear in the process of transition from 3 D order in the Cr phase to 0 D order in the Iso phase.[2]

1.2. Ferroelectric LCs

Among the LCs described above, there is a special LC having ferroelectricity. The ferroelectricity is a state in which spontaneous polarization (P_s) exists in a system in a state in which no external electric field is applied, and the P_s can be reversed by electric field reversal. Here, LCs with ferroelectricity are classified and their characteristics are explained.

1.2.1. Rod-Shaped Molecules

1.2.1.1. Chiral Smectic C (SmC*) Phase

The first ferroelectric LC was discovered by R. B. Mayer et al.[3] in 1977. Mayer et al. proved that DOBAMBC (see Figure 1-2(a)) with chiral molecules introduced into the molecule can become ferroelectric by consideration of symmetry. Although the symmetry of the normal SmC phase is C_{2h}, the symmetry of the SmC* phase into which chiral molecules are introduced is C_2, and the molecular long axis is aligned with a uniform tilt from the layer normal. Furthermore, there is the P_s derived from the dipole moment because the free rotation around the long axis of the molecule is constrained (see Figure 1-2(b)). In the absence of an external electric field,

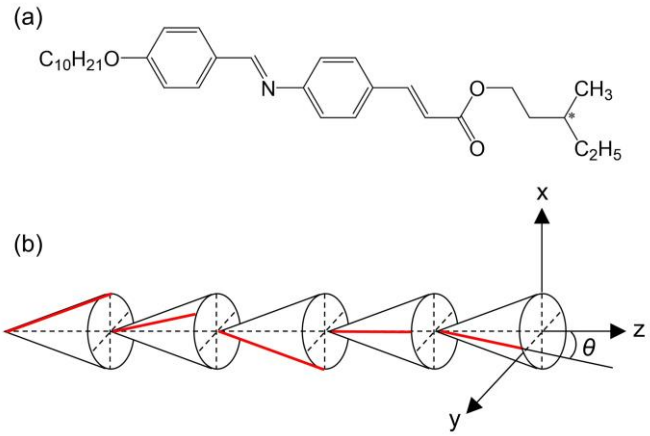

Figure 1-2. (a) Molecular structure of DOBAMBC. (b) Schematic view of representative SmC* phase. The z is the layer normal.

this ferroelectric phase forms a helical structure whose axis is the direction of the layer normal, resulting in cancellation of the P_s. However, once an electric field is applied, a state of aligned dipole moments is formed, and this state is maintained even when the electric field is turned off.

1.2.1.2. Ferroelectric nematic (N_F) phase

The interest has also been devoted on ferroelectricity in the nematic phase, the most common phase in rod-shaped LCs. Ferroelectricity is produced by the dipolar-dipolar interaction. According to the simple model by Born, the electric–dipolar interaction proportional to the square of the dipole moment, which should be strong enough to withstand a thermal fluctuation, is the most important to emerge from the nematic phase.[4] Similar theoretical predictions have been studied by Lee et al.[5] The nematic phase becomes ferroelectric when the rod-shaped molecule has a large dipole moment exceeding a certain critical magnitude along its long axis. This prediction has been first realized in the hard-rod polymers where the longitudinal dipole moment can be easily increased with the degree of polymerization. A typical example is the aromatic LC polyester, so-called "Vectra," created by the polycondensation of hydroxyl benzoic acid and hydroxyl naphthoic acid (see Figure 1-3(a)). This polymer exhibits the extremely strong second harmonic generation (SHG) in nematic LC state and its glassy solid state, showing the formation of non-centrosymmetric polar nematic LC.[6,7] As predicted from the theory[5], it is reported that the SHG-active LC is formed only when the degree of polymerization exceeds a critical value of around 40, that is the longitudinal dipole moment of polymer exceeds 100 D.[7] Similar SHG-active nematic and cholesteric LCs are also observed in the α-helical polypeptides which behave as dipole rod as well.[8,9]

More recently, two independent reports in the low-weight molecular system were published claiming the discovery of a ferroelectric nematic phase (N_F) for two quite different molecular

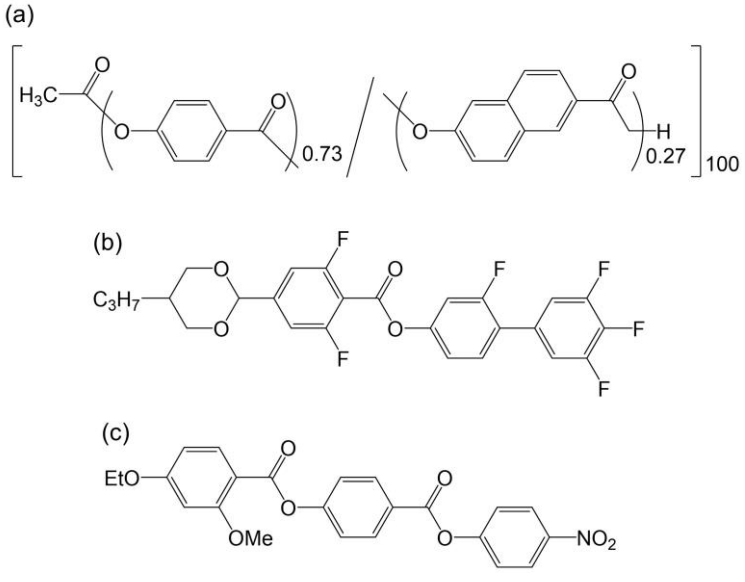

Figure 1-3. Molecular structure of (a) Vectra, (b) DIO, and (c) RM734.

structures, DIO[10] (see Figure 1-3(b)) and RM734[11,12] (see Figure 1-3(c)) with high longitudinal dipole moments (about 10 D). Furthermore, several other molecules and their ferroelectric properties are intensively studied.[13-20]

1.2.2. Bent-Shaped Molecules

1.2.2.1. Banana Molecules

Apart from the SmC* and N_F phases, which are the rod-shaped molecules as mentioned above, Watanabe et al. first discovered the ferroelectric switching characteristics of the banana molecules without asymmetric carbon molecules.[21] The banana molecules are constructed by linking the linear mesogens to the non-para-positions of aromatic central core.[21-25] A typical molecular structure, P-*n*-O-PIMB is shown in Figure 1-4(a). The banana molecules with polarization perpendicular to the long axis of the molecule form a layered structure, which suppresses free rotation around the long axis due to molecular packing. Therefore, the

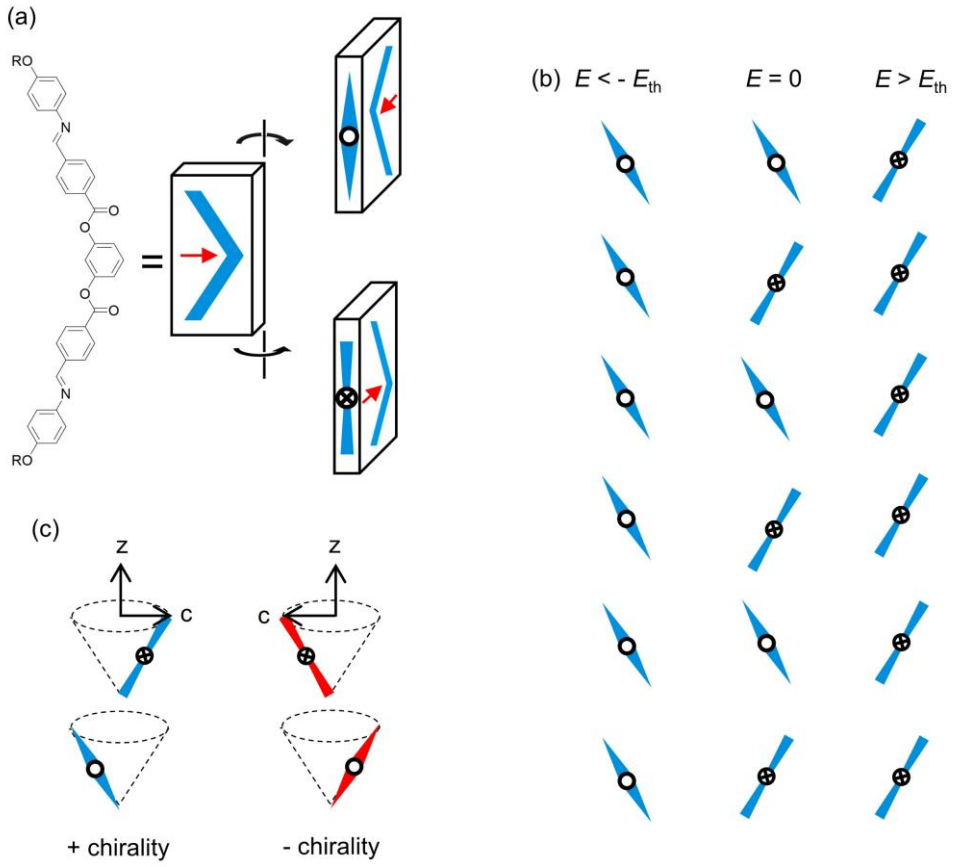

Figure 1-4. (a) Molecular structure of the banana molecule, P-*n*-O-PIMB (left) and its symbolic representation (right). Red arrows represent the bent-director (i.e. polar axis). (b) Layer organization in the $SmCP_A$ phase showing the antiferroelectric homogeneously chiral states at zero applied electric field ($E = 0$) and the corresponding ferroelectric states for fields beyond the threshold electric field (E_{th}). (c) Chirality of the SmCP phase. The z is the layer normal and the c is the molecular tilt orientation between adjacent layers.

polarization generated by the anisotropy of the molecular shape and the effective packing (polar structure) produce ferroelectricity or antiferroelectricity. If this intralayer polarization is parallel to the adjacent layer, it is ferroelectric, and if it is antiparallel, it exhibits antiferroelectricity. The phase structure model of P-*n*-O-PIMB is concluded to be an antiferroelectric phase in which the molecules are tilted from the layer normal as shown in Figure 1-4(b).[26] The chirality

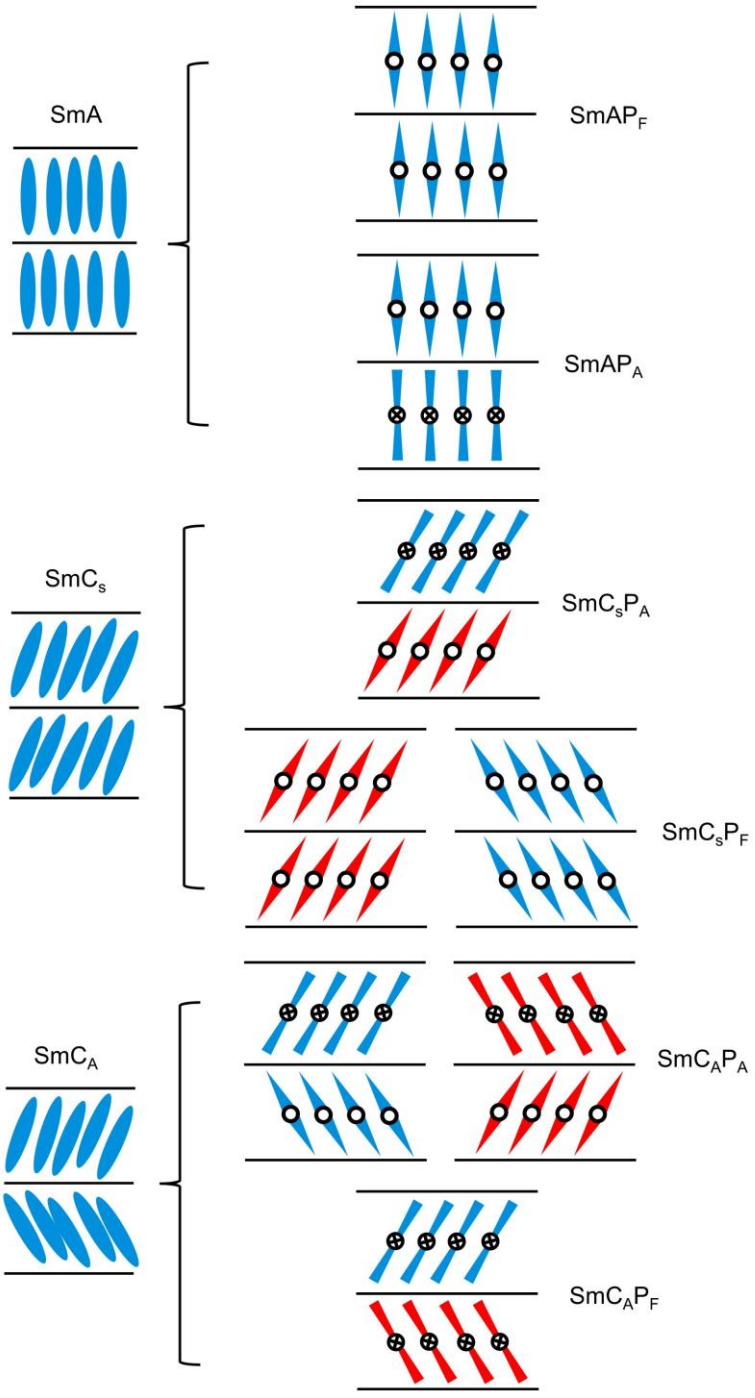

Figure 1-5. Six possible polar smectic structure of bent-shaped molecules. In two of them, molecules are not tilted from the smectic layer normal (SmAP) and another four are tilted polar smectic phases (SmCP) in which two types of layers consisting blue or red molecules which is mirror images of the other.

occurs as a result of molecules being tilted from the layer normal because molecules have the P_s due to shape anisotropy (see Figure 1-4(c)). In principle this polar packing occurs in both the non-tilted SmA and tilted SmC phases. There are six possible layer structures, "$SmAP_F$, $SmAP_A$, SmC_SP_A, SmC_SP_F, SmC_AP_A, and SmC_AP_F phases" consisting of polar packed smectic layers with achiral bent-shaped molecules (see Figure 1-5).[26–30] These structures are characterized by their layer structure and molecular orientation, in other words, clinicity and polar order. The Sm-A denotes the phase with layers in which molecules tend to align their long axis along the layer normal direction. The SmC phase denotes the phase with smectic layers in which molecules tend to align their long axis tilted with respect to the layer normal direction. The notation C_S and C_A which defines clinicity between two adjacent smectic layers in SmC type phase refers respectively to synclinic and anticlinic tilt. To denote the polar order, P_F and P_A refer respectively to ferroelectric and antiferroelectric polar order in adjacent layers. Furthermore, due to its special molecular shape, banana molecules can form various smectic and N_F phases other than the above smectic phases.[23,31] Banana molecules can produce unique LC phases that rod-shaped molecules never form.

1.2.2.2. Dimeric Molecules

The banana molecules have the phenyl group in the center of the molecule, whereas the molecule in which the central spacer is linked by a methylene chain is called a dimeric molecule.[32-37] The dimeric molecules were synthesized and structurally analyzed at the same time as the banana molecules. The odd-even effect in the methylene chain length of the spacer forms bent and rod-shaped shapes, respectively.[32,33,38] Assuming that the methylene chains are all-trans oriented, when the number of methylene chains is odd, adjacent mesogens tilt in opposite directions to the layer normal, resulting in the formation of a bent structure (see Figure 1-6(a)). When the number of carbon atoms in the methylene chain of the spacer is even, the molecule becomes rod-shaped (see Figure 1-6(b)) and does not exhibit ferroelectricity or antiferroelectricity. The LC phase forms a nematic or SmA phases. The typical bent-shaped

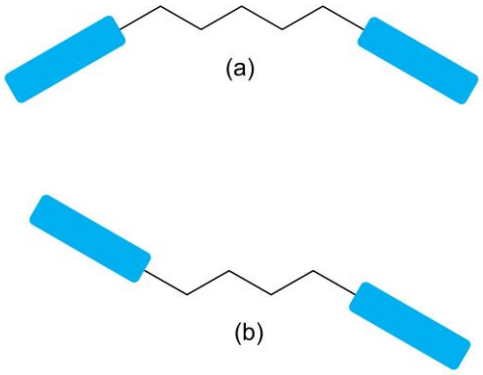

Figure 1-6. Molecular conformation of (a) odd-numbered molecule and (b) even-numbered one.

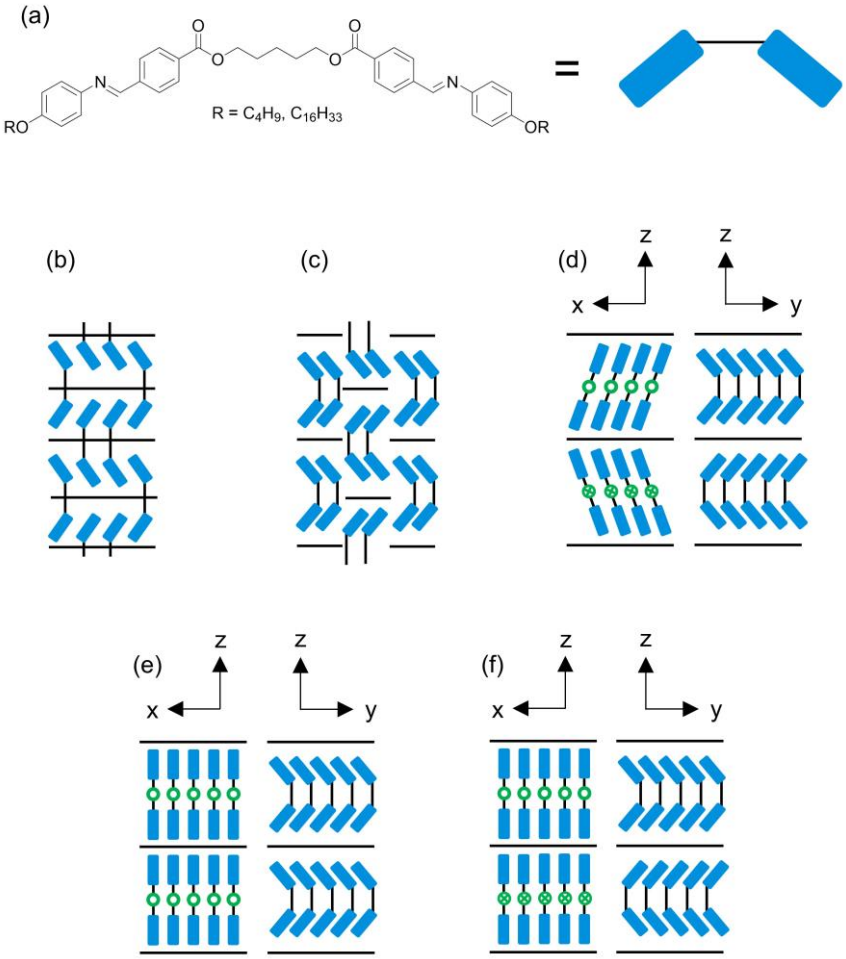

Figure 1-7. (a) Molecular structure of the bent-shaped dimeric molecule, mOAM5AMOm. Using this representation, the $SmCA^s$, $SmCA^f$, SmC_AP_A, $SmAP_F$ and $SmAP_A$ phases are schematically illustrated in (b), (c), (d), (e), and (f), respectively.

dimeric molecules are α,ω-bis(4-alkoxyanilinebenzylidene-4′-carbonyloxy)pentanes (mOAM5AMOm)[35] with the formula shown in Figure 1-7(a). The bent-shaped dimeric molecules form three types of the smectic LCs (refer to Figures 1-7(b)–(d)), depending on the alkoxy tail group. When the tail length was short (m = 4 and 6), the $SmCA^s$ phase was formed. Here each mesogen, but not a bent-shaped dimeric molecule, participated to form each smectic layer. When the tail length was medium (m = 8–12), the frustrated $SmCA^f$ phase was formed. When the tail length was long (m = 14–18), the smectic structure was identified as the SmC_AP_A phase, where each bent-shaped dimeric molecule participates in each layer comprising the bilayer of mesogenic groups. Within a layer, the bent-shaped dimeric molecules are packed with significant tilting of the molecular axis and in the same direction of the bent (polar) axis. The polar directions are opposite between the neighboring layers. Furthermore, the mixture of 4OAM5AMO4 forming the $SmCA^s$ phase and 16OAM5AMO16 forming the SmC_AP_A phase with the antiferroelectricity formed the $SmAP_F$ (see Figure 1-7(e)) and $SmAP_A$ phases (see Figure 1-7(f)) by a specific ratio, respectively.[37] The ferroelectricity of the $SmAP_F$ phase was identified by a single current peak under a triangular wave field and a clear second harmonic

generation.[37] The dimeric molecules have lower LC phase temperature than the banana molecules due to the introduction of an alkyl spacer. Considering the application, dimeric molecules are superior to banana molecules in terms of LC phase temperature.

1.3. Required Properties for Application of Ferroelectric LCs

Ferroelectric LCs are not only interesting from the viewpoint of fundamental science, but they are also promising for commercial uses, such as high-energy density capacitors, electrostatic actuator and novel information displays capable of microsecond electro-optic responses.[39-42] The use of soft LC materials might enable the realization of these flexible devices. As a result, it is expected that the applicability of the device will greatly increase. In terms of performance, especially in the capacitors and electrostatic actuators, increasing the values of the P_s and dielectric constant (ε) greatly contributes to their respective performances. As a basis for this, the relationship between the generated force, P_s, and ε in the electrostatic actuator is shown below.[40,41]

The source of the generated force (F) in an electrostatic actuator is the electric charge (Q) accumulated at the electrode / dielectric interface as shown in Figure 1-8(a). When an electric field (E) is applied to parallel-plate electrodes with a distance (d) between the electrodes, the F acting between the electrodes can be expressed by

$$F = \frac{1}{2}QE = \frac{1}{2d}QV \qquad (1-1)$$

Therefore, to increase the F without increasing the driving voltage (V), it is necessary to increase the Q. For this purpose, it is effective to use the polarization phenomenon. Ferroelectric LCs are known to generate huge P_s as described above. It is thus expected that a huge generated force can be obtained if the ferroelectric LCs is used as the electrostatic actuator medium.

In contrast, for a paraelectric material, the accumulated charge is proportional to the applied voltage,

$$Q = CV = \frac{\varepsilon_r \varepsilon_0 S}{2}\left(\frac{V}{d}\right)^2 \qquad (1-2)$$

where C is the capacitance, V is the applied voltage, d is the distance between electrodes, S is the electrode area, ε_0 is the dielectric constant of a vacuum, and ε_r is the relative dielectric constant. Substituting Equation (1-2) into Equation (1-1) gives

$$F = \frac{\varepsilon_r \varepsilon_0 S}{2}\left(\frac{V}{d}\right)^2 \qquad (1-3)$$

Equation (1-3) for the generated force is commonly used for electrostatic actuators with ordinary paraelectric media as shown in Figure 1-8(b). Therefore, in order to increase the F, it is necessary to increase the ε_r from the viewpoint of the material.

As described above, increasing the P_s and ε_r of the ferroelectric LCs has the advantage of greatly improving the performance of the device. In the next section, the general methods for evaluating the P_s and ε_r are described.

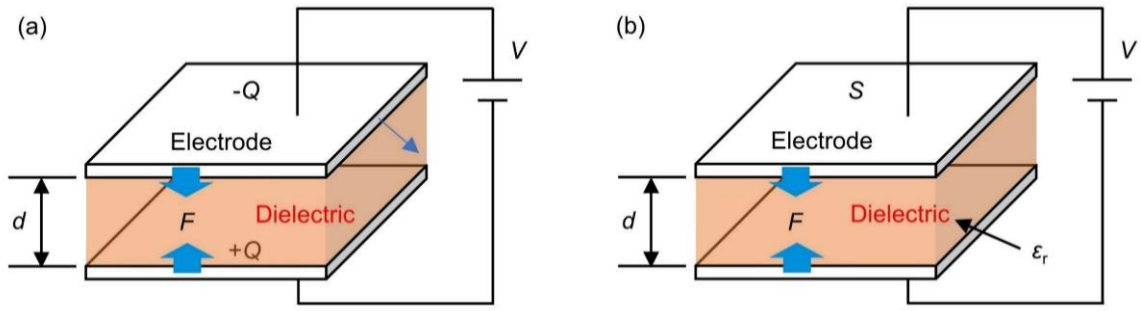

Figure 1-8. The actuation system using a typical sandwich-structure corresponding to (a) Equation 1-1 and (b) Equation 1-3.

1.3.1. Spontaneous Polarization (P_s)

The intensity of polarization is defined as the electric dipole moment per unit volume of the dielectric material. The P_s is a polarization that occurs under the influence of an internal process in a dielectric, without the effect of external factors. The P_s existing in the ferroelectric phase has the property of aligning in the direction of the electric field when a sufficiently large electric field is applied. By measuring this current, the P_s value and switching characteristics can be evaluated. In the antiferroelectric phase, although the P_s is canceled in the absence of an external electric field, the direction of polarization can be aligned by applying an electric field as in the ferroelectric phase.

In triangular wave application, the response current (I) by applying a field (V) can be written as a sum of the following three contributions; (i) charge accumulation in the capacitor (I_c) (ii) the ion flow (I_i) and (iii) the polarization realignment (I_p). Thus, one obtain[43]

$$I = I_c + I_p + I_i = C\frac{dV}{dt} + \frac{dP}{dt} + \frac{V}{R'} \quad (1-4)$$

Where P is the amount of charge induced by the polarization realignment. The three contributions of I_c, I_i and I_p are shown in Figure 1-9. The reversal P_s is obtained by integrating over half the period of the applied electric field based on the baseline drawn for the response current peak and dividing by the electrode area. The half-period of the applied electric field, P_s, is equal to half of the reversal P_s. In the ferroelectric phase, which exhibits two-state inversion, one current peak is observed per half period of the applied electric field, while in the antiferroelectric phase, which exhibits three-state inversion, two current peaks are observed. The switching response time of the device can be calculated directly from the current response of the square wave.[44]

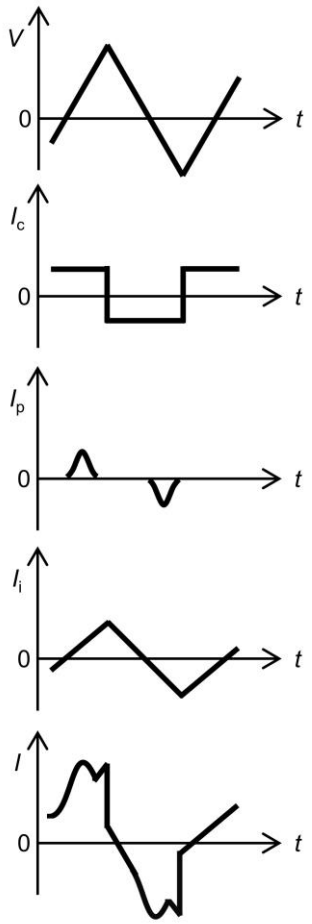

Figure 1-9. Schematic illustration of the current induced by applying a field with a triangular form. Three contributions, I_c, I_p and I_i, to the overall current I, are due to the charge accumulation, the polarization realignment, and the ion flow, respectively.

1.3.2. Relative Dielectric Constant (ε_r)

The polarization is induced by applying an external electric field to the dielectric. Among the induced polarizations, orientational polarization results from the rotation of molecules with permanent dipoles by an external electric field. The magnitude of the induced polarization varies when the LC phase is subjected to a time-dependent electric field. As long as the molecular reorientation follows the instantaneous field, the induced polarization (or the ε_r) is constant. It is within this frequency range the ε_r can be denoted the ε_s, and the mode is fully contributing to the ε_r. At higher frequencies where the dipolar reorientation is no longer in phase with the field, the contribution of the mode decreases more and more until it is completely absent. The corresponding value of the ε_r is denoted as the ε_∞. This region of the dielectric spectrum is called the relaxation region. At higher frequencies other modes may still be active and contribute to the ε_r. Let us denote the contribution of each mode to the ε_r as the dielectric strength ($\Delta\varepsilon$).[45]

$$\Delta\varepsilon = \varepsilon_s - \varepsilon_\infty \qquad (1-5)$$

Within the relaxation regime there is a phase difference between the field (stimulus) and the induced polarization (response). Due to this phase difference, a part of the electric energy is dissipated in the form of heat, Thus, there is an energy loss that is absorbed by the dielectric. Mathematically, this dielectric absorption is accounted for by introducing the complex dielectric constant ε^*, conveniently written as[45]

$$\varepsilon^* = \varepsilon' - \mathrm{i}\varepsilon'' \qquad (1-6)$$

The imaginary part due to each molecular process goes through a maximum when changing the frequency.

In the study of dielectric relaxation, the $\Delta\varepsilon$ is used instead of the ε_r. The $\Delta\varepsilon$ is the relative dielectric constant considering the effect of ion diffusion in the low frequency region (~10 Hz) and is calculated from ε' and ε'' using semi-empirical formulas. Here, semi-empirical formulas are introduced that are often used in dielectric analysis. Furthermore, the concept of Cole-Cole plots which are useful for visually understanding dielectric relaxation data are described. Although there are several ways to express the relaxation formula, here, the forms that are easy to compare, such as the Debye and the Cole-Cole formulas are described.

A simple model allowing to describe the relaxation of the dielectric permittivity in terms of a single time constant is due to Debye.[46] The real (ε') and the imaginary (ε'') parts of the complex dielectric constant ε^* are written as

$$\varepsilon^* = \varepsilon_\infty + \frac{\Delta\varepsilon}{1 + i\omega\tau} \qquad (1-7)$$

$$\varepsilon' = \varepsilon_\infty + \frac{\Delta\varepsilon}{1 + \omega^2\tau^2} \qquad (1-8)$$

$$\varepsilon'' = \frac{\Delta\varepsilon\omega\tau}{1 + \omega^2\tau^2} \qquad (1-9)$$

where $\Delta\varepsilon$ is the dielectric strength, ω is the angular frequency of the applied field, and τ is the relaxation time which is related to the relaxation frequency f_r as $\tau = 1/2\pi f_r$. In Figure 1-10(a), the real and imaginary parts of the dielectric constant are plotted against the frequency. Eliminating the frequency from equations (1-8) and (1-9), the equation of a circle is obtained with center on the ε' axis as shown in Figure 1-10(b). This graphical representation of the equation is called the Cole-Cole plot. The plot is very useful to check if the experimental values of ε' and ε'' can be described by a single relaxation time, which it often can't do. Many systems show a deviation in this sense from Debye dispersion. In order to describe systems which do not relax with a single relaxation time, Cole and Cole have extended the Debye equation by introducing the distribution parameter α.[47]

$$\varepsilon^* = \varepsilon_\infty + \frac{\Delta\varepsilon}{1 + (i\omega\tau)^{1-\alpha}} \quad 0 \le \alpha < 1 \qquad (1-10)$$

$$\varepsilon' = \varepsilon_\infty + \frac{(\varepsilon_s - \varepsilon_\infty)[1 + (\omega\tau)^{1-\alpha}\sin(\alpha\pi/2)]}{1 + 2(\omega\tau)^{1-\alpha}\sin(\alpha\pi/2) + (\omega\tau)^{2(1-\alpha)}} \qquad (1-11)$$

$$\varepsilon'' = \frac{(\varepsilon_s - \varepsilon_\infty)[(\omega\tau)^{1-\alpha}\cos(\alpha\pi/2)]}{1 + 2(\omega\tau)^{1-\alpha}\sin(\alpha\pi/2) + (\omega\tau)^{2(1-\alpha)}} \qquad (1-12)$$

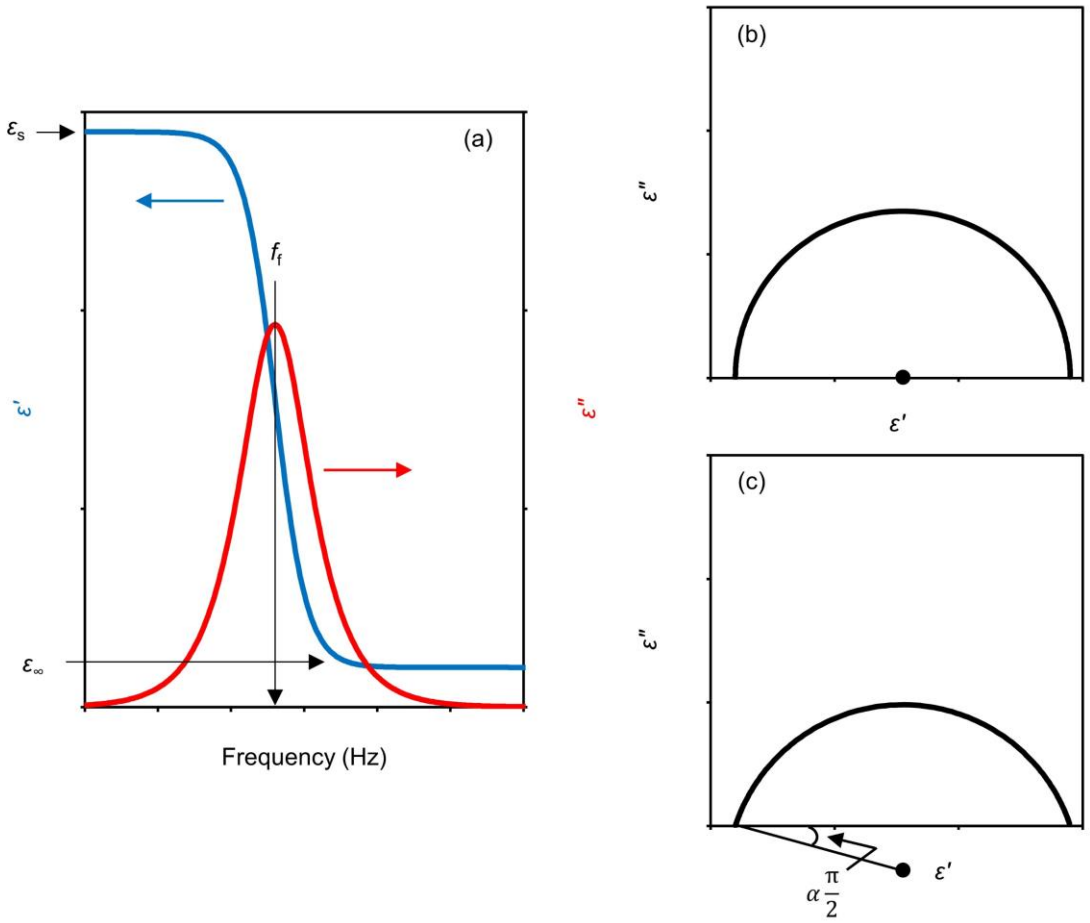

Figure 1-10. (a) Typical curve for the frequency dependence of the real (ε') and imaginary (ε'') parts of the complex dielectric constant. (b) Cole-Cole plot showing the relaxation between ε' and ε'' for a mechanism with a single relaxation time. (c) Cole-Cole plot showing the relaxation between ε' and ε'' for a mechanism characterized by a distribution of relaxation times; α is the distribution parameter.

The corresponding Cole-Cole plot with its center shifted is shown in Figure 1-10(c). Although the system has a single relaxation time because equation (1-10) is equivalent to Debye's relaxation equation (1-7) for $\alpha = 0$, the distribution of the relaxation time is widened as α increases.

1.4. Ferroelectric LCs with higher P_s and $\Delta\varepsilon$

Several ferroelectric LCs with high P_s and $\Delta\varepsilon$ have been reported so far. For example, Ozaki et al. synthesized some chiral SmC* materials with two chiral carbons or bulky molecular moieties and found them to have very high P_s (0.2 μCcm^{-2}) and $\Delta\varepsilon$ (> 7000) at 250 μm-thick cell.[48] Also, the previously mentioned DIO and RM734 materials reveal anomalously huge $\Delta\varepsilon$ around 10000 and a large P_s of about 4 μCcm^{-2}, which are an order of magnitude higher than

the previously reported values in other ferroelectric LC phases.[10-12] Several other molecules and their ferroelectric properties are intensively studied.[13-20] Furthermore, in the ferroelectric phase of banana molecules, W586 with carbosilane groups exhibit $\Delta\varepsilon$ of 300 and 2000 in 3 μm and 25 μm-thick cells, respectively, and the P_s reaches 0.4 μCcm^{-2}.[49] The azo-banana molecule, which is composed of asymmetric molecules with fluoro substitution, achieves the maximum value of $\Delta\varepsilon$ (~ 400) in a 9 μm-thick cell.[26]

1.5. Objective of Thesis

As mentioned above, ferroelectric LCs with enhanced the P_s and $\Delta\varepsilon$ have a great impact not only on basic science but also on industry. Hence, it is of great significance to obtain the molecular design for increasing the P_s and $\Delta\varepsilon$. The objective of this thesis is to obtain the molecular design for enhancing the P_s and $\Delta\varepsilon$ for the bent-shaped dimeric molecules with low LC phase temperature among bent LCs that can form a wide variety of LC phases.

1.6. Structure of Thesis

In Chapter 1 "General Introduction", the expression mechanism of ferroelectric LCs and the need for high P_s and $\Delta\varepsilon$ required for various applications are outlined. In addition, by reviewing conventional LCs research on the P_s and $\Delta\varepsilon$, the significance of the molecular design for enhancing the P_s and $\Delta\varepsilon$ in bent-shaped dimeric molecules is indicated. Furthermore, the objective and structure of this thesis are presented.

In Chapter 2 "Huge Dielectric Constants of the Ferroelectric Smectic-A Phase in Bent-Shaped Dimeric Molecules", in order to grasp the $\Delta\varepsilon$ of the ferroelectric phase in the bent-shaped dimeric molecules and obtain the molecular design for the $\Delta\varepsilon$ enhancement, the dielectric relaxation properties of the $SmAP_F$ phase formed by mixtures of bent-shaped dimeric molecules with different alkyl chain lengths are analyzed.

In Chapter 3 “Electric Switching Behaviors and Dielectric Relaxation Properties in Ferroelectric, Antiferroelectric and Paraelectric Smectic Phases of Bent-Shaped Dimeric Molecules”, in order to obtain the molecular design for the $\Delta\varepsilon$ enhancement, the relationship between the dielectric relaxation properties and electrical switching behaviors in the $SmAP_F$, $SmAP_A$ and SmC_AP_A phases is analyzed.

In Chapter 4 “Spontaneous Polarization Characteristics in Polar Smectic Phases of Fluoro-Substituted Bent-Shaped Dimeric Molecules”, in order to obtain the molecular design for the P_s enhancement, three types of the bent-shaped dimeric molecules are synthesized by fluorine substitution on the mesogenic unit and, the effect of fluorine substitution on the polar smectic phase is analyzed.

In Chapter 5 “Three Distinct Polar Phases, Isotropic, Nematic and Smectic-A Phases Formed from Fluoro-Substituted Dimeric Molecule with Large Dipole Moment”, a novel dimeric molecule with large dipole moment is developed to enhance the P_s and $\Delta\varepsilon$. A dimeric molecule, di-5(3FM-C4T), with fluorine-substituted mesogenic cores as side wings connected by a

pentamethylene spacer is synthesized and demonstrated for the P_s and $\Delta\varepsilon$.

In Chapter 6, "General Conclusion", the results obtained in each chapter are summarized and the molecular design for enhancement of the P_s and $\Delta\varepsilon$ in the bent-shaped dimeric molecules are presented.

References

(1) Goodbye, J. W. Smectic Polymorphism and Molecular Shape-the Orthogonal Phases. *Mol. Cryst. Liq. Cryst.* **1981**, *75*, 179-199.

(2) Percec, V.; Sahoo, D. Discotic liquid crystals 45 years later. Dendronized discs and crowns increase liquid crystal complexity to columnar from spheres, cubic Frank-Kasper, liquid quasicrystals and memory-effect induced columnar-bundles. *Giant* **2022**, *12*, 100127.

(3) Meyer, R. B. Ferroelectric Liquid Crystals; A Review. *Mol. Cryst. Liq. Cryst.* **1977**, *40*, 33-48.

(4) M. Born. Über anisotrope Flüssigkeiten. Versuch einer Theorie der flüssigen Kristalle und des elektrischen Kerr-Effekts in Flüssigkeiten. Sitzungsber. *Preuss. Akad Wiss.* **1916**, *30*, 614–650.

(5) Yu, C. J.; Yu, M.; Lee, S. D. Phase Diagram for Ferroelectric Nematic Ordering of Hard Spherocylinders with Longitudinal Dipoles. *Jpn. J. Appl. Phys.* **2002**, *41*, L102–L104.

(6) Watanabe, T.; Miyata, S.; Furukawa, T.; Takezoe, H.; Nishi, T.; Sone, M.; Migita, A.; Watanabe, J. Nematic Liquid Crystals with Polar Ordering Formed from Simple Aromatic Polyester. *Jpn. J. Appl. Phys.* **1996**, *35*, L505–L507.

(7) Koike, M.; Yen, C. C.; Yuqing, L.; Tsuchiya, H.; Tokita, M.; Kawauchi, S.; Takezoe, H.; Watanabe, J. Unusual Nematic Liquid Crystal with Polar C_s Symmetry Formed from Aromatic Polyesters with Head−Tail Character. *Macromolecules* **2007**, *40*, 2524–2531.

(8) Yen, C. C.; Taguchi, Y.; Tokita, M.; Watanabe, J. Polar Nematic Phase in Lyotropic Solutions of Poly(γ-benzyl glutamate) and Its Temperature Instability As Detected by SHG Measurement. *Macromolecules* **2008**, *41*, 2755–2758.

(9) Park, B.; Kinoshita, Y.; Kinoshita, Y.; Takezoe, H.; Watanabe, J. Ferroelectricity in the Lyotropic Cholesteric Phase of Poly L-Glutamate. *Jpn. J. Appl. Phys.* **1998**, 37 L136–L138.

(10) Nishikawa, H.; Shiroshita, K.; Higuchi, H.; Okumura, Y.; Haseba, Y.; Yamamoto, S.; Sago, K.; Kikuchi, H. A fluid liquid-crystal material with highly polar order. *Adv. Mater.* **2017**, *29*, 1702354.

(11) Mandle, R. J.; Cowling, S. J.; Goodby, J. W. A nematic to nematic transformation exhibited by a rod-like liquid crystal. *Phys. Chem. Chem. Phys.*, **2017**, *19*, 11429–11435.

(12) Mandle, R. J.; Cowling, S. J.; Goodby, J. W. Rational Design of Rod-Like Liquid Crystals Exhibiting Two Nematic Phases. *Chem. Eur. J.* **2017**, *23*, 14554–14562.

(13) Mertelj, A.; Cmok, L.; Sebastián, N.; Mandle, R. J.; Parker, R. R., Whitwood, A. C.; Goodby, J. W.; Čopič, M. Splay Nematic Phase. *Phys. Rev. X* **2018**, *8*, 041025.

(14) Chen, X.; Korblova, E.; Dong, D.; Wei, X.; Shao, R.; Radzihovsky, L.; Glaser, M. A.;

Maclennan, J. E.; Bedrov, D., et al. First-principles experimental demonstration of ferroelectricity in a thermotropic nematic liquid crystal: Polar domains and striking electro-optics. *Proc. Natl. Acad. Sci. U.S.A.* **2020**, *117*, 14021–14031.

(15) Sebastián, N.; Cmok, L.; Mandle, R. J.; Fuente, M.; Olenik, I. D.; Čopič, M.; Mertelj, A. Ferroelectric-Ferroelastic Phase Transition in a Nematic Liquid Crystal. *Phys. Rev. Lett.* **2020**, *124*, 037801.

(16) Manabe, A.; Bremer, M.; Kraska, M. Ferroelectric nematic phase at and below room temperature. *Liq. Cryst.* **2021**, *48*, 1079–1086.

(17) Li, J.; Nishikawa, H.; Kougo, J.; Zhou, J.; Dai, S.; Tang, W.; Zhao, X.; Hisai, Y.; Huang, M.; Aya, S. Development of ferroelectric nematic fluids with giant-ε dielectricity and nonlinear optical properties, *Sci. Adv.* **2021**, *7*, eabf5047.

(18) Mandle, R. J.; Cowling, S. J., Goodby, J. W. Structural variants of RM734 in the design of splay nematic materials. *Liq. Cryst.* **2021**, *48*, 1780–1790.

(19) Saha, R.; Nepal, P.; Feng, C.; Hossain, M. S.; Fukuto, M.; Li, R.; Gleeson, J. T.; Sprunt, S.; Twieg, R. J.; Jákli, A. Multiple ferroelectric nematic phases of a highly polar liquid crystal compound. *Liq. Cryst.* **2022**, *49*, 1784–1796.

(20) Yadav, N.; Panarin, Y. P.; Vij, J. K.; Jiang, W.; Mehl, G. H. Polar nature of the ferro-electric nematic studied by dielectric spectroscopy. ArXiv 2203.04944 (2022).

(21) Sekine, T.; Watanabe, J.; Furukawa, T.; Takezoe, H. Distinct ferroelectric smectic liquid crystals consisting of banana shaped achiral molecules. *J. Mater. Chem.* **1996**, *6*, 1231–1233.

(22) Sekine, T.; Niori T.; Watanabe, J.; Furukawa, T.; Choi, S. W.; Takezoe, H. Spontaneous helix formation in smectic liquid crystals comprising achiral molecules. *J. Mater. Chem.* **1997**, *7*, 1307–1309.

(23) Pelzl, G.; Diele, S.; Weissflog, W. Banana-Shaped Compounds- A New Field of Liquid Crystals. *Adv. Mater.* **1999**, *11*, 707–724.

(24) Takezoe, H.; Takanishi, Y. Bent-core liquid crystals: their mysterious and attractive world. *Jpn. J. Appl. Phys.* **2006**, *45*, 597–625.

(25) Jákli, A.; Lavrentovich, O. D.; Selinger, J. V. Physics of liquid crystals of bent-shaped molecules. *Rev. Mod. Phys.* **2018**, *90*, 045004.

(26) Link, D. R.; Natale, G.; Shao, R.; Maclennan, J. E.; Clark, N. A.; Körblova, E.; Walba, D. M. Spontaneous Formation of Macroscopic Chiral Domains in a Fluid Smectic Phase of Achiral Molecules. *Science* **1997**, *278*, 1924–1927.

(27) Heppke, G.; Jákli, A.; Rauch, S.; Sawade, H. Electric-field-induced chiral separation in liquid crystals. *Physical Review E* **1999**, *60*, 5575–5579.

(28) Walba, D. M.; Körblova, E.; Shao, R.; Maclennan, J. E.; Link, D. R.; Glaser, M. A.; Clark, N. A. A ferroelectric liquid crystal conglomerate composed of racemic molecules. Science **2000**, *288*, 2181–2184.

(29) Eremin, A.; Diele, S.; Pelzl, G.; Nádasi, H.; Weissflog, W.; Salfetnikova, J.; Kresse, H.

Experimental evidence for an achiral orthogonal biaxial smectic phase without in-plane order exhibiting antiferroelectric switching behavior. *Physical Review E* **2001**, *64*, 051707.

(30) Rauch, S.; Bault, P.; Sawade, H.; Heppke, G.; Nair, G. G.; Jákli, A. Ferroelectric-chiral–antiferroelectric-racemic liquid crystal phase transition of bent-shape molecules. *Physical Review E* **2002**, *66*, 021706.

(31) Kumar, J.; Prasad, C. Ferroelectric nematic and ferrielectric smectic mesophases in an achiral bent-core azo compound. *J. Phys. Chem. B* **2018**, *122*, 2998–3007.

(32) Watanabe, J.; Nakata, Y.; Shimizu, K. Frustrated bilayer smectic phase in main-chain polymers with two different spacers. *J. Phys. II France* **1994**, *4*, 581–588.

(33) Watanabe, J.; Hayashi, M.; Nakata, Y.; Niori, T.; Tokita, M. Smectic liquid crystals in main-chain polymers. *Prog. Polym. Sci.* **1997**, *22*, 1053–1087.

(34) Watanabe, J.; Izumi T.; Niori, T.; Zennyoji, M.; Takanishi, Y.; Takezoe, H. Smectic mesophase properties of dimeric compounds 2 distinct formation of smectic structures with antiferroelectric ordering and frustration. *Mol. Cryst. Liq. Cryst.* **2000**, *346*, 77–86.

(35) Izumi, T.; Kang, S.; Niori, T.; Takanishi, Y.; Takezoe, H.; Watanabe, J. Smectic mesophase behavior of dimeric compounds showing antiferroelectricity, frustration and chirality. *Jpn. J. Appl. Phys.* **2006**, *45*, 1506–1514.

(36) Izumi, T.; Naitou, Y.; Tokita, M.; Watanabe, J. Frustrated smectic phase appearing as transitional state between single-layer and antiferroelectric bilayer smectic phases in binary mixtures of dimeric compounds. *Jpn. J. Appl. Phys.* **2006**, *45*, 4991–4993.

(37) Izumi T.; Naitou, Y.; Shimbo, Y.; Takanishi, Y.; Takezoe, H.; Watanabe, J. Several types of bilayer smectic liquid crystals with ferroelectric and antiferroelectric properties in binary mixture of dimeric compounds. *J. Phys. Chem. B* **2006**, *110*, 23911–23919.

(38) Watanabe, J.; Hayashi, M. Thermotropic liquid crystals of polyesters having a mesogenic p,p'-bibenzoate unit. 2. X-ray study on smectic mesophase structures of BB-5 and BB-6. *Macromolecules* **1989**, *22*, 4083–4088.

(39) Strivastava, A.K.; Voshchenko, V.V. Ferroelectric liquid crystals and their application in modern display and photonic devices. In *Unconventional Liquid Crystals and Their Applications*; Lee, W.; Kumer, S.; De Gruyter, 2021; pp 153−210.

(40) Nishimura, S.; Masuyama, S.; Shimizu, G.; Chen, C. Y.; Ichibayashi, T.: Watanabe, J. Lowering of electrostatic actuator driving voltage and increasing generated force using spontaneous polarization of ferroelectric nematic liquid crystals. *Adv. Phys. Res.*, **2022**, *1*, 2200017.

(41) Carpi, F.; Rossi, D. D.; Kornbluh, R.; Pelrine, R.; Sommer-Larsen, P. Dielectric Elastomers as Electromechanical Transducers. **2008**.

(42) Guo, Q.; Yan, K.; Chigrinov, V.; Zhao, H.; Tribelsky, M.; Ferroelectric Liquid Crystals: Physics and Applications. *Crystals* **2019**, *9*, 470.

(43) Miyasato, K.; Abe, S.; Takezoe, H.; Fukuda, A.; Kuze, E. Direct Method with Triangular Waves for Measuring Spontaneous Polarization in Ferroelectric Liquid Crystals. *Jpn. J.*

Appl. Phys. **1983**, *22*, L661-L663.

(44) Skarp, K.; Dahl, I.; Lagerwall, S. T.; Stebler, B. Polarization and Viscosity Measurements in a Ferroelectric Liquid Crystal by the Field Reversal Method. *Mol. Cryst. Liq. Cryst.* **1984**, *114*, 283-297.

(45) Gouda, F.; Skarp, K.; Lagerwall, S. T. Dielectric studies of the soft mode and Goldstone mode in ferroelectric liquid crystals. *Ferroelectrics* **1991**, *113*, 165-206.

(46) Debye, P. J. W. Polar molecules. Dover publications, **1929**, New York.

(47) Cole, K.; Cole, R. Dispersion and absorption in dielectrics I, alternating current characteristics, *J. Chem. Phys.* **1941**, *9*, 341–351.

(48) Ozaki, M.; Yoshino, K.; Sakurai, T.; Mikami, N.; Higuchi, R. Dielectric properties of new stable ferroelectric liquid crystals with large spontaneous polarization, *J. Chem. Phys.* **1987**, *86*, 3648-3654.

(49) Guo, L.; Gorecka, E.; Pociecha, D.; Vaupotič, N.; Čepič, M.; Reddy, R. A.; Gornik, K.; Araoka, F.; Clark, N. A.; Walba, D. M. et al. Ferroelectric behavior of orthogonal smectic phase made of bent-core molecules. *Physical Review E* **2011**, *84*, 031706.

CHAPTER 2

Huge Dielectric Constants of the Ferroelectric Smectic-A Phase in Bent-Shaped Dimeric Molecules

2.1. Introduction

The typical bent-shaped dimeric molecules with two aromatic mesogens linked by an odd-carbon numbered alkyl spacer are α,ω-bis(4-alkoxyanilinebenzylidene-4′-carbonyloxy)pentanes (mOAM5AMOm)[1-3] with the formula shown in Figure 2-1. These bent-shaped dimeric molecules form three types of the smectic liquid crystals (LCs), $SmCA^s$, $SmCA^f$ and SmC_AP_A phases depending on the alkoxy tail group.[1] Furthermore, the mixture of 4OAM5AMO4 forming the $SmCA^s$ phase and 16OAM5AMO16 forming the SmC_AP_A phase with the antiferroelectricity forms the ferroelectric smectic-A ($SmAP_F$) phase by a specific ratio.

The $SmAP_F$ phase generally shows that the molecules lie perpendicular to the layer, with ferroelectric alignment of the polar directions. The bent-shaped dimeric molecules and general bent-shaped molecules form the $SmCP_F$ and the $SmCP_A$, but the $SmAP_F$ phase is not commonly observed in these systems.[1,2,4,5,6] For example, W586 consisting of the bent-shaped molecule with a carbosilane group at a terminal chain suppresses out-of-layer fluctuations, favoring anticlinic tail orientation and thus the $SmAP_F$ phase due to the influence of carbosilane.[7-9] In the bent-shaped dimeric molecules, mixing of 4OAM5AMO4 and 16OAM5AMO16 with different alkyl chain lengths obviously prevents the tilted association of molecules, although

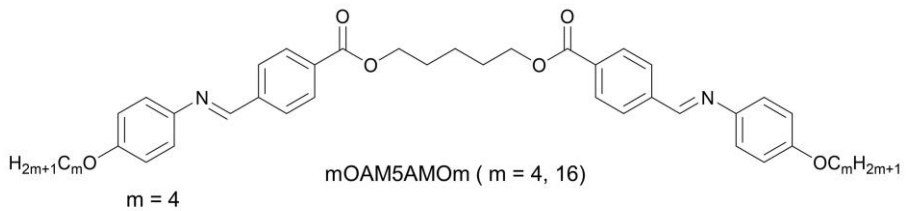

m = 4
Crystal – 89.7 °C – $SmCA^s$ – 142.5 °C – Isotropic
m = 16
Crystal – 109.2 °C – SmC_AP_A – 120.0 °C – Isotropic
m = 4 (65 mol%) + 16 (35 mol%)
Crystal – 89.0 °C – $SmAP_A$ – 94.0 °C – $SmAP_F$ - 115.0 °C - Isotropic

Figure 2-1. Molecular structures and phases sequence for mOAM5AMOm (m = 4, 16, and 4 + 16). The transition temperatures are taken from DSC cooling run and the switching current curve.[3]

the reason is not clear.[3] As one of the properties of the $SmAP_F$ phase by the bent-shaped molecule, Guo et al. reported that W586 has high dielectric constants.[10]

In this chapter, the dielectric relaxation properties of the $SmAP_F$ phase in the bent-shaped dimeric molecules is examined.

2.2. Experimental Section

The mOAM5AMOm dimers with m values of 4 and 16 were synthesized following the methods reported in a previous report.[1] The bent-shaped dimeric molecules mixture of 4OAM5AMO4 (65 mol%) + 16OAM5AMO16 (35 mol%) was prepared by evaporating a chloroform solution of the two molecules at a predetermined molar ratio.[3] The phase transition temperatures were determined by DSC (SHIMADZU DSC-60 Plus) at a rate of 5 °Cmin^{-1} under cooling and heating runs. Texture observation and the identification of the mesophases were carried out using a polarizing optical microscope (OLYMPUS BX53) equipped with a hot stage and a temperature controller (Mettler Toledo FP 82HT). Electrooptical and dielectric investigations were performed using glass cells, having indium tin oxide (ITO) electrodes commercially available from EHC Co., Ltd. The area of the ITO electrodes was 100 mm^2, and the cell thicknesses of the ITO electrodes were 3, 10, 25, and 50 μm. In these cells, the bent-shaped dimeric molecules were homogeneously aligned with the bent plane parallel to the cell plane. Before the measurements, an AC applied fields of the 16OAM5AMO16 and the 4OAM5AMO4 (65 mol%) + the 16OAM5AMO16 (35 mol%) was applied at 33 and 5 $V_{pp}\mu m^{-1}$ for the growth of the LCs, respectively. The complex dielectric constants were measured in the frequency range between 10^1 and 10^7 Hz with the impedance analyzer (NF Electronic Instruments, FRA51615). The electric field was 1 V_{pp}.

2.3. Results and Discussion

The molecular structures and the phases sequence (from 1st cooling run of DSC) of the bent-shaped dimeric molecules 4OAM5AMO4, 16OAM5AMO16, and the mixture (4OAM5AMO4 (65 mol%) + 16OAM5AMO16 (35 mol%)) are given in Figure 2-1.

To clarify both the non-collective and collective motions of the molecules, the dielectric dispersion measurements were performed in the $SmCA^s$ (m = 4), SmC_AP_A (m = 16), and $SmAP_F$ (mixture of m = 4 and 16) phases. Here, it should be noted that the domain size is small especially in the $SmAP_F$ and SmC_AP_A phases just as cooled from isotropic phase. Hence, the domains of the $SmAP_F$ and SmC_AP_A were enlarged by applying the AC field of 5 $V_{pp}\mu m^{-1}$ and 33 $V_{pp}\mu m^{-1}$, respectively; they were grown up by agitation of molecular motion due to the ferroelectric switching. In Figures 2-2(a) and (b), the real (ε') and imaginary (ε'') parts of the dielectric constants are plotted against the frequency from 10^1 to 10^7 Hz, respectively. The two relaxation modes are observed in this frequency range. One is the low frequency (LF) mode which is observed at approximately 500 Hz in the $SmAP_F$ phase and possesses huge dielectric constants. The low relaxation frequency (f_r) of the order of 1 kHz or less,[10-12] as well as the

suppression under the DC bias fields (mentioned later), shows that this mode is the LF mode, the collective fluctuation of polarization that is attributable to the ferroelectric phase. Another is the high frequency (HF) mode observed at approximately 100 kHz in the $SmCA^s$ and the SmC_AP_A phases. The isotropic phase also exhibits this mode. It is attributable to the non-collective molecular rotation around the short axis of the mesogens as observed in the conventional LC phases.[13,14]

Figures 2-2(c) and (d) show the Cole-Cole plots for these two modes. The experimental dielectric spectra were further analyzed by fitting the following Cole-Cole model[15]:

$$\varepsilon^* = \varepsilon' - i\varepsilon'' = \varepsilon_\infty + \frac{\Delta\varepsilon}{1 + (\omega\tau)^{1-\alpha}} \quad 0 < \alpha < 1, \qquad (2-1)$$

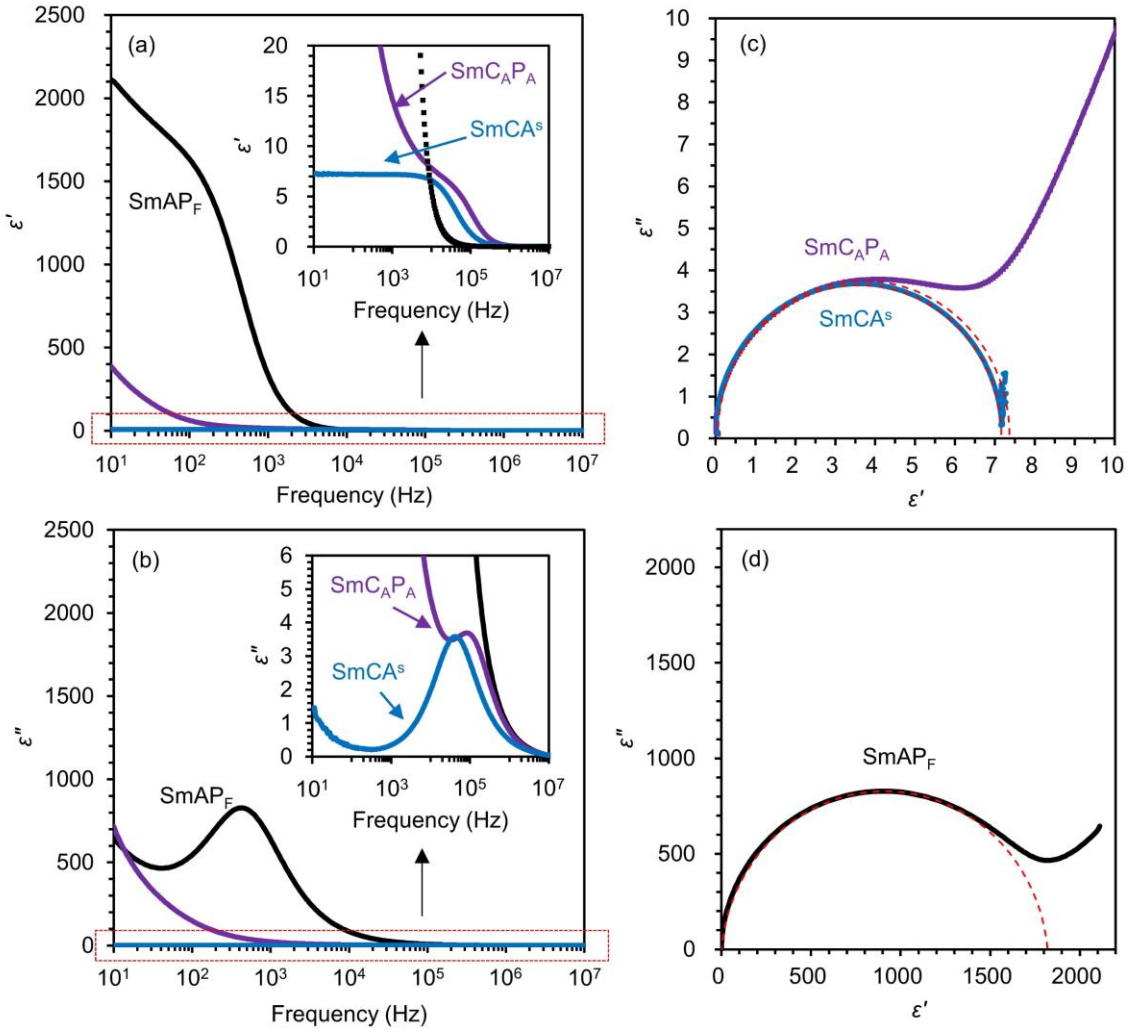

Figure 2-2. (a) and (b) Frequency dependence of the real (ε') and imaginary (ε'') parts of the complex dielectric constants of the SmC_AP_A (at 114°C), the $SmCA^s$ (at 90°C) and the $SmAP_F$ (at 98°C) phases, measured in a 3 μm-thick cell. In the insets, the vertical axis is expanded to clarify the HF mode. (c) Cole-Cole plot for the HF mode of the SmC_AP_A and the $SmCA^s$ phases, and (d) Cole-Cole plot for the LF mode of the $SmAP_F$ phase, based on the data of Figures 2-2 (a) and (b). The dashed curves are obtained by fitting Equation (2-1).

where ω is the angular frequency, $\Delta\varepsilon$ (= ε_s - ε_∞) is the dielectric strength, and ε_s and ε_∞ are the "static-frequency" and "infinite-frequency" dielectric constants, respectively. $\tau = 1/(2\pi f_r)$ is the relaxation time (where f_r is the relaxation frequency), and α is the distribution parameter of relaxation time. For $\alpha = 0$ Cole-Cole model reduces to Debye model. The fitting according to Cole-Cole equation is shown in Figures 2-2(c), (d) and 2-4(c), and the determined parameters are listed in Table 2-1. For the HF relaxation of the $SmCA^s$ and SmC_AP_A phases, the α is around 0. For the LF mode of the $SmAP_F$ phase, on the other hand, α is between 0.05 and 0.12.

Table 2-1. List of Cole-Cole parameters, $\Delta\varepsilon$, α and f_r determined from the data of Figure 2-2 and Figure 2-4.

	$SmAP_F$ (3 μm cell)	**$SmCA^s$ (3 μm cell)**	**SmC_AP_A (3 μm cell)**	**$SmAP_F$ (10 μm cell)**	**$SmAP_F$ (25 μm cell)**	**$SmAP_F$ (50 μm cell)**
$\Delta\varepsilon$	1.8×10^3	6.8	7.2	3.2×10^3	4.5×10^3	7.4×10^3
f_r (Hz)	4.9×10^2	1.3×10^5	8.2×10^4	5.4×10^2	3.5×10^2	3.3×10^2
α	6.0×10^{-2}	0	0	5.0×10^{-2}	7.0×10^{-2}	0.12

Most significant is that the $\Delta\varepsilon$ is very large (approximately 1800) for the LF mode of the $SmAP_F$ phase whereas much smaller, but usual values (< 10), are observed in the HF mode of the $SmCA^s$ and SmC_AP_A phases. The high $\Delta\varepsilon$ has been reported in the ferroelectric phases of the bent-shaped molecules.[10,16-18] W586 showed the maximum value of the $\Delta\varepsilon$ (~300) as observed in a 3 μm-thick cell.[10] Furthermore, the bent-shaped azo molecule consisting of nonsymmetrical molecules with a lateral fluoro substitution on one of the wings achieved the maximum value of the $\Delta\varepsilon$ (~400) in a 9 μm-thick cell.[18] The present $\Delta\varepsilon$ of 1800 exceeds these values substantially.

Figure 2-3 shows the temperature dependence of the characteristic f_r of the relaxation processes observed in the $SmCA^s$, SmC_AP_A, and $SmAP_F$ phases at 3 μm-thick cell. The HF mode observed in the $SmCA^s$ and SmC_AP_A phases follows the standard Arrhenius equation[16,18]

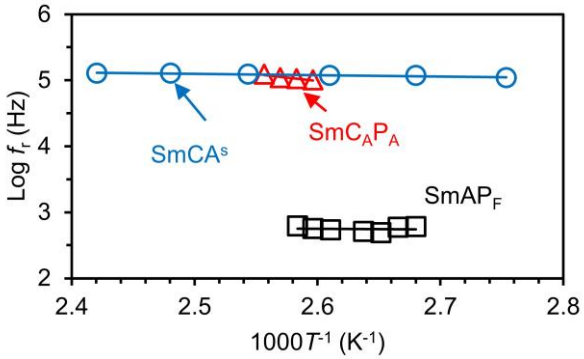

Figure 2-3. Logarithm of the dielectric relaxation frequencies as a function of inverse absolute temperature for the $SmCA^s$, the SmC_AP_A and the $SmAP_F$ phases at 3 μm-thick cell.

$$f_r = A\exp(-\frac{E_{act}}{k_B T}) \qquad (2-2)$$

where f_r is relaxation frequency, A is pre-exponential factor, E_{act} is the activation energy, k_B is the Boltzmann constant and T is the absolute temperature. Equation (2-2) is fitted to the experimental data points in order to obtain the E_{act}. Estimated E_{act} of the $SmCA^s$ and SmC_AP_A phases are 4 and 40 $kJmol^{-1}$, respectively. In the higher temperature region, the f_r of the $SmAP_F$ phase is somewhat temperature dependent, but seems to be independent in the lower temperature region as expected for the LF mode.[19]

As another feature of the LF mode in the $SmAP_F$ phase, the f_r and $\Delta\varepsilon$ strongly depend on the cell thickness (refer to Figure 2-4). As thickness increases from 3 to 50 μm, the f_r decreases from 500 to 300 Hz. On the other hand, the $\Delta\varepsilon$ almost linearly grows; although the $\Delta\varepsilon$ is approximately 1800 in a 3 μm-thick cell, it is 3200, 4500, and 7400 in the 10, 25, and 50 μm-thick cells, respectively.

A similar thickness dependence of the $\Delta\varepsilon$ for LF mode has been observed in the ferroelectric chiral Sm-C*[20] and $SmAP_F$ phases.[10] Ozaki et al. found that some chiral Sm-C*materials possess the dielectric constants larger than 7500 in a 250 μm-thick cell.[20] Guo et al. mentioned

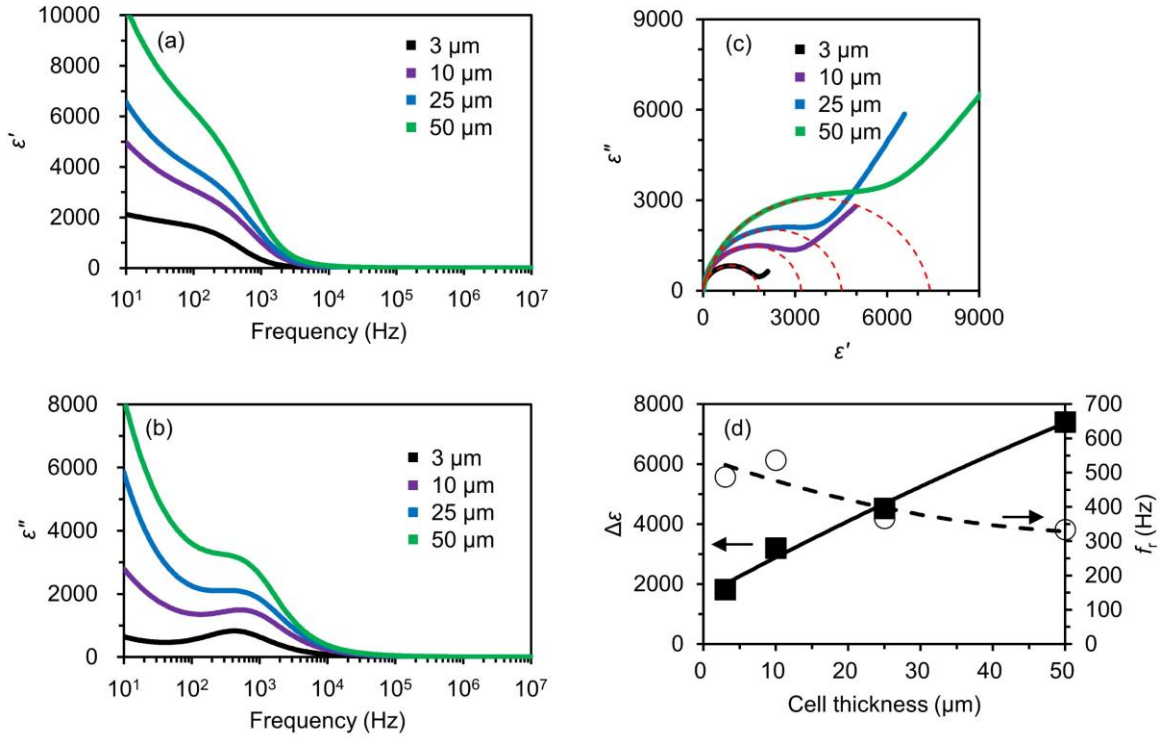

Figure 2-4. (a) and (b) Frequency dependence of the real (ε') and imaginary (ε'') parts of the complex dielectric constants of the 3, 10, 25, and 50 μm-thick cells in the $SmAP_F$ phase. (c) Cole-Cole plot of the 3, 10, 25, and 50 μm-thick cells in the $SmAP_F$ phase. The dashed curves are obtained by fitting Equation (2-1). (d) Cell thickness dependence of the $\Delta\varepsilon$ and the f_r in the $SmAP_F$ phase. The solid and dashed curves are guides for the eyes.

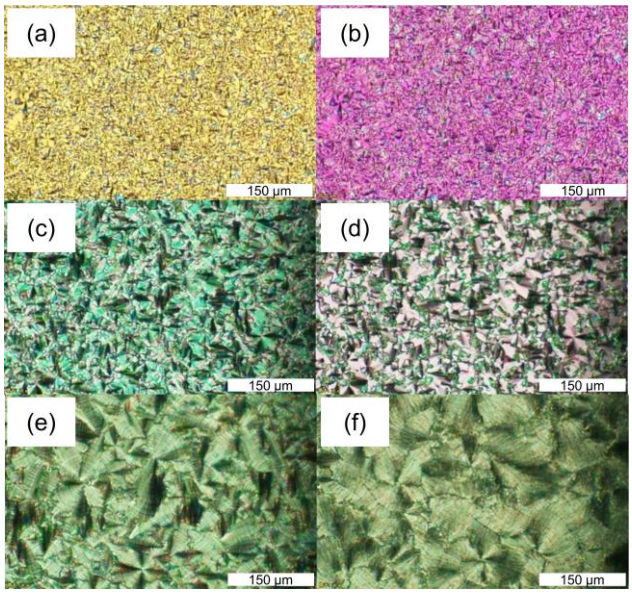

Figure 2-5. Optical textures in the $SmAP_F$ phase (a) in a 3 µm-thick cell at 0 $V\mu m^{-1}$ and (b) in a 3 µm-thick cell at 1 Vum^{-1} (c) in a 10 µm-thick cell at 0 $V\mu m^{-1}$ and (d) in a 10 µm-thick cell at 1 $V\mu m^{-1}$ (e) in a 25 µm-thick cell at 0 $V\mu m^{-1}$ and (f) in a 25 µm-thick cell at 1 $V\mu m^{-1}$.

that by linear extrapolating of $\Delta\varepsilon$ for W586 an even larger value (~20000) is expected for this cell thickness.[10] The $\Delta\varepsilon$ is estimated by linear extrapolation similar to Guo et al. The expected $\Delta\varepsilon$ of 30000 exceeds these values. One may speculate that such a cell thickness dependence is caused by a strong anchoring of the molecules to the cell surfaces, which can prevent the collective fluctuations to the spontaneous polarization (P_s) through the cell thickness, especially close to the surface. However, the anchoring can cause significant suppression only in a thin cell, but not lead to the linear increase with the cell's thickness. Only a theoretical approach to explain this trend has been carried out by Guo et al.[10] They collected the $\Delta\varepsilon$ with the cell where the bent direction of the bent-shaped molecules lay perpendicular to the cell's surface by the strong surface anchoring. In such a cell, it is speculated that a splay of polarization arises across its thickness that can induce the cell thickness dependence in the $\Delta\varepsilon$ and f_r in a relation with the anchoring strength. Comparing the model and the experimental results, they have estimated the correlation length in the bulk and the surface to be approximately 10 and 1 µm, respectively.

In our case, however, the molecular orientation reported by Guo et al.[10] is unlikely. Figures 2-5(a), (c), and (e) show the optical microscopic textures of the $SmAP_F$ phase in 3, 10, and 25 µm-thick cells, respectively. In all these cells, well-developed fan-shaped textures are observed, indicating the homogeneous alignment of the molecules, in other words, the alignment of the smectic layers perpendicular to the cell's surface. Figures 2-5(b), (d), and (f) indicate the textures under the DC bias fields. The textures do not change at all, but the birefringence colors change. This indicates that the bent (polar) direction of the molecules that are initially parallel to the cell's surface become perpendicular to it because of the ferroelectric response. Based on the retardation obtained from the general polarization color chart, the birefringence (Δn) is estimated to be 0.07 at 0 $V\mu m^{-1}$ and 0.18 at 1 $V\mu m^{-1}$, which are well expected from the parallely

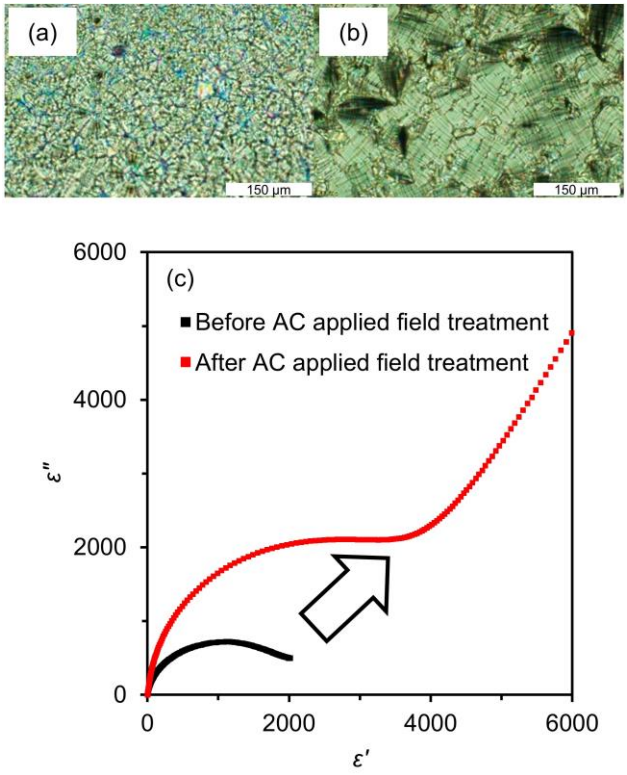

Figure 2-6. Optical textures in the $SmAP_F$ phase at a 25 μm-thick cell (a) before application of AC field and (b) after application of AC field of 5 $V_{pp}\mu m^{-1}$. (c) Cole-Cole plot for the dielectric data of their $SmAP_F$ phases; $\Delta\varepsilon$ are 1900 and 4500 before and after AC application, respectively.

and perpendicularly aligned models, respectively. In such a molecular alignment, the splay of polarization does not arise across the cell's thickness as reported by Guo et al.[10]

Figure 2-5 shows the clear trend of the fan-shaped domain size increasing with the cell's thickness. Further, its average size roughly corresponds to the cell's thickness, meaning that the domain is uniform across the cell thickness. Thus, the coherent length of the molecular dipoles that cooperatively orient in the AC applied field increases with the increase of the cell's thickness. This increment, that is the increase of the number of molecules participating in the collective motion, may be responsible for the increase of the $\Delta\varepsilon$ and the decrease of the f_r.

The close relationship between the domain size and the $\Delta\varepsilon$ can be seen even in the same cell. The domain size of the $SmAP_F$ phase as-cooled from isotropic melt is fairly small and, as mentioned above, grows under AC applied fields. The estimated $\Delta\varepsilon$ in the former cell is very small. Examples, as observed in a 25 μm-thick cell, are shown in Figure 2-6. The $\Delta\varepsilon$ is 1900 while it becomes 4500 after the AC field treatment.

The relationship between the cooperative motion of dipoles and the $\Delta\varepsilon$ has been treated theoretically[21] and experimentally.[22,23] Kirkwood[21] has extended the Onsager theory by treating the interacting dipoles, and shown that the $\Delta\varepsilon$ is proportional to

$$\frac{N\mu^2}{3kT}(1 + z\langle\cos\theta\rangle)$$

where N is the number of dipoles per unit volume, μ is the dipole moment of molecule, z is the coordination number (the number of interacting dipoles), and θ is the angle between the interacting dipoles. This was successfully applied for the water liquid; its large dielectric constant of 80 is reproducible by $z = 4$ and $\langle \cos\theta \rangle = 0.5$. In the ferroelectric copolymer based on vinylidene cyanide, $z = 30$ and $\langle \cos\theta \rangle = 0.62$ were elucidated to explain the high dielectric constant of 130.[21] On the analogy, it is supposed that the huge $\Delta\varepsilon$ of the present molecular system may be attributable to the cooperative fluctuation of the large number of molecules $z = \sim 10^3$ which increases with the increase of domain size. The effect of the DC bias fields on the LF mode of the $SmAP_F$ phase was also studied. As shown in Figure 2-7(a), by applying the DC bias fields, the LF mode is quickly quenched. As a result, the HF mode can be clearly detected at 100 kHz. The disappearance of the LF mode is explained by the suppression of the dipoles' fluctuation due to the DC bias fields. Here, the cell thickness dependence is also observed on the critical voltage that suppresses the LF mode. The critical voltage is 0.40 $V\mu m^{-1}$ for a 3 μm-thick cell, 0.14 $V\mu m^{-1}$ for a 10 μm-thick cell, and 0.06 $V\mu m^{-1}$ for a 25 μm-thick cell (refer to Figures 2-7). This trend is the same as that reported by Guo et al.[10] but opposite to that reported by Shimbo et al.[24]

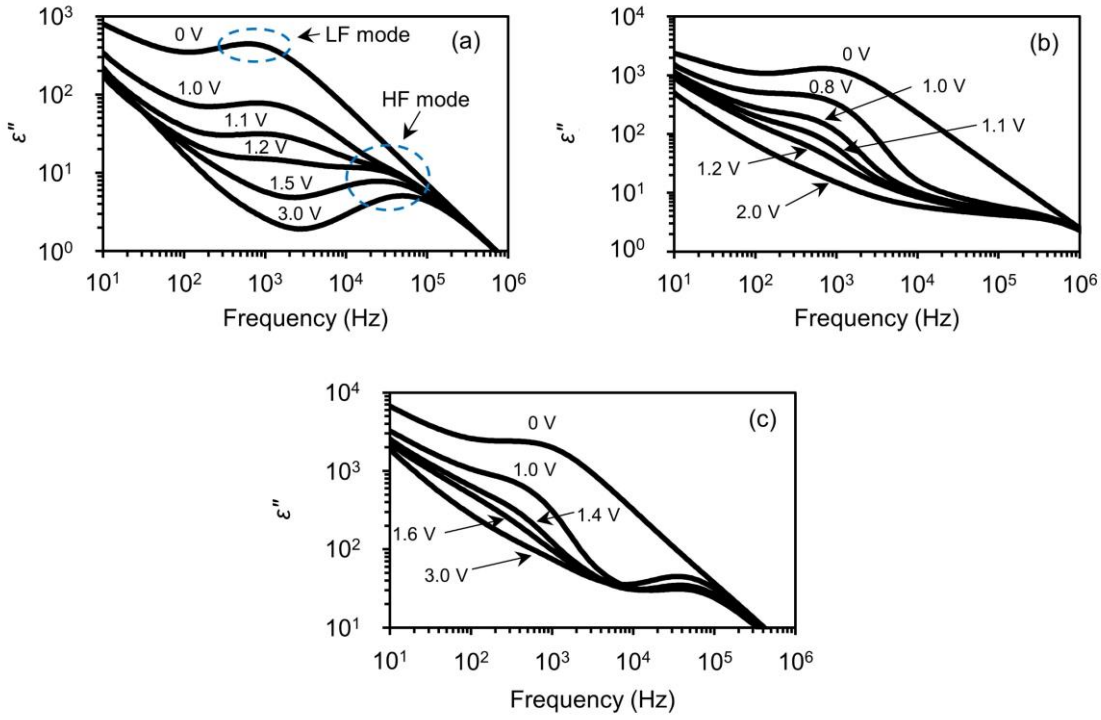

Figure 2-7. The imaginary (ε'') part of dielectric constants in the $SmAP_F$ phase measured under the DC bias fields in (a) a 3 μm-thick cell, (b) a 10 μm-thick cell, and (c) a 25 μm-thick cell. Their values are presented in a log scale.

2.4. Conclusions

In this chapter, the dielectric relaxation properties were studied for the $SmAP_F$ phase in the bent-shaped dimeric molecules mixture of 4OAM5AMO4 (forming the $SmCA^s$ phase) and 16OAM5AMO16 (forming the SmC_AP_A phase). Within a cell of the $SmAP_F$ phase, the bent-shaped dimeric molecules lie with their bent plane parallel to the surface. The $SmAP_F$ phase shows the LF mode at 500 Hz characteristic to the ferroelectric phase and a huge $\Delta\varepsilon$ of over 7000 in a 50 μm-thick cell, which is much higher compared to almost all the reported values in the bent-shaped molecules. The highly cooperative orientation of the bent-shaped dimeric molecule is considered to bring about the giant value of the $\Delta\varepsilon$. It is also characteristic of the LF mode that the cooperative fluctuation of dipoles is easily quenched under the DC bias fields.

References

(1) Izumi, T.; Kang, S.; Niori, T.; Takanishi, Y.; Takezoe, H.; Watanabe, J. Smectic mesophase behavior of dimeric compounds showing antiferroelectricity, frustration and chirality. *Jpn. J. Appl. Phys.* **2006**, *45*, 1506-1514.

(2) Izumi, T.; Naitou, Y.; Tokita, M.; Watanabe, J. Frustrated smectic phase appearing as transitional state between single-layer and antiferroelectric bilayer smectic phases in binary mixtures of dimeric compounds. *Jpn. J. Appl. Phys.* **2006**, *45*, 4991-4993.

(3) Izumi, T.; Naitou, Y.; Shimbo, Y.; Takanishi, Y.; Takezoe, H.; Watanabe, J. Several types of bilayer smectic liquid crystals with ferroelectric and antiferroelectric properties in binary mixture of dimeric compounds. *J. Phys. Chem. B* **2006**, *110*, 23911-23919.

(4) Niori, T.; Sekine, T.; Watanabe, J.; Furukawa, T.; Takezoe, H. Distinct ferroelectric smectic liquid crystals consisting of banana shaped achiral molecules. *J. Mater. Chem.* **1996**, *6*, 1231-1233.

(5) Takezoe, H.; Takanishi, Y. Bent-core liquid crystals: their mysterious and attractive world. *Jpn. J. Appl. Phys.* **2006**, *45*, 597-625.

(6) Watanabe, J.; Izumi, T.; Niori, T.; Zennyoji, M.; Takanishi, Y.; Takezoe, H. Smectic mesophase properties of dimeric compounds. 2. Distinct formation of smectic structures with antiferroelectric ordering and frustration. *Mol. Cryst. Liq. Cryst.* **2000**, *346*, 77-86.

(7) Reddy, R. A.; Zhu, C.; Shao, R.; Korblova, E.; Gong, T.; Shen, Y.; Garcia, E.; Glaser, M. A.; Maclennan, J. E.; Walba, D. M. et al. Spontaneous ferroelectric order in a bent-core smectic liquid crystal of fluid orthorhombic layers. *Science* **2011**, *332*, 72-77.

(8) Gorecka, E.; Vaupotic, N.; Pociecha, D. in Handbook of Liquid Crystals, ed. Goodby, J. W.; Collings, P. J.; Kato, T.; Tschierske, C.; Gleeson, H. F.; Raynes, P. Wiley-VCH Verlag GmbH & Co. KGaA., Germany, 2nd edition **2014**, *13*, 1-33.

(9) Tayi, A. S.; Kaeser, A.; Matsumoto, M.; Aida, T.; Stupp, S. I. Supramolecular ferroelectrics. *Nature Chemistry* **2015**, *7*, 281-294.

(10) Guo, L.; Gorecka, E.; Pociecha, D.; Vaupotič, N.; Čepič, M.; Reddy, R. A.; Gornik, K.; Araoka, F.; Clark, N. A.; Walba, D. M. et al. Ferroelectric behavior of orthogonal smectic

phase made of bent-core molecules. *Physical Review E* **2011**, *84*, 031706.

(11) Filipič, C.; Carlsson, T.; Levstik, A.; Žekš, B.; Blinc, R.; Gouda, F.; Lagerwall, S. T.; Skarp, K. Dielectric properties near the smectic-C*–smectic-A phase transition of some ferroelectric liquid-crystalline systems with a very large spontaneous polarization. *Phys. Rev. A* **1988**, *38*, 5833-5839.

(12) Khened, S.; Prasad, S.; Shivkumar, B.; Sadashiva, B. K. Dielectric studies of Goldstone mode and soft mode in the vicinity of the A-C* transition. *J. Phys. II France* **1991**, *1*, 171–180.

(13) Hiraoka, K.; Takezoe, H.; Fukuda, A. Dielectric relaxation modes in the antiferroelectric smectic CA* phase. *Ferroelectrics* **1993**, *147*, 13–25.

(14) Hatano, J.; Hanakai, Y.; Furue, H.; Uehara, H.; Saito, S.; Murashiro, K. Phase sequence in smectic liquid crystals having fluorophenyl group in the core. *Jpn. J. Appl. Phys.* **1994**, *33*, 5498–5502.

(15) Cole, K.; Cole, R. Dispersion and absorption in dielectrics I, alternating current characteristics, *J. Chem. Phys.* **1941**, *9*, 341–351.

(16) Marik, M.; Jana, D.; Majumder, K.; Chaudhuri, B. K. Dielectric behavior in B1 and B2 phases composed of unsymmetrical bent shaped liquid crystal molecules. *Mol. Cryst. Liq. Cryst.* **2015**, *606*, 111–125.

(17) Różański, S. Dielectric properties of liquid crystal formed by laterally fluorine-substituted banana-shaped molecules, *Phase Transitions* **2018**, *91*, 1007–1016.

(18) Kumar, J.; Prasad, C. Ferroelectric nematic and ferrielectric smectic mesophases in an achiral bent-core azo compound. *J. Phys. Chem. B* **2018**, *122*, 2998–3007.

(19) Fuente, M.; Dunmur, D. Dielectric Properties of Liquid Crystals. In *Handbook of liquid crystals*, 2nd ed.; Goodby, J.; Collings, P.; Kato, T.; Tschierske, C.; Gleeson, H.; Raynes, P., Eds.; Wiley-VCH Verlag GmbH & Co KGaA: Germany, 2014; pp 1−46.

(20) Ozaki, M.; Yoshino, K.; Sakurai, T.; Mikami, N.; Higuchi, R. Dielectric properties of new stable ferroelectric liquid crystals with large spontaneous polarization. *J. Chem. Phys.* **1987**, *86*, 3648-3654.

(21) Kirkwood, J. G. The dielectric polarization of polar liquids. *J. Chem. Phys.* **1939**, *7*, 911-919.

(22) Furukawa, T. Nonlinear dielectric and conductive spectra of polymers. *Makromol. Chem., Macromol. Symp.*, **1993**, *70/71*, 183-192.

(23) Ohigashi, H.; Omote, K.; Abe, H.; Koga, K. Chain motions in the paraelectric phase in single crystalline films of vinylidene fluoride and trifluoroethylene copolymer P(VDF/TrFE). *J. Phys. Soc. Jpn.* **1999**, *68*, 1824-1827.

(24) Shimbo, Y.; Gorecka, E.; Pociecha, D.; Araoka, F.; Goto, M.; Takanishi, Y.; Ishikawa, K.; Mieczkowski, J.; Gomola, K.; Takezoe, H. Electric-Field-Induced Polar Biaxial Order in a Nontilted Smectic Phase of an Asymmetric Bent-Core Liquid Crystal, *Phys. Rev. Lett.* **2006**, *97*, 113901.

CHAPTER 3

Electric Switching Behaviors and Dielectric Relaxation Properties in Ferroelectric, Antiferroelectric and Paraelectric Smectic Phases of Bent-Shaped Dimeric Molecules

3.1. Introduction

In a typical α,ω-bis(4-alkoxyanilinebenzylidene-4′-carbonyloxy)pentanes (mOAM5AMOm), the mixture of 4OAM5AMO4 forming the $SmCA^s$ phase and 16OAM5AMO16 forming the SmC_AP_A phase forms $SmAP_F$, $SmAP_A$, and SmA phases depending on the mixture ratio.[1]

In Chapter 2, the characteristic dielectric properties focusing on the $SmAP_F$ phase was described. The $SmAP_F$ phase exhibited the collective fluctuation mode of dipoles at around 500 Hz, which possesses a huge dielectric strength ($\Delta\varepsilon$). The $\Delta\varepsilon$ varies with the cell thickness and reaches a value higher than 7000 in a 50 μm-thick cell, which is much higher than almost all the reported values in bent-shaped molecules.[2,3] The highly cooperative fluctuation of dipoles is considered to bring about the giant value of $\Delta\varepsilon$.

In this chapter, the interesting insights which are of importance for the design of high dielectric constants by observing the electric switching behaviors and the dielectric properties of the $SmAP_F$, $SmAP_A$, and SmC_AP_A and SmA phases are provided.

3.2. Experimental Section

The bent-shaped dimeric molecules of 4OAM5AMO4 and 16OAM5AMO16 were synthesized following methods reported in a previous report.[4] Mixtures of the two molecules were prepared by evaporating chloroform solutions containing the two molecules at a predetermined molar ratio. The mixture is abbreviated as M-X, where X indicates the mol% fraction of 16OAM5AMO16. The phase behavior was examined for mixtures with X more than 25%, which can form the ferro- and antiferroelectric smectic phases.[1] The phase transition temperatures were determined by differential scanning calorimetry (DSC) (SHIMADZU DSC-60 Plus) at a rate of 5 °Cmin^{-1} under cooling run. Texture observation and identification of the mesophases were carried out using a polarizing optical microscope (POM) (OLYMPUS BX53)

equipped with a hot stage and a temperature controller (Mettler Toledo FP 82HT). X-ray diffraction (XRD) measurements were performed using a Nano-viewer (Rigaku) with Cu K_α radiation. The homeotropically aligned sample for XRD measurements was prepared as droplets on the glass substrate coated with commercially available trimethoxy(octadecyl)silane. Electrooptical and dielectric investigations were performed using glass cells coated with indium tin oxide (ITO) electrodes, which is commercially available from EHC Co., Ltd. The area of the ITO electrodes was 100 mm^2, and the cell thicknesses of the ITO electrodes were 3 μm, 10 μm, 25 μm, 50 μm and 80 μm. Basic data were collected by using the 3 μm-thick cell unless otherwise specified. In these ITO cells, the bent-shaped dimeric molecules were homogeneously aligned with the molecular axis and the bent plane parallel to the cell plane (shown in details later). The polarization reversal current was observed by applying a triangular wave voltage using a high-speed amplifier (FLC Electronics, F20A) connected to a function generator (NF Electronic Instruments, WF1945B). Before the dielectric relaxation measurements, the AC electric field in the $SmAP_F$, $SmAP_A$ and SmC_AP_A phases were applied at 5 $V_{pp}\mu m^{-1}$, 5 $V_{pp}\mu m^{-1}$ and 33 $V_{pp}\mu m^{-1}$, respectively, and sweeping with frequencies of 10–1000 Hz in 300 log steps to increase the domain size. The complex dielectric constants were measured in a frequency range between 10^1 Hz and 10^7 Hz with the impedance analyzer (NF Electronic Instruments, FRA51615). The electric voltage for the measurement was 1 V_{pp}.

3.3. Results and Discussion

3.3.1. Phase behaviors of the SmA, $SmAP_F$, $SmAP_A$ and SmC_AP_A phases

The phase behavior in M-X mixtures with X more than 25 is shown in Figure 3-1, which includes four types of smectic phases, the SmC_AP_A, $SmAP_A$, $SmAP_F$ and SmA phases. Transition temperatures from Iso to Sm and Sm to solid (dark) phases were well collected using the DSC. On the other hand, the SmA-$SmAP_F$ and $SmAP_F$-$SmAP_A$ transitions are hardly

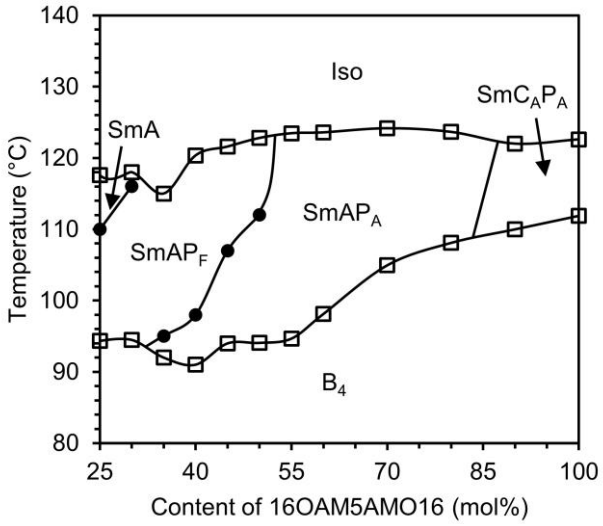

Figure 3-1. Phase behavior in binary mixtures of 4OAM5AMO4 and 16OAM5AMO16. Transition temperatures are collected using the DSC (□) and POM (●) (refer to the text).

identified from the DSC measurement because of the very small enthalpy change. Additionally, these transitions are well recognized from the clear change of optical microscopic textures in the homeotropic aligned cell.[1] Here, the SmA shows totally dark texture, while the $SmAP_F$ exhibits the birefringent schlieren texture. The $SmAP_A$ also shows the schlieren texture, and its transformation to the $SmAP_F$ can be detected from the violent fluctuation of schlieren texture. In the banana molecule, the non-tilted smectic phases (SmAP) have been found with transitions

Table 3-1. Thermodynamic data for phase transition temperatures and associated enthalpies and layer spacings in mixtures of 4OAM5AMO4 and 16OAM5AMO16.

Contents of 16OAM5AMOC16	Transition temperature / °C (enthalpy / $kJmol^{-1}$)						Layer Spacing / Å
	B_4	$SmAP_A$	$SmAP_F$	SmA	SmC_AP_A	Iso	LC phase
100	● 111.9 (72.9)	-	-	-	● 122.6 (21.4)	●	56.9
90	● 110.0 (60.4)	-	-	-	● 122.0 (19.8)	●	55.4
80	● 108.1 (62.0)	● 123.7 (18.4)	-	-	-	●	57.1
70	● 105.0 (65.8)	● 124.2 (17.3)	-	-	-	●	54.9
60	● 98.1 (59.8)	● 123.6 (15.7)	-	-	-	●	52.7
55	● 94.7 (57.6)	● 123.5 (15.3)	-	-	-	●	51.3
50	● 94.1 (54.3)	● 112.0 (-)	● 122.8 (14.1)	-	-	●	50.7 ($SmAP_A$) 50.7 ($SmAP_F$)
45	● 94.0 (52.6)	● 107.0 (-)	● 121.6 (13.2)	-	-	●	50.4 ($SmAP_A$) 50.4 ($SmAP_F$)
40	● 91.0 (49.3)	● 98.0 (-)	● 120.4 (8.4)	-	-	●	50.1 ($SmAP_A$) 50.1 ($SmAP_F$)
35	● 92.0 (44.6)	● 95.0 (-)	● 115.0 (12.3)	-	-	●	48.4 ($SmAP_A$) 48.4 ($SmAP_F$)
30	● 94.5 (42.4)	-	● 116.0 (-)	● 118.0 (12.0)	-	●	46.4 ($SmAP_F$) 38.0 (SmA)
25	● 94.3 (38.2)	-	● 110.0 (-)	● 117.6 (10.0)	-	●	46.6 ($SmAP_F$) 38.4 (SmA)

from the paraelectric SmA with short–range polar order via intermediate $SmAP_R$ phases with random polarization to polar the $SmAP_A$ and $SmAP_F$ with long-range polar order. [5–7]

The phase behavior is essentially the same as that previously reported[1] (Table 3-1), and a more in-depth analyses are provided here. The SmC_AP_A phase is observed only in the narrow region of 100 mol% to 90 mol% of 16OAM5AMO16. The $SmAP_A$ phase is formed in the region of 80 mol% to 35 mol%, and the $SmAP_F$ phase is in the region of 50 mol% to 25 mol%. The mixtures of 35–50 mol%, hence, show the dimorphism forming the $SmAP_A$ and $SmAP_F$ in order of increasing temperature. Another dimorphism of $SmAP_F$ and SmA is observed in the mixtures of 25 mol% and 30 mol% where the SmA exists in a higher temperature region than the $SmAP_F$. The lowest-temperature solid phase appearing from these smectic phases is totally transparent by naked eyes and shows weak birefringent (dark) texture in a cross-polarized microscopic observation. It is also characterized by exhibiting the chiral domains with a slight rotation of polarizer from the cross-polarization position. This solid phase, hence, can be classified into the same phase as B_4 in the bent-shaped molecules.[8]

3.3.2. Electric switching behaviors of the $SmAP_F$, $SmAP_A$ and SmC_AP_A phases

The smectic phases show the fan-shaped textures on cooling from isotropic phase in all ITO-coated cells. The result implies the molecules prefer the homogeneous alignment on the ITO surface. In other words, the smectic layers are constructed in a direction perpendicular to the cell surface. Although the fan-shaped domain size is small in a cell as it cooled from the isotropic phase, it can be well enlarged by applying an AC field higher than the threshold electric field (E_{th}) of ferroelectric switching. This is due to the coalescence of domains by an agitation of molecular motion through the switching. The electric switching and dielectric measurements were performed for these treated cells.

On applying the DC field for ferroelectric switching, two characteristic changes of textures can be observed. Typical optical microscopic textures observed in the $SmAP_F$ of M-50 are shown in Figure 3-2. First, the birefringence colors change while maintaining the fan-shaped domains and are reversible on field-on and field-off. The color change is attributed to the change of birefringence (Δn). As described in Chapter 2, the Δn is estimated to be 0.07 at 0 V μm^{-1} and 0.18 at 1 V μm^{-1}. This indicates that the bent (polar) direction of molecules is initially parallel to the cell's surface and changes to be perpendicular to the surface after switching. Secondly, fine stripes running across the long axis of fan-shape domains at a field-off state are well observed in a thick cell (Figure 3-2(a)). Interestingly, as found in Figure 3-2(b), these stripes disappear completely on switching. Such stripes can be considered as polarization splay defects. Since the polar (bent) directions initially align parallel to the cell surface, two kinds of domains with opposite polar directions are necessarily encountered when they evolve from the isotropic melt. Hence, the boundaries, i.e., polarization splay defects, are created by degeneracy of the opposite directed polarization as illustrated in Figure 3-2(c). At the center of the boundary, the polar direction of the molecules is perpendicular to the surface. On applying the DC field, bent

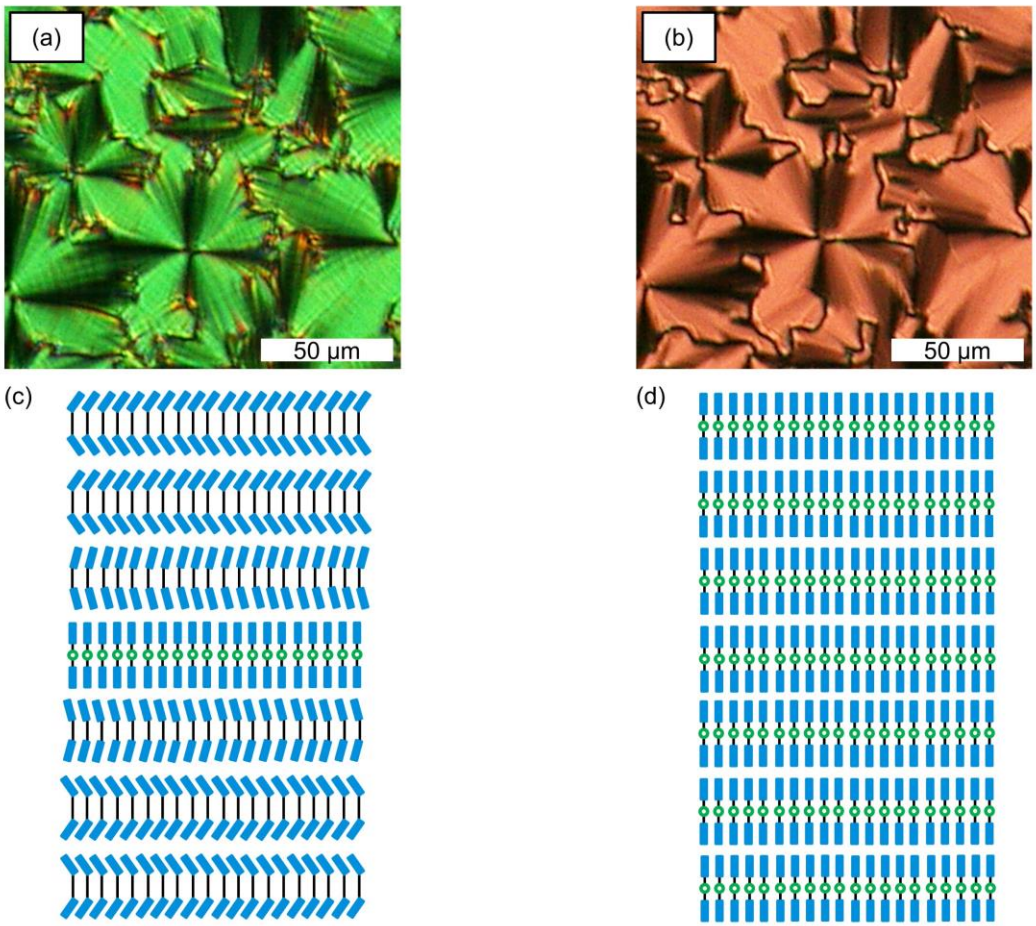

Figure 3-2. Optical textures in the $SmAP_F$ phase of M-50 in a 10 μm-thick cell (a) at 0 $V\mu m^{-1}$ and (b) at 1 $V\mu m^{-1}$. (c) Molecular packing in polarization splay defect of the $SmAP_F$ phase in the ground state and (d) molecular packing when the electric field is applied.

directions of all the molecules change to be standing up against the surface (see Figure 3-2(d)), then, the stripes (i.e., defects) disappear without changing the fan-shape textures. Thus, the switching is expected to take place in a way that the bent directions initially parallel to the cell surface change to be perpendicular to the surface without changing the homogeneous alignment of molecular axes. Similar characteristic changes in texture were observed in the $SmAP_A$.

Figures 3-3(a)–(c) show the typical polarization switching currents of the $SmAP_F$ in M-35, $SmAP_A$ in M-70, and SmC_AP_A in M-100, respectively, measured under a triangular wave voltage application. As expected, the ferroelectric $SmAP_F$ shows one current peak on half a cycle, while the antiferroelectric $SmAP_A$ and SmC_AP_A phases show two current peaks. The reversal polarization (equal to $2P_s$) is about 700 $nCcm^{-2}$ independent of the phase type. Interestingly, the E_{th} at the top of the current peak is dependent on the phase type. As given in Figures 3-3(a)–(c), the E_{th} of the $SmAP_F$ is very low, 0.7 $V\mu m^{-1}$, and that of the $SmAP_A$ is 2.0 $V\mu m^{-1}$. In contrast, the E_{th} of the SmC_AP_A is relatively high, 9.3 $V\mu m^{-1}$. These values are independent on the temperature. In Figure 3-3(d), E_{th}'s collected for all mixtures are plotted against the mixture content. The plotting reveals the E_{th} does not depend on the mixture content,

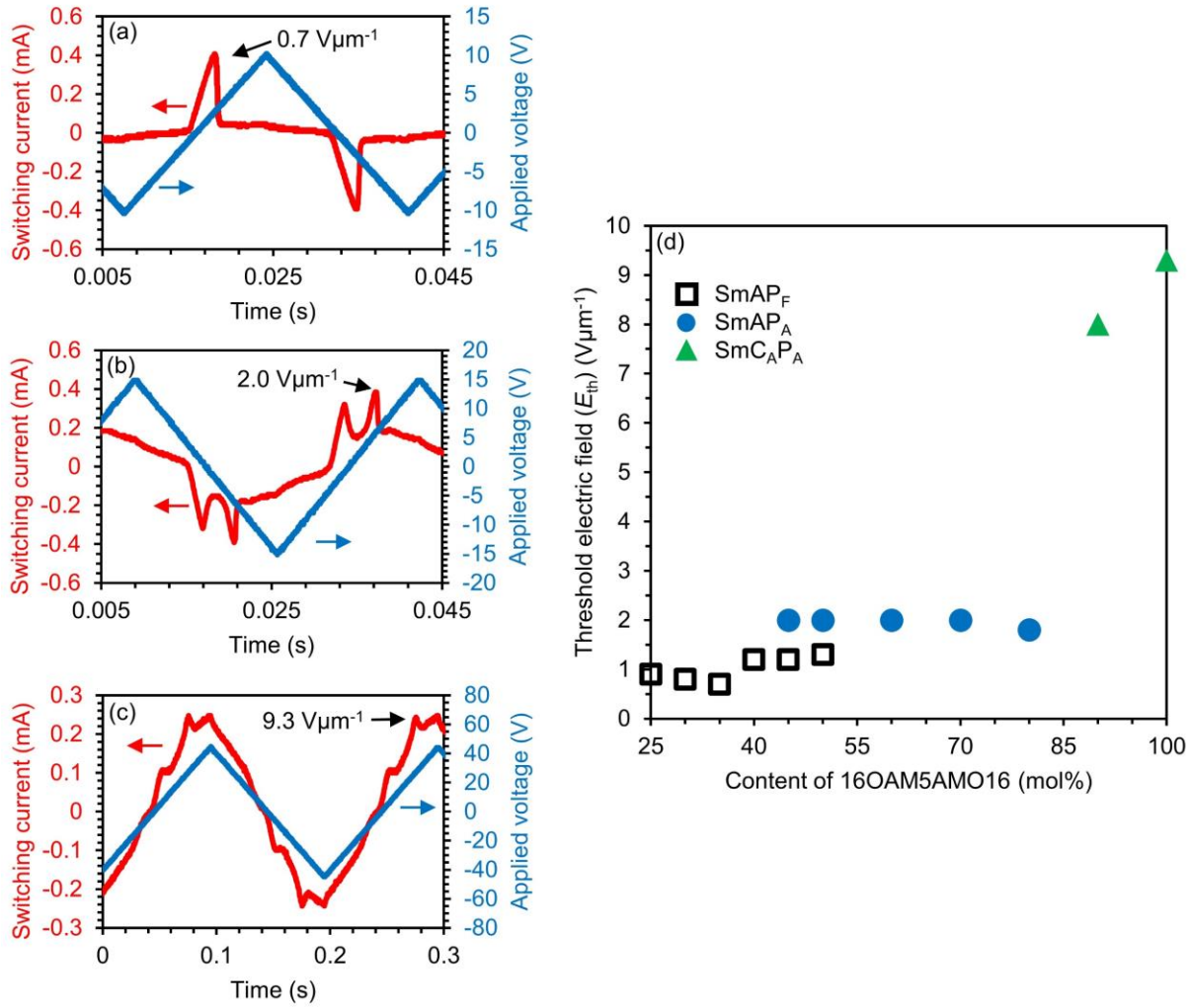

Figure 3-3. Polarization reversal current responses observed for (a) the $SmAP_F$ phase in M-35 by applying a triangle-wave field (20 V_{pp}, 30 Hz), (b) the $SmAP_A$ phase in M-70 by applying a triangle-wave field (30 V_{pp}, 30 Hz) and (c) the SmC_AP_A phase in M-100 by applying a triangle-wave field (90 V_{pp}, 5 Hz), measured in a 3 μm-thick cell. (d) Mixture content dependence of the E_{th} in the $SmAP_F$, $SmAP_A$ and SmC_AP_A phases, measured in a 3 μm-thick cell.

but on the type of phases.

Figure 3-4 shows the cell thickness dependence of the E_{th} (refer to Figures 3-5 and 3-6 presenting the detailed polarization reversal current responses in the $SmAP_F$ and $SmAP_A$ phases of M-50). Here, the dependences were examined for the $SmAP_F$ and $SmAP_A$, but not for the SmC_AP_A because of the requirement of a high field. The E_{th} decreases with increasing the cell thickness from 3 μm to 80 μm. The trend is more significant for the $SmAP_F$; the E_{th} becomes almost zero (0.1 $V\mu m^{-1}$) in a cell of 80 μm thickness. The E_{th} of the $SmAP_A$ also becomes small, around 0.6 $V\mu m^{-1}$. Such a remarkable cell thickness dependence suggests that the response of the $SmAP_F$ to an electric field is inherently thresholdless (free rotation of the polar director around molecular axis). The weak threshold nature may arise from interactions at cell surfaces and the fan-shape domain boundary, the effect of which becomes weakened when the cell

thickness increases followed by an increase in the domain size. In contrast to these, the SmC_AP_A shows a high E_{th}, which is considered to result from the tilting of the molecules to the layer.

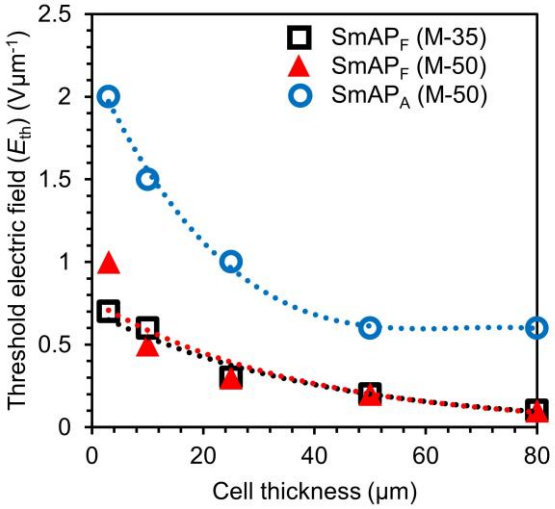

Figure 3-4. Cell thickness dependence of the E_{th} in the $SmAP_F$ phase of M-35 and 50, and $SmAP_A$ phase of M-50. The dotted curves are guides for the eyes.

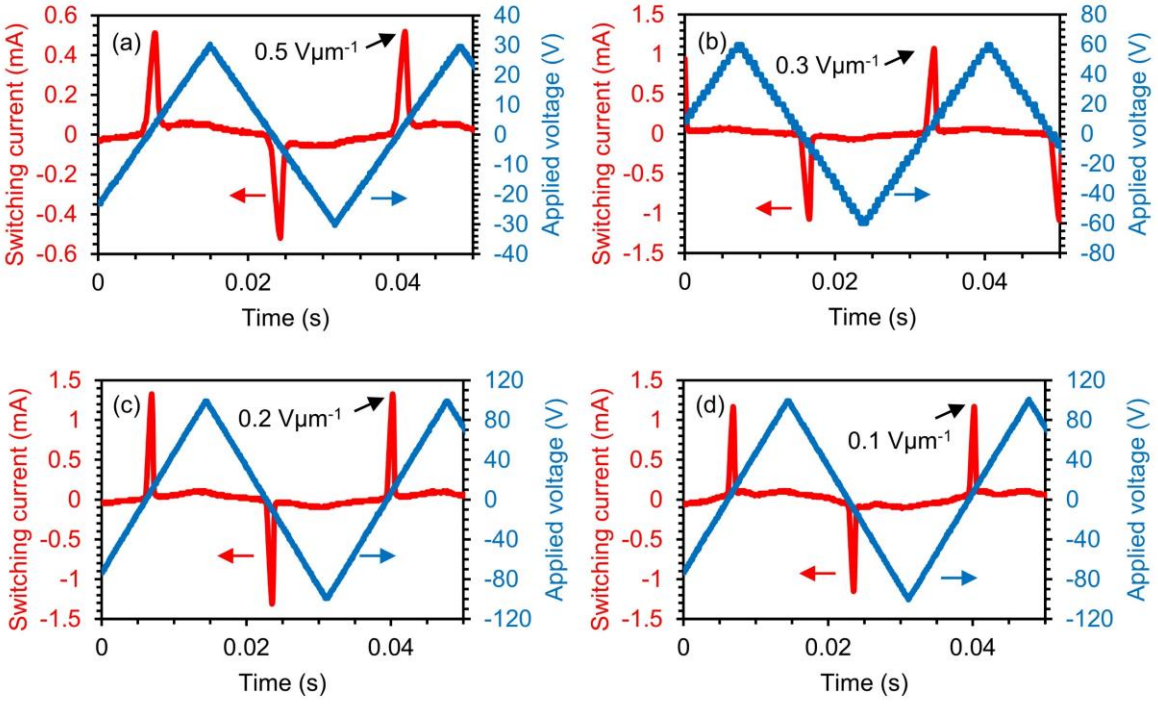

Figure 3-5. Polarization reversal current responses observed for the $SmAP_F$ phase in M-50 (a) in a 10 μm-thick cell by applying a triangle-wave field (60 V_{pp}, 30 Hz), (b) in a 25 μm-thick cell by applying a triangle-wave field (120 V_{pp}, 30 Hz), (c) in a 50 μm-thick cell by applying a triangle-wave field (200 V_{pp}, 30 Hz) and (d) in a 80 μm-thick cell by applying a triangle-wave field (200 V_{pp}, 30 Hz).

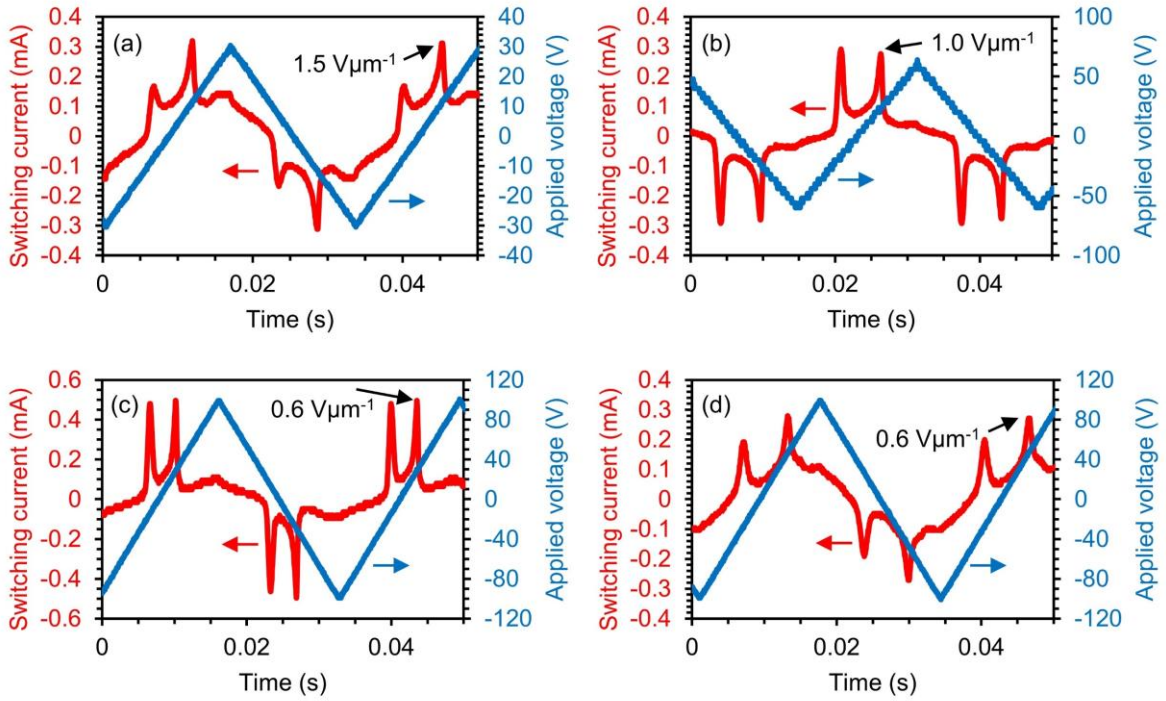

Figure 3-6. Polarization reversal current responses observed for the $SmAP_A$ phase in M-50 (a) in a 10 μm-thick cell by applying a triangle-wave field (60 V_{pp}, 30 Hz), (b) in a 25 μm-thick cell by applying a triangle-wave field (120 V_{pp}, 30 Hz), (c) in a 50 μm-thick cell by applying a triangle-wave field (200 V_{pp}, 30 Hz) and (d) in a 80 μm-thick cell by applying a triangle-wave field (200 V_{pp}, 30 Hz).

3.3.3. Dielectric properties

The dielectric measurements were performed for four types of the smectic phases. Figures 3-7(a) and (b) show their typical dielectric data, as observed for the SmA of M-25, $SmAP_F$ of M-35, $SmAP_A$ of M-70, and SmC_AP_A of M-100, where the real (ε') and imaginary (ε'') parts of the dielectric constants are plotted against the frequencies of 10^1 Hz to 10^7 Hz, respectively. Two relaxation modes can be observed in this frequency range. One is the low frequency (LF) mode, which is observed at approximately 500 Hz in the $SmAP_F$ and at 2000 Hz in the $SmAP_A$. These high dielectric constants and low relaxation frequencies (f_r) reveal that the mode is the collective fluctuation mode of polarization, which is typically observed in the ferroelectric and antiferroelectric phases.[2,9–13] Another is the high frequency (HF) mode appearing at approximately 100 kHz, which is observed in the paraelectric SmA phase and SmC_AP_A phase. It is attributable to the non-collective molecular rotation around the short axes of mesogens as commonly observed in conventional liquid crystal (LC) phases.[11–13] The similar HF mode is described in the non-polar $SmCA^s$ of M-0 in Chapter 2. This HF mode may also exist in the $SmAP_F$ and $SmAP_A$ phases, but may be hidden by the LF mode with the huge dielectric constants. In fact, it can be detected when the LF modes are suppressed by the DC bias application as mentioned later.

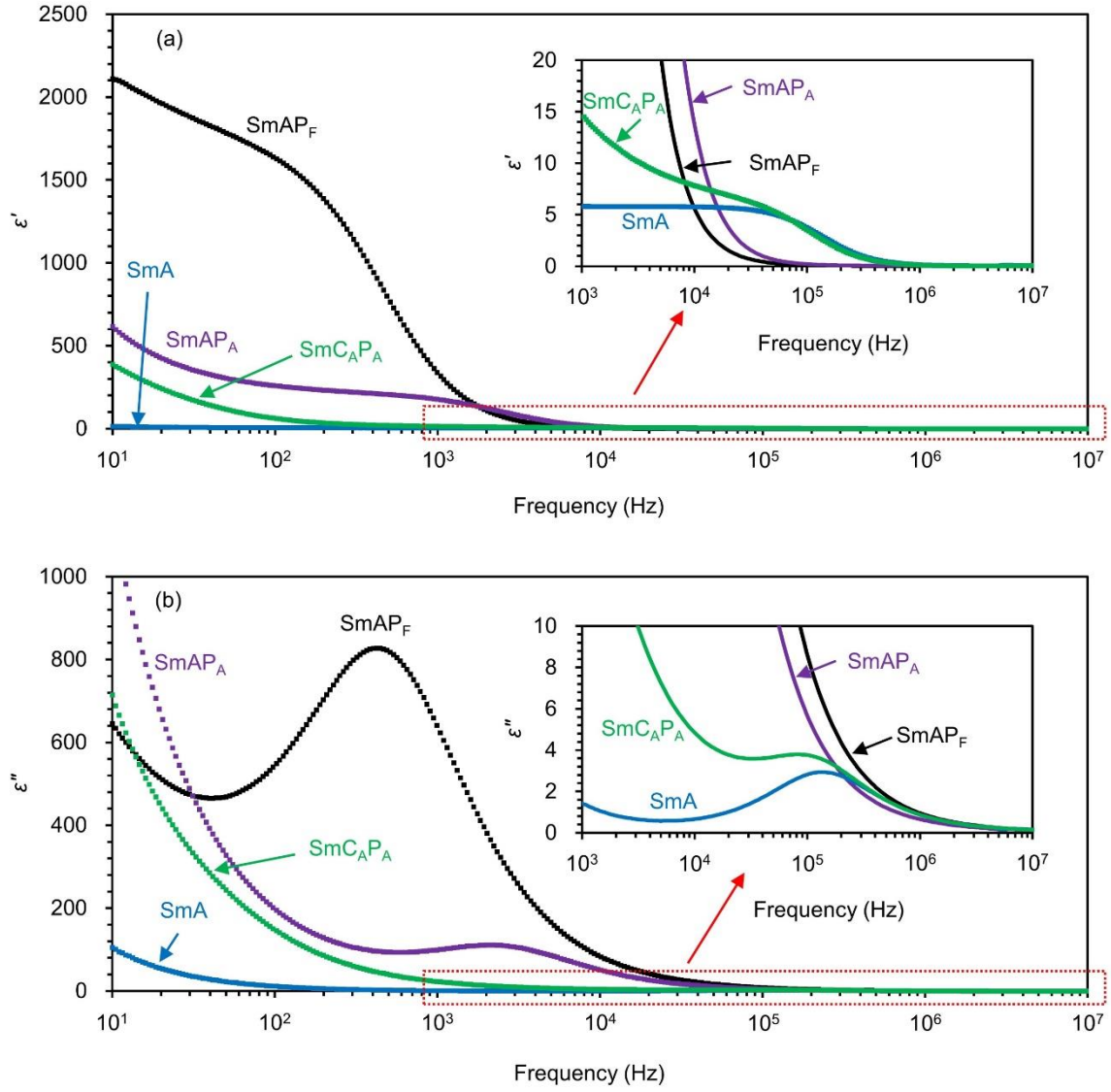

Figure 3-7. Frequency dependences of (a) the real (ε') part and (b) imaginary (ε'') part of the complex dielectric constants in the $SmAP_F$ phase of M-35, $SmAP_A$ phase of M-70, SmC_AP_A phase of M-100 and SmA phase of M-25, measured in a 3 μm-thick cell. In the insets, the vertical axis is expanded to clarify the dielectric relaxation modes of the SmC_AP_A and SmA phases at around 10^5 Hz.

The dielectric spectra were analyzed by fitting with the following Cole-Cole equation[14]:

$$\varepsilon^* = \varepsilon' - i\varepsilon'' = \varepsilon_\infty + \frac{\Delta\varepsilon}{1 + (i\omega\tau)^{1-\alpha}} \quad 0 < \alpha < 1, \qquad (3-1)$$

where ω is the angular frequency, $\Delta\varepsilon$ (= ε_s - ε_∞) is the dielectric strength, and ε_s and ε_∞ are the "static-frequency" and "infinite-frequency" dielectric constants, respectively. $\tau = 1/(2\pi f_r)$ is the relaxation time (where f_r is the relaxation frequency), and α is the distribution parameter of relaxation time. For $\alpha = 0$, the Cole-Cole model reduces to the Debye model. Figure 3-8 shows the Cole-Cole plots for the LF and HF modes. The determined parameters, $\Delta\varepsilon$, f_r and α, in the Cole-Cole equation are listed in Table 3-2. For the HF mode of the SmA and SmC_AP_A phases,

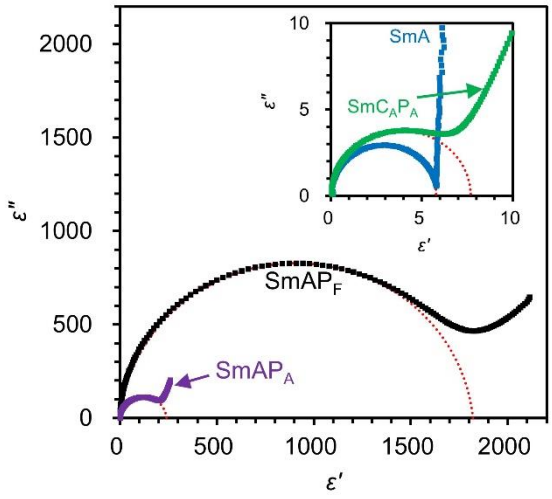

Figure 3-8. Cole-Cole plot for the $SmAP_F$ phase of M-35, $SmAP_A$ phase of M-70, SmC_AP_A phase of M-100 and SmA phase of M-25 based on the data of Figures 3-7(a) and (b). In the insets, the horizontal and vertical axes are expanded to clarify the Cole-Cole plots for the low frequency modes of SmC_AP_A and SmA phases. The dotted curves are obtained by fitting Equation (3-1).

α is almost zero. For the LF mode of the $SmAP_F$ and $SmAP_A$ phases, α is between 0.03 and 0.07. One noticeable point is that the $\Delta\varepsilon$ for the LF mode of the $SmAP_F$ and $SmAP_A$ phases are very large; 1820 for the $SmAP_F$ and 240 for the $SmAP_A$. On the other hand, the SmA and SmC_AP_A phases show $\Delta\varepsilon$ values less than 10, which is usually obtained for the HF mode.

The characteristic dielectric behaviors of the $SmAP_F$ and $SmAP_A$ can be also recognized through temperature variation for the M-35 and M-50 exhibiting the dimorphism of the $SmAP_F$ and $SmAP_A$. Figures 3-9(a) and (b) show the temperature dependence of the $\Delta\varepsilon$ and f_r as observed for the M-50. A clear transition can be recognized here through the change of the large

Table 3-2. List of the Cole-Cole parameters, the $\Delta\varepsilon$, f_r and α, collected from the data of Figures 3-7 and 3-8.

	$SmAP_F$	**$SmAP_A$**	**SmA**	**SmC_AP_A**
$\Delta\varepsilon$	1.8×10^3	2.4×10^2	5.7	7.6
f_r (Hz)	4.9×10^2	2.1×10^3	1.4×10^5	8.2×10^4
α	0.06	0.04	0	0

$\Delta\varepsilon$ (around 1400) to a relatively small $\Delta\varepsilon$ (around 200) on the cooling run. All the $\Delta\varepsilon$ and f_r of the $SmAP_F$, $SmAP_A$ and SmC_AP_A phases thus collected are plotted against the mixture composition in Figures 3-10(a) and (b), respectively. It can be seen that the $\Delta\varepsilon$ and f_r of each phase are almost the same without being greatly affected by the difference in the content as well as the temperature.

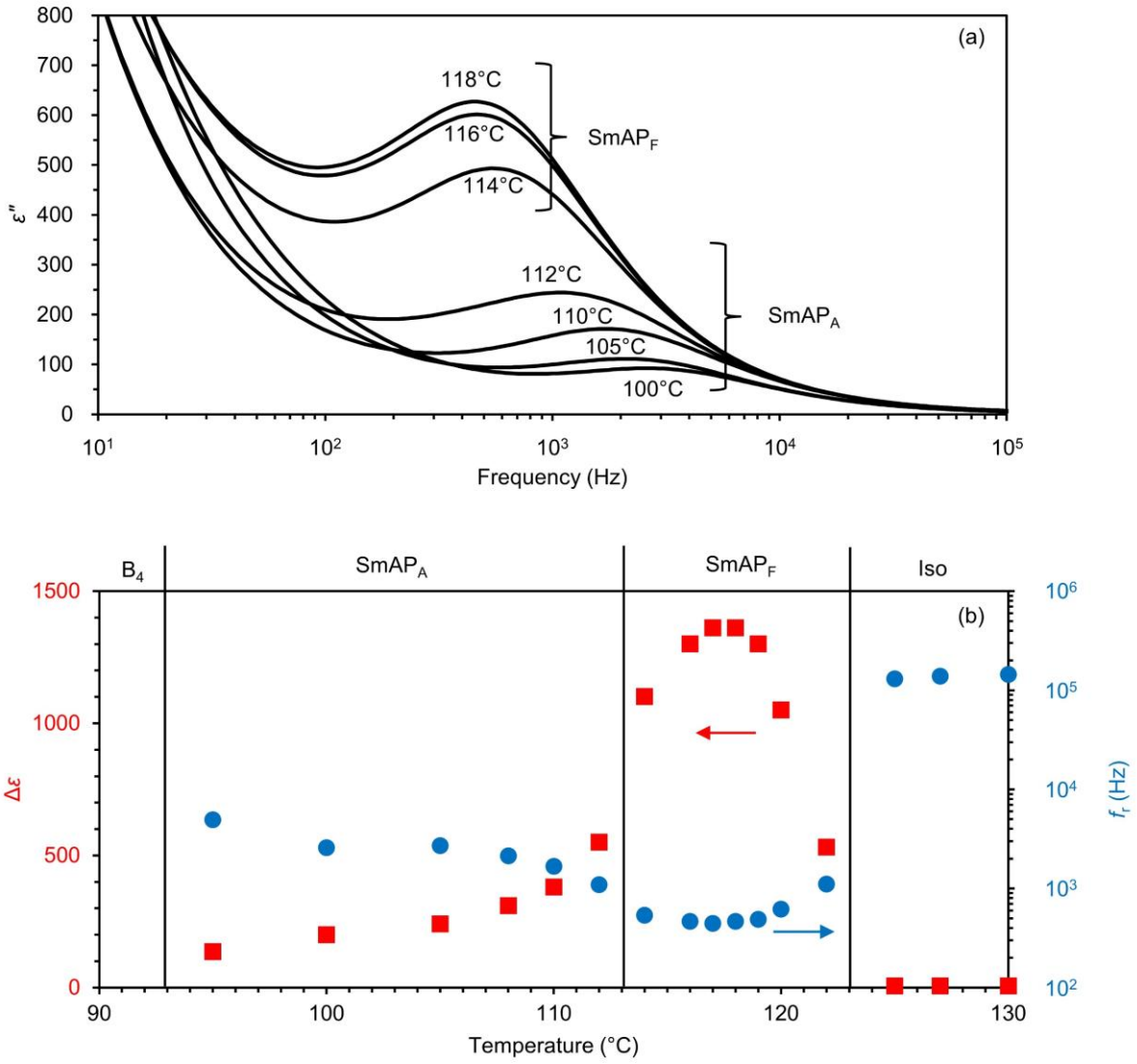

Figure 3-9. (a) The imaginary (ε'') part of dielectric constant in M-50, measured at various temperatures of the $SmAP_F$ and $SmAP_A$ phases in a 3 μm-thick cell and (b) temperature variation of the estimated $\Delta\varepsilon$ and f_r. In (b), the corresponding data of the non-collective mode in isotropic melt are included.

The exhibition of huge dielectric constants in the $SmAP_F$ is reliable as being due to the collective fluctuation of polar order (the LF mode). However, one may consider that the straight-forward collective mode of the $SmAP_A$ cannot be dielectrically detected since all the polar directions of layers turn around the molecule and keeping their antipolar order form layer to layer. One of the plausible explanations for this is provided that an anti-phase fluctuation of dipoles is likely to occur in adjacent layers; the molecules in neighboring layers fluctuate with a different sign of angle ($\Delta\psi$) that resulting in a temporary non-zero cancellation of neighboring dipoles.[15,16] The temperature dependence of the relaxation frequency, f_r, were examined for the LF and HF modes although their measurements were limited in a short temperature range of 10–20 °C (refer to Figure 3-11). The HF mode observed in the SmC_AP_A and SmA phases

follows the standard Arrhenius equation[17,18], and the activation energies are 40 kJmol^{-1} and 73 kJmol^{-1}, respectively. These values are comparable to those reported.[9] On the other hand, the f_r of the $SmAP_F$ and $SmAP_A$ phases is nearly temperature independent as expected for the LF mode.[2,8]

It is interesting to note that the $\Delta\varepsilon$ of the LF modes is strongly dependent on the cell thickness. As found in Figure 3-12, the $\Delta\varepsilon$ of the $SmAP_F$ phase grows almost linearly following an increase in the cell thickness from 3 μm to 80 μm, and reaches an extremely huge value of 10000 in the 80 μm-cell. Detailed dielectric relaxation data in the $SmAP_F$ and $SmAP_A$ phases of M-50 is

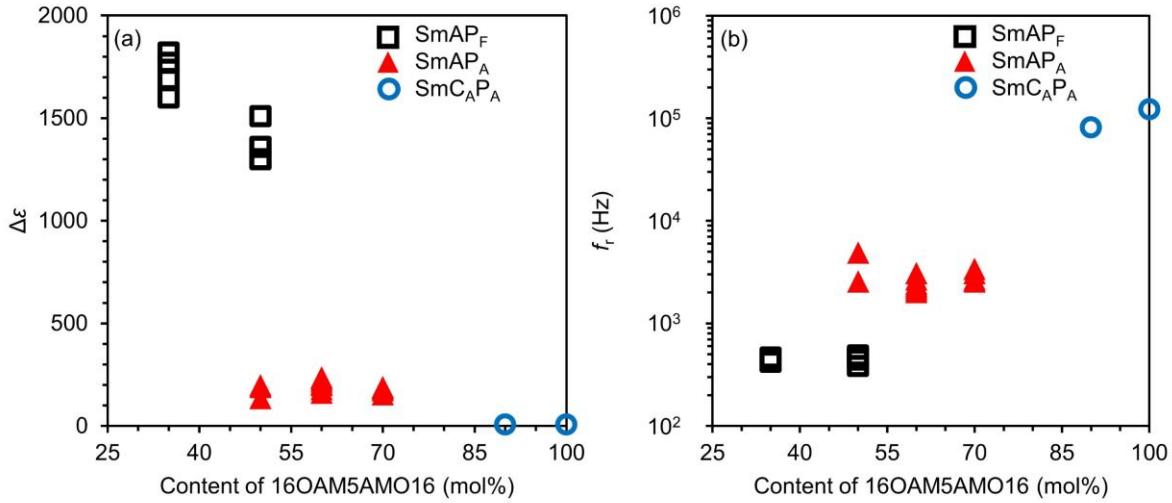

Figure 3-10. Mixture content dependence of (a) the $\Delta\varepsilon$ and (b) f_r for the collective modes of the $SmAP_F$ and $SmAP_A$ phases (measured in a 3 μm-thick cell). As reference, the $\Delta\varepsilon$ and f_r for the non-collective mode of SmC_AP_A phase are presented.

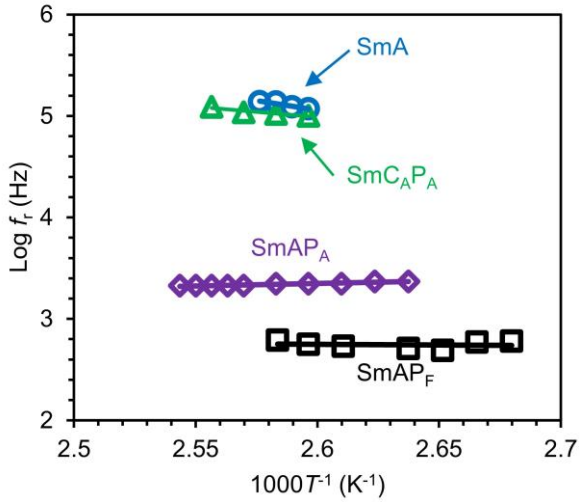

Figure 3-11. Logarithm of the dielectric relaxation frequencies as a function of inverse absolute temperature for the $SmAP_F$ of M-35, $SmAP_A$ of M-70, SmC_AP_A of M-100 and SmA of M-25 phases, measured in a 3 μm-thick cell.

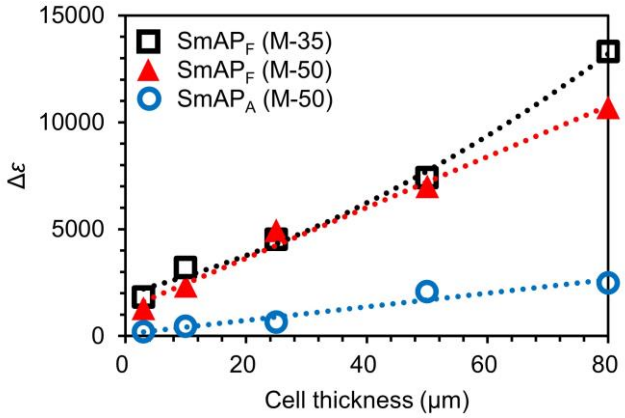

Figure 3-12. Cell thickness dependence of the $\Delta\varepsilon$ in the SmAP$_F$ phase of M-35 and 50, and SmAP$_A$ phase of M-50. The dotted curves are guides for the eyes.

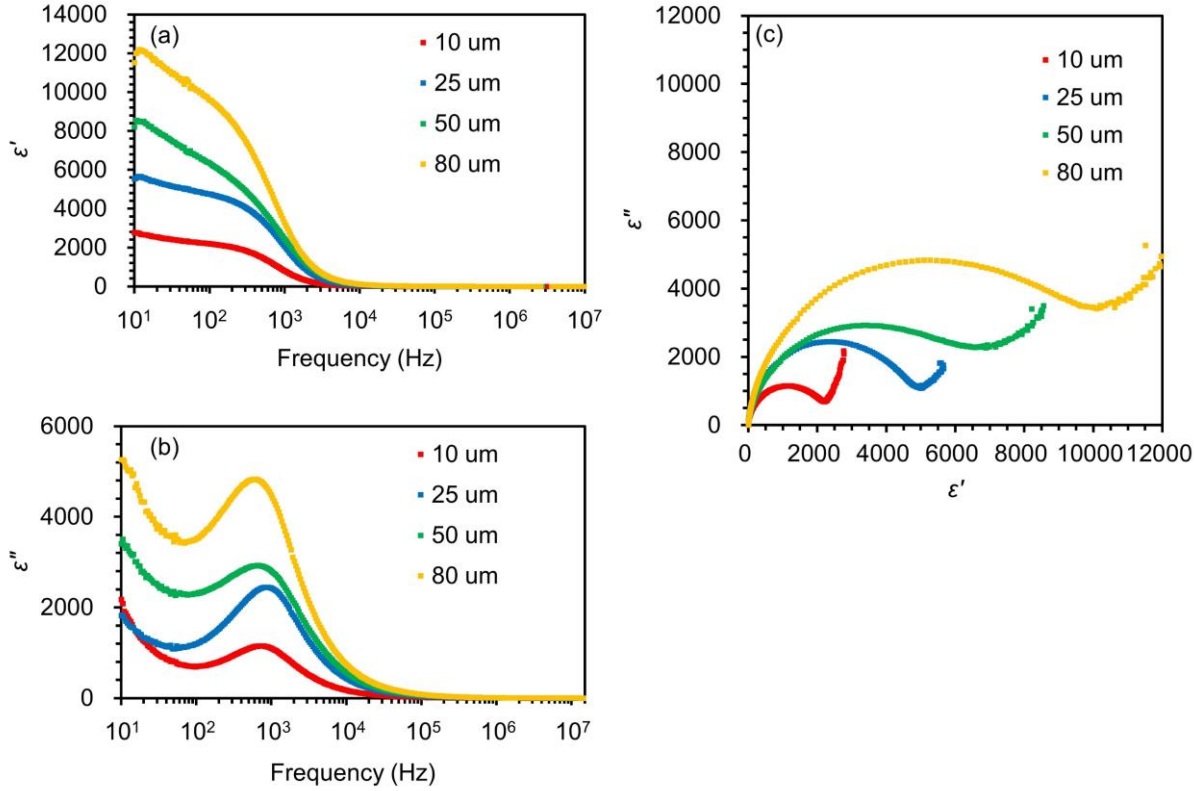

Figure 3-13. Frequency dependence of (a) the real part (ε') and (b) imaginary part (ε'') of the complex dielectric constants in the SmAP$_F$ phase from M-50 measured in 10, 25, 50 and 80 μm-thick cells, and (c) their Cole-Cole plot.

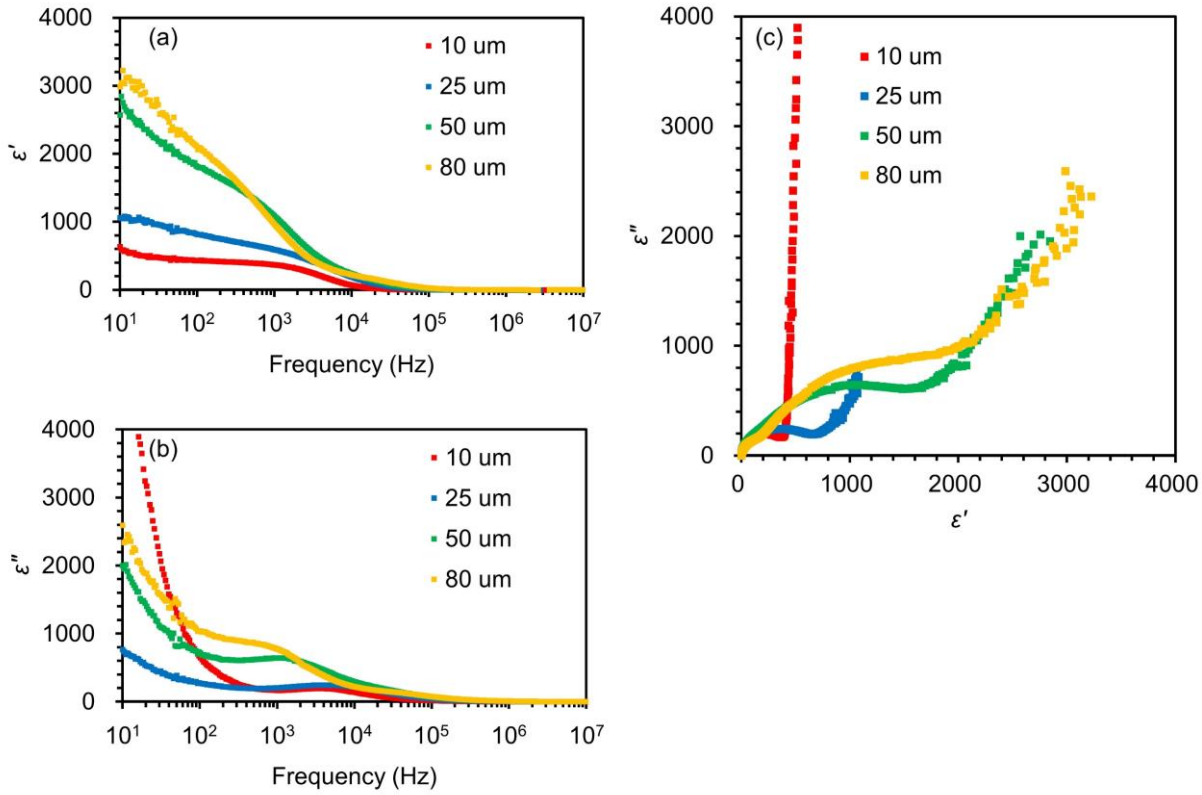

Figure 3-14. Frequency dependence of (a) the real (ε') part and (b) imaginary (ε'') part of the complex dielectric constants in the $SmAP_A$ phase of M-50 measured in 10, 25, 50 and 80 μm-thick cells, and (c) their Cole-Cole plot.

presented in Figures 3-13 and 3-14, respectively. A similar increment to 2000 can be seen in the $SmAP_A$, and the value is about one fifth part of $SmAP_F$. The increment of $\Delta\varepsilon$ with the cell thickness can be explained by a result of an increment in the correlation length of the LF mode which is ascribed to an increment of the smectic domain size in Chapter 2.

3.3.4. DC bias field effect on dielectric properties of the $SmAP_F$, $SmAP_A$ and SmC_AP_A phases

In order to obtain the information of electric-field-effects on the polar order, dielectric measurement was performed under DC bias fields. Figure 3-15(a) shows the variation of the $\Delta\varepsilon$ with the DC bias field typically observed in the $SmAP_F$ of M-35 and M-50. By applying the DC bias field, the $\Delta\varepsilon$ of the $SmAP_F$ phase decreases and then becomes almost zero at around 0.5 $V\mu m^{-1}$. As a result, the HF mode emerges clearly at 100 kHz. Considering 0.5 $V\mu m^{-1}$ roughly corresponds to the E_{th} of 0.7 $V\mu m^{-1}$ estimated from the electric switching, the disappearance of the LF mode is explained by the suppression of the dipoles' fluctuation due to the DC bias field.[2] On the other hand, the suppression behavior is not simple (refer to Figure 3-15(b)) for the $SmAP_A$ phase. The $\Delta\varepsilon$ and f_r are almost constant up to 0.9 $V\mu m^{-1}$. On further increase of the DC field from 0.9 $V\mu m^{-1}$ to 1.5 $V\mu m^{-1}$, a local maximum is observed in the $\Delta\varepsilon$, and a local

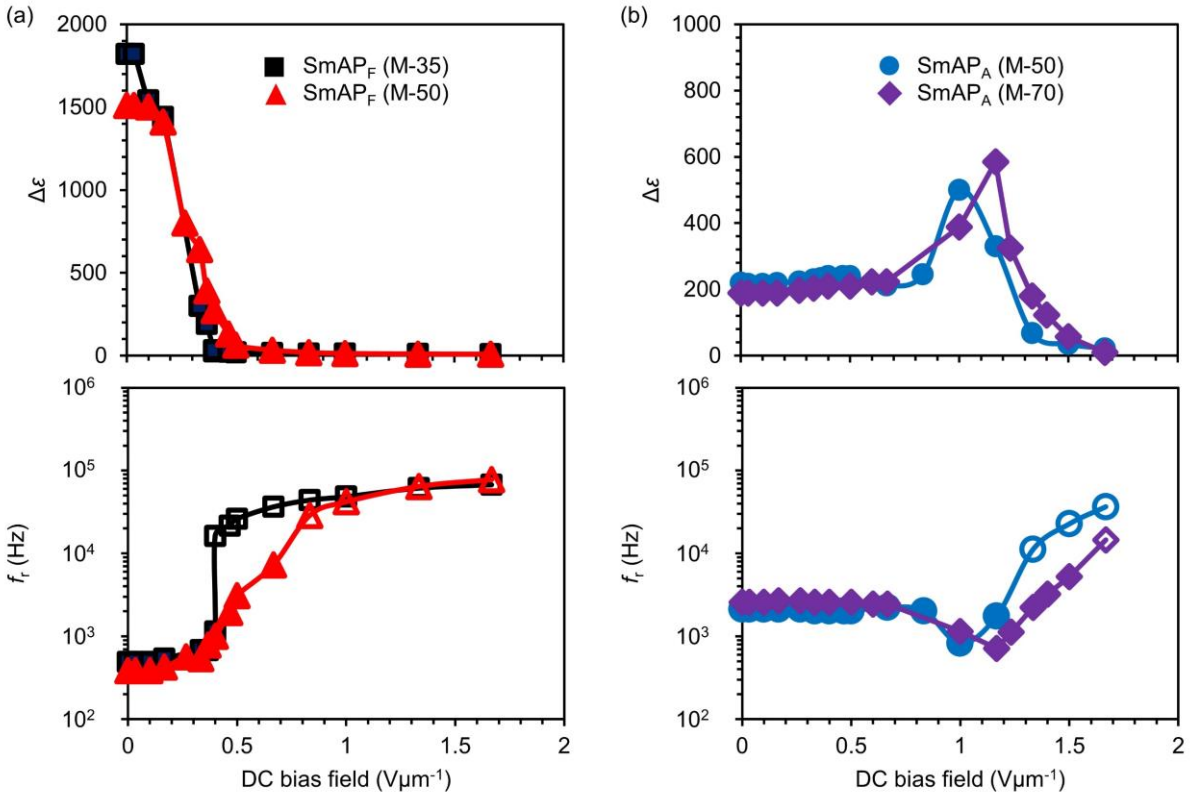

Figure 3-15. DC bias field dependence of the $\Delta\varepsilon$ and f_r in (a) the SmAP$_F$ phase of M-35 and 50, and (b) SmAP$_A$ phase of M-50 and 70, measured in a 3 μm-thick cell. Here, the f_r (open symbol) of 10^4 to 10^5 Hz collected for the non-collective modes are plotted as reference.

minimum is observed in the f_r at 1.2 Vμm^{-1}. The maximum $\Delta\varepsilon$ at 1.2 Vμm^{-1} is around 600, which is three times larger than that of the initial value, and the corresponding f_r gets closer to that of the LF mode of the SmAP$_F$ phase. Finally, the $\Delta\varepsilon$ becomes zero at around 1.6–1.7 Vμm^{-1} which is nearly equal to the E_{th} of 2 Vμm^{-1}. Two explanations for this curious behavior before the suppression are suggested. First, the SmAP$_A$ structure partly transforms to the SmAP$_F$ structure. Secondly, the LF mode characteristic of the SmAP$_A$ is enhanced just before the transformation to the SmAP$_F$ structure.

It should be noted that such an enhancement behavior is not observed in another type of antiferroelectric phase, the SmC$_A$P$_A$, which invariably shows only the HF mode even when the DC bias field up to 15 Vμm^{-1} (larger than E_{th}) is applied.

3.4. Concluding Remarks

In this chapter, three types of the ferroelectric and antiferroelectric smectic phases, SmAP$_F$, SmAP$_A$, and SmC$_A$P$_A$, each show the well-defined switching and dielectric behavior characteristics.

In the SmAP$_F$ phase, a small E_{th} less than 1 Vμm^{-1} for the ferroelectric switching is characteristic. It decreases with the cell thickness, and becomes 0.1 Vμm^{-1} in the 80 μm-thick cell. Such a small E_{th} is reasonable, considering that the ferroelectric switching of the SmAP$_F$

is essentially thresholdless because all possible polar directions around the molecular axes are energetically equivalent. A weak threshold nature may arise from interactions at cell surfaces and the boundary between the fan-shaped domains, the effect of which becomes weakened when the cell thickness increases. The present $SmAP_F$ is also found to show the distinct LF mode due to the collective fluctuation of polarization in the dielectric measurement. The LF mode appears at a low frequency of around 500 Hz and with a huge $\Delta\varepsilon$ beyond 1500. Again, the $\Delta\varepsilon$ is strongly dependent on the cell thickness. The $\Delta\varepsilon$ increases from 1500 in the 3 μm-thick cell to 10000 in the 80 μm-thick cell, and simultaneously the mode frequency decreases from 500 Hz to 200 Hz. Considering the smectic domain size increases with increasing the cell thickness, these increase and decrease are attributed to the increase of the correlation length of the LF mode.

In the antiferroelectric $SmAP_A$ phase, the E_{th} is higher than that of the $SmAP_F$, but still low at around 2 $V\mu m^{-1}$ in the 3 μm-thick cell. Similar cell thickness dependence is observed here and the E_{th} decrease to 0.6 $V\mu m^{-1}$ in the 80 μm-thick cell. In dielectric measurement, the $SmAP_A$ shows the LF mode with the $\Delta\varepsilon$ at around 200 and at frequency of 2 kHz in the 3 μm-thick cell. Similarly, as in the $SmAP_F$, the $\Delta\varepsilon$ increases to 2000, and the frequency decreases to 1 kHz with increasing the cell thickness. This LF mode is due to the collective fluctuation of net-polarization produced by the anti-phase rotation of dipoles in adjacent layers.

Another antiferroelectric phase, the SmC_AP_A, does not show the LF mode, but only the HF mode. The collective fluctuation would be limited because of the high energy barrier for rotation of dipoles as suggested from the high E_{th} at around 10 $V\mu m^{-1}$ in the 3 μm-thick cell, which is ten times larger than that of the $SmAP_F$. The HF mode with the $\Delta\varepsilon$ at around 8 and at a frequency of around 100 kHz is due to rotational relaxation of individual molecules around their short axes. Similar HF mode was observed in the paraelectric SmA, and in the $SmAP_F$ and $SmAP_A$ in which the large LF mode was suppressed under the DC bias field.

Finally, the inverse dependency of the $\Delta\varepsilon$ for the LF mode and the E_{th} on the cell thickness

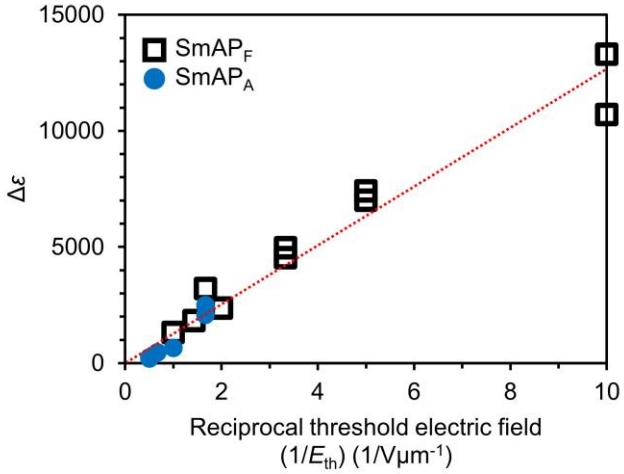

Figure 3-16. Linear correlation between the $\Delta\varepsilon$ and reciprocal E_{th} in the $SmAP_F$ phase of M-35 and 50, $SmAP_A$ phase of M-50, 60 and 70. The dotted line is guide for the eyes.

(compare Figures 3-4 and 3-12) are explained. Focusing on this dependency, the $\Delta\varepsilon$ plotted against reciprocal of the E_{th} in Figure 3-16. It can be found that all data of the $SmAP_F$ and $SmAP_A$ phases collected from the different mixtures and cells with different thicknesses fall on a linear line. The linear relationship seems reasonable, indicating that the lower the E_{th} (i.e., energy barrier between two polar states) is, the more the collective fluctuation mode of dipoles is enhanced. This will be helpful to design the high dielectric constant materials.

References

(1) Izumi T.; Naitou, Y.; Shimbo, Y.; Takanishi, Y.; Takezoe, H.; Watanabe, J. Several types of bilayer smectic liquid crystals with ferroelectric and antiferroelectric properties in binary mixture of dimeric compounds. *J. Phys. Chem. B* **2006**, *110*, 23911–23919.

(2) Guo, L.; Gorecka, E.; Pociecha, D.; Vaupotič, N.; Čepič, M.; Reddy, R. A.; Gornik, K.; Araoka, F.; Clark, N. A.; Walba, D. M., et al. Ferroelectric behavior of orthogonal smectic phase made of bent-core molecules. *Physical Review E* **2011**, *84*, 031706.

(3) Kumar, J.; Prasad, C. Ferroelectric nematic and ferrielectric smectic mesophases in an achiral bent-core azo compound. *J. Phys. Chem. B* **2018**, *122*, 2998–3007.

(4) Izumi, T.; Kang, S.; Niori, T.; Takanishi, Y.; Takezoe, H.; Watanabe, J. Smectic mesophase behavior of dimeric compounds showing antiferroelectricity, frustration and chirality. *Jpn. J. Appl. Phys.* **2006**, *45*, 1506–1514.

(5) Achard, M.F.; Bedel, J.Ph.; Marcerou, J.P.; Nguyen, H.T.; Rouillon, J.C. Switching of banana liquid crystal mesophases under field, *Eur. Phys. J. E* **2003**, *10*, 129–134.

(6) Alaasar, M.; Prehm, M.; Tamba, M.; Sebastián, N.; Eremin, A.; Tschierske, C. Development of polar order in the liquid crystal phases of a 4-cyanoresorcinol-based bent-core mesogen with fluorinated azobenzene wings, *ChemPhysChem* **2016**, *17*, 278–287.

(7) Gomola, K.; Guo, L.; Dhara, S.; Shimbo, Y.; Gorecka, E.; Pociecha, D.; Mieczkowski, J.; Takezoe, H. Syntheses and characterization of novel asymmetric bent-core mesogens exhibiting polar smectic phases, *J. Mater. Chem.*, **2009**, *19*, 4240–4247.

(8) Thisayukta, J.; Takezoe, H.; Watanabe, J. Study on helical structure of the B_4 phase formed from achiral banana-shaped molecule. *Jpn. J. Appl. Phys.* **2001**, *40*, 3277–3288.

(9) Filipič, C.; Carlsson, T.; Levstik, A.; Žekš, B.; Blinc, R.; Gouda, F.; Lagerwall, S. T.; Skarp, K. Dielectric properties near the smectic-C*–smectic-A phase transition of some ferroelectric liquid-crystalline systems with a very large spontaneous polarization. *Phys. Rev. A* **1988**, *38*, 5833–5839.

(10) Khened, S.; Prasad, S.; Shivkumar, B.; Sadashiva, B. K. Dielectric studies of Goldstone mode and soft mode in the vicinity of the A-C* transition. *J. Phys. II France* **1991**, *1*, 171–180.

(11) Fuente, M.; Dunmur, D. Dielectric Properties of Liquid Crystals. In *Handbook of liquid crystals*, 2nd ed.; Goodby, J.; Collings, P.; Kato, T.; Tschierske, C.; Gleeson, H.; Raynes, P., Eds.; Wiley-VCH Verlag GmbH & Co KGaA: Germany, 2014; pp 1−46.

(12) Hiraoka, K.; Takezoe, H.; Fukuda, A. Dielectric relaxation modes in the antiferroelectric smectic CA* phase, *Ferroelectrics* **1993**, *147*, 13–25.

(13) Hatano, J.; Hanakai, Y.; Furue, H.; Uehara, H.; Saito, S.; Murashiro, K. Phase sequence in smectic liquid crystals having fluorophenyl group in the core. *Jpn. J. Appl. Phys.* **1994**, *33*, 5498–5502.

(14) Cole, K.; Cole, R. Dispersion and absorption in dielectrics I, alternating current characteristics, *J. Chem. Phys.* **1941**, *9*, 341–351.

(15) Buivydas, M.; Gouda, F.; Lagerwall, S. T.; Stebler, B. The molecular aspect of the double absorption peak in the dielectric spectrum of the antiferroelectric liquid crystal phase. *Liq. Cryst.* **1995**, *18*, 879–886.

(16) Zennyoji, M.; Takanishi, Y.; Ishikawa, K.; Thisayukta, J.; Watanabe, J.; Takezoe, H. Electrooptic and dielectric properties in bent-shaped liquid crystals. *Jpn. J. Appl. Phys.* **2000**, *39*, 3536–3541.

(17) Marik, M.; Jana, D.; Majumder, K.; Chaudhuri, B. K. Dielectric behavior in B1 and B2 phases composed of unsymmetrical bent shaped liquid crystal molecules. *Mol. Cryst. Liq. Cryst.* **2015**, *606*, 111–125.

(18) Różański, S. Dielectric properties of liquid crystal formed by laterally fluorine-substituted banana-shaped molecules, *Phase Transitions* **2018**, *91*, 1007–1016.

CHAPTER 4

Spontaneous Polarization Characteristics in Polar Smectic Phases of Fluoro-Substituted Bent-Shaped Dimeric Molecules

4.1. Introduction

As mentioned in Chapter 1, for commercial uses of the polar phases, increasing the dielectric strength ($\Delta\varepsilon$), and the spontaneous polarization (P_s), are desired. In this aspect, a study on the characteristic dielectric properties of the $SmAP_F$ phase mentioned in Chapters 2 and 3 is interesting. The $SmAP_F$ phase exhibits the collective fluctuation mode of dipoles at around 500 Hz, which possesses a huge $\Delta\varepsilon$. The $\Delta\varepsilon$ increases with the cell thickness and reaches a value higher than 10000 in a 80 μm-thick cell, which is much higher than almost all of the reported values in the bent-shaped molecules.[1,2] The highly cooperative orientation of the bent-shaped dimeric molecule is considered to bring about the giant value of the $\Delta\varepsilon$. In Chapter 3, the electrical switching and dielectric relaxation properties have also been examined for other $SmAP_A$ and SmC_AP_A phases as well as the $SmAP_F$ phase. The P_s obtained from the electrical switching are similar, but the threshold electric field (E_{th}) differs greatly depending on the kind of smectic phases. Plotting the $\Delta\varepsilon$ against the reciprocal of the E_{th} in the $SmAP_F$ and $SmAP_A$ phases show a linearly proportional trend. This indicates that the lower the E_{th} (i.e., energy barrier between two polar states) is, the more the collective fluctuation mode of dipoles is enhanced. Thus, it is concluded that the polar liquid crystal (LC) materials with small E_{th} are the molecular design for increasing the $\Delta\varepsilon$.

On the other hand, increasing the dipole moment of the molecule is another method to increase the $\Delta\varepsilon$ as well as P_s. This is reported by attaching the polar groups.[3–6] The fluorine substitution in the bent core mesogen is a typical strategy, and a substantial increase in the P_s has been reported.[3–5] Furthermore, the fluorine substitution on LC molecules offers further interesting effects, for example, lowering the mesophase temperature region[3,5,7,8] and the viscosity of the LC phase,[5,8] which are useful for commercialization. So far, there is still few reports on the fluorine-substituted bent-shaped dimeric molecules forming the polar LC phases.

In this chapter, novel 2F-Z-C16, 2F-Y-C16 and 4F-XY-C16 fluorine-substituted on X, Y and Z positions of C16 (=16OAM5AMO16) molecules mentioned in Chapters 2 and 3 (see Figure

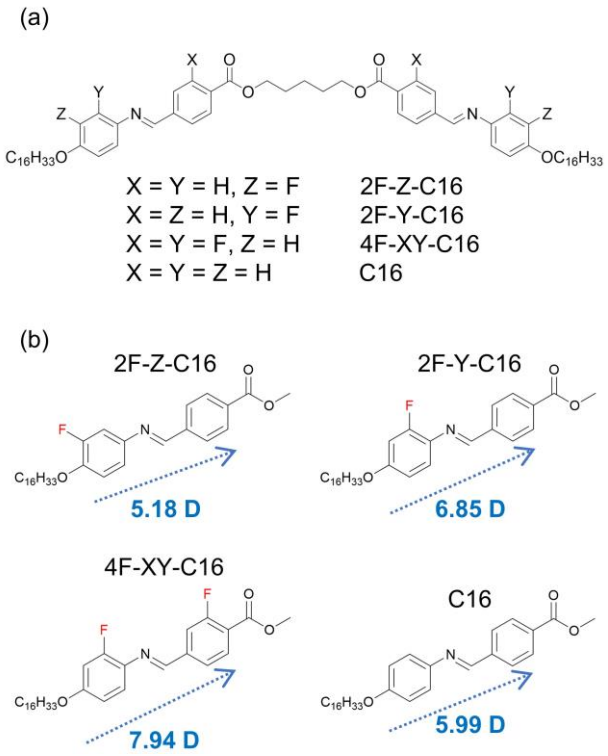

Figure 4-1. (a) Molecular structures of the fluoro-substituted bent-shaped dimeric molecules, and (b) the values of dipole moment along the long axis of one-side mesogen calculated by density functional theory. The arrows represent the direction of the dipole moment.

4-1(a)) are synthesized, and the effects of the fluorine substitution on the polar smectic structures, P_s and other properties are investigated.

4.2. Experimental Section

4.2.1. Materials

Unless otherwise noted, reagents and solvents were purchased from commercial suppliers and used without further purification.

4.2.2. Measurements

Nuclear magnetic resonance (NMR) spectroscopy measurements were carried out on a Bruker AVANCE-500 spectrometer (500 MHz for ^{1}H, 470 MHz for ^{19}F and 126 MHz for ^{13}C). Chemical shifts (δ) are expressed relative to the resonances of the residual non-deuterated solvent for ^{1}H ($CDCl_3$: $^{1}H(\delta) = 7.26$ ppm), the resonances of the residual solvent for ^{13}C ($CDCl_3$: $^{13}C(\delta) = 77.16$ ppm), the resonance of CF_3COOH as external standard for ^{19}F (CF_3COOH: $^{19}F(\delta) = -76.55$ ppm). Absolute values of the coupling constants are given in Hertz (Hz), regardless of their sign. Multiplicities are abbreviated as singlet (s), doublet (d), doublet of doublets (dd), triplet (t), multiplet (m) and broad (br). The elemental analyses (C, H, N) were carried out on a MICRO CORDER JM10 and the element analysis (O) were carried out on a vario MICRO cube. The phase transition temperatures were determined by differential scanning

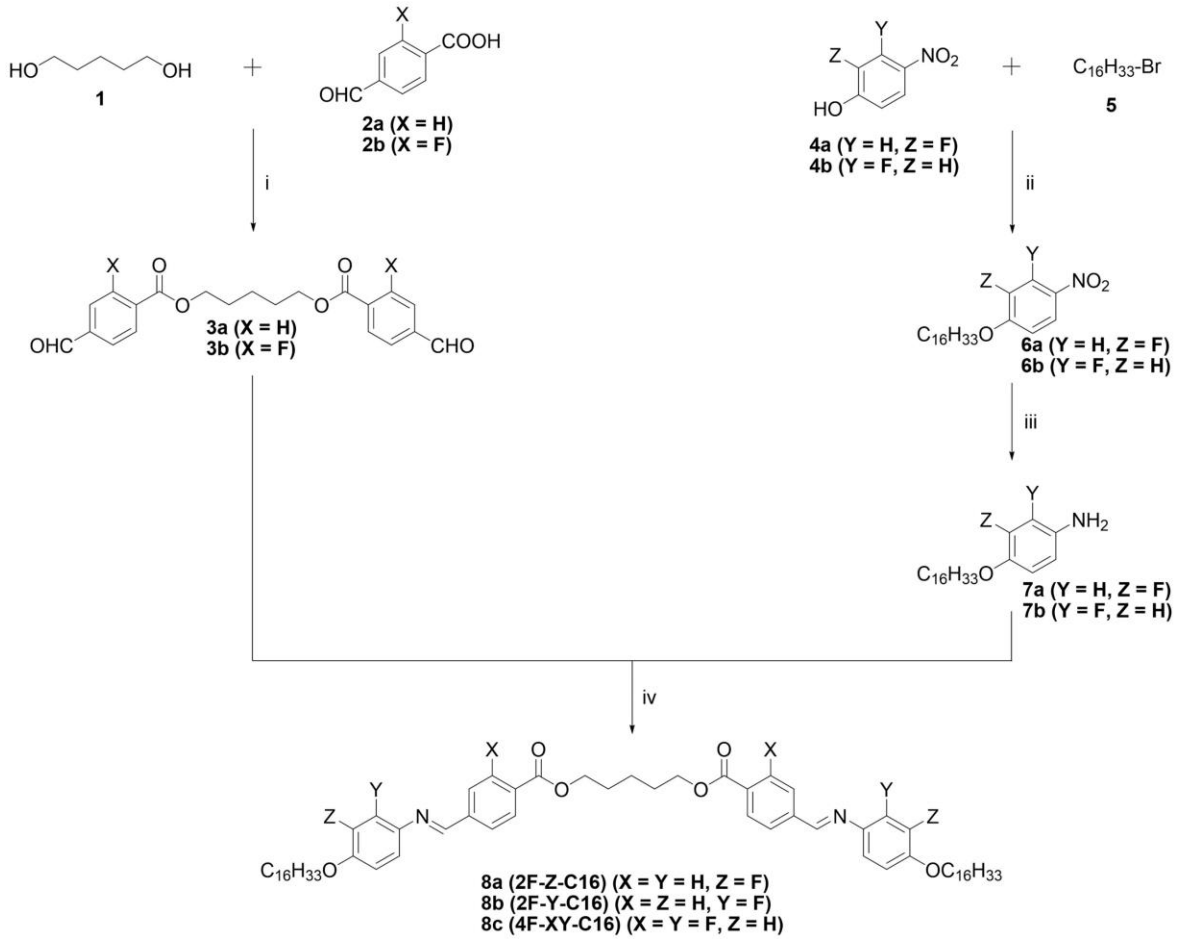

Scheme 4-1. Synthetic route for the preparation the fluorine-substituted bent-shaped dimeric molecule. Reagents and conditions: (i) *N*,*N'*-dicyclohexylcarbodiimide, ethyl acetate, 4-dimethylaminopyridine, room temperature 15 hours, (ii) potassium carbonate, acetone, reflux 12 hours, (iii) 5% Pd-C, ethanol, hydrogen, room temperature 15 hours, (iv) ethanol, reflux 4 hours.

calorimetry (DSC) (SHIMADZU DSC-60 Plus) at a rate of 5 °Cmin^{-1} under cooling run. Optical microscopic, electrooptical, dielectric and second harmonic generation (SHG) investigations were performed using glass cells coated with indium tin oxide (ITO) electrodes, which is commercially available from EHC Co., Ltd. The area of the ITO electrodes was 100 mm^2, and the cell thicknesses of the ITO electrodes were 3 μm. Texture observation and identification of the mesophases were carried out using a polarizing optical microscope (POM) (OLYMPUS BX53) equipped with a hot stage and a temperature controller (Mettler Toledo FP 82HT). X-ray diffraction (XRD) measurements were performed using a Nano-viewer (Rigaku) with Cu K_α radiation. The homeotropically aligned sample for XRD measurements was prepared as droplets on the glass substrate coated with commercially available trimethoxy(octadecyl)silane. The polarization reversal current and switching rate to the ferroelectric phase were observed by applying a triangular wave voltage and a rectangular wave voltage using a high-speed amplifier (FLC Electronics, F20A) connected to a function generator (NF Electronic Instruments,

WF1945B), respectively. SHG measurement was performed using a 10 Hz Nd:YAG laser (Minilite-II) of λ = 1064 nm as a fundamental beam, and in the *p*-in and *p*-out polarization combinations. The incidence angle of the laser to the sample cell settled in a heater block was 45 or 90 degrees. The SHG signal was detected by a photomultiplier tube (Hamamatsu model-R1924A) and the outputs from the photomultiplier tube were accumulated by a BOXCAR integrator (Stanford Research Systems). The complex dielectric constants were measured in a frequency range between 10^1 Hz and 10^7 Hz with the impedance analyzer (NF Electronic Instruments, FRA51615) and with the electric voltage of 1 V_{pp}. Before the dielectric relaxation measurements, the smectic domain size was increased by the application of the AC electric field of 10 $V_{pp}\mu m^{-1}$ to 33 $V_{pp}\mu m^{-1}$ with frequencies of 10–1000 Hz in 300 log steps.

4.2.3. Synthesis

The bent-shaped dimeric molecule, C16 was synthesized following methods reported in a previous report.[9] Three homologues fluorine-substituted bent-shaped dimeric molecule, 2F-Z-C16, 2F-Y-C16 and 4F-XY-C16 were newly synthesized as follows (see Scheme 4-1).

4.2.3.1. Synthesis of 3a-3b

In a flask equipped with a magnetic stirrer and a nitrogen inlet were placed 1,5-pentanediol (**1**) (4.16 g, 39.94 mmol), 4-formylbenzoic acid (**2a**) (12.00 g, 79.93 mmol), *N*,*N*′-dicyclohexylcarbodiimide (18.97 g, 91.94 mmol), and ethyl acetate (94.00 g). 4-dimethylaminopyridine (11.23 g, 91.92 mmol) was then added to the solution at room temperature. The solution was stirred at room temperature for 15 hours. After filtration to remove precipitated materials, the filtrate was purified by chromatography on silica gel using chloroform eluent and then recrystallized from ethanol/water (1/1) to give **3a** (4.60 g, 31 %) as a white solid. **3b** was similarly prepared in 26 % as a white solid.

For **3a**, ^{1}H NMR (500 MHz, $CDCl_3$, 25 °C): δ (ppm) 10.10 (s, 2H, C*H*O), 8.19 (d, J = 8.3 Hz, 4H, Ar-*H*), 7.94 (d, J = 8.4 Hz, 4H, Ar-*H*), 4.41 (t, J = 6.5 Hz, 4H, COOCH_2), 1.93-1.87 (m, 4H, $COOCH_2CH_2$), 1.76-1.61 (m, 2H, $COOCH_2CH_2CH_2$). ^{13}C NMR (125 MHz, $CDCl_3$, 25 °C): δ (ppm) 191.60, 165.56, 139.15, 135.25, 130.14, 129.51, 65.26, 28.30, 22.58.

For **3b**, ^{1}H NMR (500 MHz, $CDCl_3$, 25 °C): δ (ppm) 10.05 (s, 2H, C*H*O), 8.09 (t, J = 7.3 Hz, 2H, Ar-*H*), 7.72 (d, J = 7.9 Hz, 2H, Ar-*H*), 7.62 (d, J = 10.1 Hz, 2H, Ar-*H*), 4.41 (t, J = 6.4 Hz, 4H, COOCH_2), 1.91-1.85 (m, 4H, $COOCH_2CH_2$), 1.68-1.62 (m, 2H, $COOCH_2CH_2CH_2$). ^{19}F NMR (470 MHz, $CDCl_3$, 25 °C): δ (ppm) –107.65 (t, J = 8.2 Hz, 2F, Ar-*F*). ^{13}C NMR (125 MHz, $CDCl_3$, 25 °C): δ (ppm) 190.14, 163.65, 163.62, 163.02, 160.93, 140.78, 140.72, 132.97, 124.96, 124.93, 124.04, 123.95, 117.23, 117.05, 65.62, 28.14, 22.47.

4.2.3.2. Synthesis of 6a-6b

In a flask equipped with a magnetic stirrer, a reflux condenser and a nitrogen inlet were placed 2-fluoro-4-nitrophenol (**4a**) (5.00 g, 31.83 mmol), 1-bromohexadecane (**5**) (10.69 g,

35.01 mmol), potassium carbonate (6.60 g, 47.76 mmol), and acetone (33.00 g). The solution was stirred and heated under reflux for 12 hours. The solution was concentrated by using a rotary evaporator and was diluted with water and ethyl acetate. The organic layer was then extracted with water. The solvent was evaporated and residue was purified by chromatography on silica gel using ethyl acetate/hexane (1/49) eluent to give **6a** (4.60 g, 38 %) as a white solid. **6b** was similarly prepared in 33 % as a white solid.

For **6a**, ^{1}H NMR (500 MHz, $CDCl_3$, 25 °C): δ (ppm) 8.06-8.03 (m, 1H, Ar-*H*), 7.98 (dd, J = 10.7, 2.7 Hz, 1H, Ar-*H*), 7.01 (t, J = 8.6 Hz, 1H, Ar-*H*), 4.13 (t, J = 6.6 Hz, 2H, OCH_2), 1.89-1.83 (m, 2H, OCH_2CH_2), 1.51-1.45 (m, 2H, $OCH_2CH_2CH_2$), 1.37-1.26 (m, 24H, $(CH_2)_{12}CH_3$), 0.88 (t, J = 6.9 Hz, 3H, CH_2CH_3). ^{19}F NMR (470 MHz, $CDCl_3$, 25 °C): δ (ppm) –130.50 (t, J = 9.3 Hz, 1F, Ar-*F*). ^{13}C NMR (125 MHz, $CDCl_3$, 25 °C): δ (ppm) 153.11, 153.03, 152.27, 150.27, 140.60, 140.55, 120.91, 120.89, 112.82, 112.80, 112.38, 112.20, 69.91, 31.93, 29.69, 29.67, 29.64, 29.56, 29.50, 29.37, 29.27, 28.87, 25.80, 22.70, 14.12.

For **6b**, ^{1}H NMR (500 MHz, $CDCl_3$, 25 °C): δ (ppm) 8.08 (t, J = 8.9 Hz, 1H, Ar-*H*), 6.75-6.69 (m, 2H, Ar-*H*), 4.02 (t, J = 6.5 Hz, 2H, OCH_2), 1.84-1.78 (m, 2H, OCH_2CH_2), 1.48-1.42 (m, 2H, $OCH_2CH_2CH_2$), 1.36-1.26 (m, 24H, $(CH_2)_{12}CH_3$), 0.88 (t, J = 6.9 Hz, 3H, CH_2CH_3). ^{19}F NMR (470 MHz, $CDCl_3$, 25 °C): δ (ppm) –112.96 (t, J = 10.7 Hz, 1F, Ar-*F*). ^{13}C NMR (125 MHz, $CDCl_3$, 25 °C): δ (ppm) 165.00, 158.60, 156.50, 130.51, 130.45, 127.88, 128.86, 110.76, 110.74, 103.58, 103.39, 69.41, 31.93, 29.70, 29.67, 29.64, 29.56, 29.51, 29.37, 29.26, 28.81, 25.84, 22.70, 14.12.

4.2.3.3. Synthesis of 7a-7b

In a flask equipped with a magnetic stirrer and a hydrogen inlet were placed **6a** (4.50 g, 11.79 mmol), ethanol (34.04 g), and 5% palladium-activated carbon (1.51 g, 0.71 mmol/Pd). The flask was degassed and purged with hydrogen several times and then stirred at room temperature for 15 hours. The solution was filtered and concentrated using a rotary evaporator. The product was dried at 50 °C *in vacuo* to give **7a** (3.99 g, 96 %) as a red solid. **7b** was similarly prepared in 97 % as a red solid.

For **7a**, ^{1}H NMR (500 MHz, $CDCl_3$, 25 °C): δ (ppm) 6.79 (t, J = 8.9 Hz, 1H, Ar-*H*), 6.45 (dd, J = 12.7, 2.7 Hz, 1H, Ar-*H*), 6.37-6.34 (m, 1H, Ar-*H*), 3.93 (t, J = 6.7 Hz, 2H, OCH_2), 3.48 (br, 2H, NH_2), 1.77-1.72 (m, 2H, OCH_2CH_2), 1.46-1.40 (m, 2H, $OCH_2CH_2CH_2$), 1.34-1.23 (m, 24H, $(CH_2)_{12}CH_3$), 0.88 (t, J = 6.9 Hz, 3H, CH_2CH_3). ^{19}F NMR (470 MHz, $CDCl_3$, 25 °C): δ (ppm) –132.68 (t, J = 10.8 Hz, 1F, Ar-*F*). ^{13}C NMR (125 MHz, $CDCl_3$, 25 °C): δ (ppm) 154.79, 152.84, 141.13, 141.06, 139.62, 139.53, 117.89, 117.87, 110.37, 110.34, 104.25, 104.08, 71.06, 31.94, 29.71, 29.67, 29.61, 29.59, 29.47, 29.41, 29.38, 25.93, 22.71, 14.13.

For **7b**, ^{1}H NMR (500 MHz, $CDCl_3$, 25 °C): δ (ppm) 6.72-6.68 (m, 1H, Ar-*H*), 6.63-6.60 (m, 1H, Ar-*H*), 6.54-6.52 (m, 1H, Ar-*H*), 3.86 (t, J = 6.5 Hz, 2H, OCH_2), 3.41 (br, 2H, NH_2), 1.75-1.71 (m, 2H, OCH_2CH_2), 1.43-1.41 (m, 2H, $OCH_2CH_2CH_2$), 1.31-1.27 (m, 24H, $(CH_2)_{12}CH_3$), 0.89 (t, J = 6.7 Hz, 3H, CH_2CH_3). ^{19}F NMR (470 MHz, $CDCl_3$, 25 °C): δ (ppm) –132.09 (t, J =

11.2 Hz, 1F, Ar-*F*). ^{13}C NMR (125 MHz, $CDCl_3$, 25 °C): δ (ppm) 152.98, 152.43, 152.36, 151.08, 127.57, 127.47, 117.65, 117.61, 110.58, 110.55, 103.09, 102.91, 68.82, 31.94, 29.71, 29.68, 29.61, 29.59, 29.41, 29.38, 29.29, 26.03, 22.71, 14.13.

4.2.3.4. Synthesis of 8a-8c

In a flask equipped with a magnetic stirrer, a reflux condenser and a nitrogen inlet were placed **3a** (0.67 g, 1.82 mmol), **7a** (1.59 g, 4.52 mmol), and ethanol (35.43 g). The solution was stirred and heated under reflux for 4 hours. The solution was cooled and then precipitates were filtered. The residue was purified by chromatography on activated alumina using chloroform eluent, and recrystallized from chloroform/ethanol (1/1) to give 2F-Z-C16 (**8a**) (1.74 g, 85 %) as a yellow solid. 2F-Y-C16 (**8b**) and 4F-XY-C16 (**8c**) were similarly prepared in 90 % and 84 % as yellow solid, respectively.

For **8a**, ^{1}H NMR (500 MHz, $CDCl_3$, 25 °C): δ (ppm) 8.48 (s, 2H, N=C*H*), 8.11 (d, J = 8.3 Hz, 4H, Ar-*H*), 7.92 (d, J = 8.4 Hz, 4H, Ar-*H*), 7.07 (dd, J = 12.1, 2.4 Hz, 2H, Ar-*H*), 7.02-6.93 (m, 4H, Ar-*H*), 4.40 (t, J = 6.5 Hz, 4H, COOCH_2), 4.04 (t, J = 6.7 Hz, 4H, OCH_2), 1.92-1.87 (m, 4H, $COOCH_2CH_2$), 1.86-1.80 (m, 4H, OCH_2CH_2), 1.69-1.64 (m, 2H, $COOCH_2CH_2CH_2$), 1.51-1.45 (m, 4H, $OCH_2CH_2CH_2$), 1.37-1.26 (m, 48H, $OCH_2CH_2CH_2(CH_2)_{12}$), 0.88 (t, J = 6.9 Hz, 6H, CH_2CH_3). ^{19}F NMR (470 MHz, $CDCl_3$, 25 °C): δ (ppm) –132.87 (t, J = 10.3 Hz, 2F, Ar-*F*). ^{13}C NMR (125 MHz, $CDCl_3$, 25 °C): δ (ppm) 166.09, 157.66, 153.82, 151.85, 146.31, 146.22, 144.31, 144.26, 139.94, 132.43, 129.93, 128.53, 117.51, 117.49, 114.93, 114.91, 109.10, 108.94, 69.73, 64.93, 31.94, 29.71, 29.68, 29.62, 29.58, 29.40, 29.38, 29.26, 28.34, 25.94, 22.71, 22.63, 14.13. Elemental analysis: calculated for $C_{65}H_{92}F_2N_2O_6$, C 75.40, H 8.96, N 2.71, O 9.27; found, C 75.34, H 9.23, N 2.75, O 9.71%.

For **8b**, ^{1}H NMR (500 MHz, $CDCl_3$, 25 °C): δ (ppm) 8.61 (s, 2H, N=C*H*), 8.10 (d, J = 8.3 Hz, 4H, Ar-*H*), 7.94 (d, J = 8.3 Hz, 4H, Ar-*H*), 7.19-7.15 (m, 2H, Ar-*H*), 6.71-6.69 (m, 4H, Ar-*H*), 4.39 (t, J = 6.4 Hz, 4H, COOCH_2), 3.95 (t, J = 6.5 Hz, 4H, OCH_2), 1.92-1.87 (m, 4H, $COOCH_2CH_2$), 1.82-1.76 (m, 4H, OCH_2CH_2), 1.67-1.64 (m, 2H, $COOCH_2CH_2CH_2$), 1.49-1.43 (m, 4H, $OCH_2CH_2CH_2$), 1.36-1.26 (m, 48H, $OCH_2CH_2CH_2(CH_2)_{12}$), 0.88 (t, J = 6.9 Hz, 6H, CH_2CH_3). ^{19}F NMR (470 MHz, $CDCl_3$, 25 °C): δ (ppm) –122.74 (t, J = 10.9 Hz, 2F, Ar-*F*). ^{13}C NMR (125 MHz, $CDCl_3$, 25 °C): δ (ppm) 166.13, 159.02, 158.99, 158.90, 158.81, 157.47, 155.47, 140.24, 132.38, 131.73, 131.64, 129.88, 128.50, 122.55, 122.53, 110.63, 110.60, 103.05, 102.86, 68.61, 64.91, 31.94, 29.71, 29.68, 29.62, 29.58, 29.40, 29.38, 29.16, 28.34, 26.01, 22.71, 22.64, 14.13. Elemental analysis: calculated for $C_{65}H_{92}F_2N_2O_6$, C 75.40, H 8.96, N 2.71, O 9.27; found, C 75.21, H 8.68, N 2.78, O 9.57%.

For **8c**, ^{1}H NMR (500 MHz, $CDCl_3$, 25 °C): δ (ppm) 8.57 (s, 2H, N=C*H*), 8.00 (t, J = 7.5 Hz, 2H, Ar-*H*), 7.68 (t, J = 9.6 Hz, 4H, Ar-*H*), 7.18 (t, J = 9.1 Hz, 2H, Ar-*H*), 6.70-6.68 (m, 4H, Ar-*H*), 4.40 (t, J = 6.3 Hz, 4H, COOCH_2), 3.95 (t, J = 6.5 Hz, 4H, OCH_2), 1.91-1.85 (m, 4H, $COOCH_2CH_2$), 1.82-1.76 (m, 4H, OCH_2CH_2), 1.70-1.63 (m, 2H, $COOCH_2CH_2CH_2$), 1.47-1.43 (m, 4H, $OCH_2CH_2CH_2$), 1.36-1.26 (m, 48H, $OCH_2CH_2CH_2(CH_2)_{12}$), 0.88 (t, J = 6.8 Hz, 6H,

CH_2CH_3). ^{19}F NMR (470 MHz, $CDCl_3$, 25 °C): δ (ppm) –108.82 (t, J = 8.9 Hz, 2F, Ar-*F*), –122.13 (t, J = 10.9 Hz, 2F, Ar-F). ^{13}C NMR (125 MHz, $CDCl_3$, 25 °C): δ (ppm) 164.15, 164.11, 163.15, 161.07, 159.23, 159.15, 157.58, 157.32, 155.58, 142.39, 142.33, 132.47, 131.08, 131.00, 124.08, 124.05, 122.90, 122.88, 120.74, 120.66, 116.21, 116.02, 110.70, 110.68, 103.08, 102.89, 68.63, 65.23, 31.94, 29.71, 29.67, 29.61, 29.58, 29.38, 29.13, 28.20, 26.00, 22.70, 14.13. Elemental analysis: calculated for $C_{65}H_{90}F_4N_2O_6$, C 72.87, H 8.47, N 2.61, O 8.96; found, C 72.71, H 8.62, N 2.64, O 9.69%.

4.2.4. Computational calculations

The molecular parameter such as the dipole moment was calculated by density functional theory. It was carried out by Gaussian 09 software, selecting DFT/B3LYP methods using 6-31G (d,p) basis.[10,11] The geometries were optimized by minimizing the energies with respect to all geometrical parameters without imposing any molecular symmetry constraints.

4.3. Results and Discussion

4.3.1. Molecular parameters obtained by density functional theory

The calculated dipole moments along the long axis of the one-sided mesogenic core of the dimeric molecules, are given in Figure 4-1(b). Those are 5.18, 6.86, 7.94 and 5.99 D, respectively, for 2F-Z-C16, 2F-Y-C16, 4F-XY-C16 and C16. Detail dipole moment components (μ_x, μ_y, μ_z), and the resultant dipole moment (μ) are shown in Table 4-1. In comparison with C16, fluorine substitution on the X and Y positions led to increase in the dipole moment, while it decreased when the substitution was on the Z position. This observation seems to be reasonable when compared with the previous reports.[3,4]

The molecular length, calculated under the assumption of taking an all-trans conformation, is 64.2 Å for C16.[9] Calculated molecular length is not essentially varied by the fluorine substitution, although the actual length in LC state may be shorter than this.

Table 4-1. Dipole moment components (μ_x, μ_y, μ_z), and the resultant dipole moment (μ) by DFT calculation.

	Dipole moment (D)			
	μ_x	μ_y	μ_z	μ[a]
2F-Z-C16	4.74	2.04	0.40	5.18
2F-Y-C16	6.65	1.63	0.16	6.85
4F-XY-C16	7.94	0.24	-0.12	7.94
C16	5.80	-0.48	-1.43	5.99

[a] $\mu = \mu_{resultant} = (\mu_x^2 + \mu_y^2 + \mu_z^2)^{1/2}$

4.3.2. Transition behaviors

The DSC thermograms are shown in Figure 4-2 and their thermodynamic DSC data are listed in Table 4-2. All the materials form the monotropic smectic phases: 2F-Z-C16 forms the $SmAP_F$ phase, while 2F-Y-C16 and 4F-XY-C16 form SmC_AP_A phase. The SmC_AP_A phase for 4F-XY-C16 and the $SmAP_F$ phase for 2F-Z-C16 transforms to crystal (Cr) on cooling. In contrast, the SmC_AP_A phases for C16 and 2F-Y-C16 transform to B_4 phase[12], and only the B_4 phase of 2F-Y-C16 is followed by Cr phase on further cooling.

One significant effect due to the fluorine substitution is observed on the transition temperatures. Although the temperature span of smectic phase is almost unchanged, the smectic region shifts by 10–30 °C to the low temperature in a comparison of C16. The effect is more remarkable in the fluorine substitution to position Y rather than position Z, and by the increase in number of the fluorine substitutions. This is due to the weakening of the intermolecular force caused by the fluorine substitution.[3–5,8]

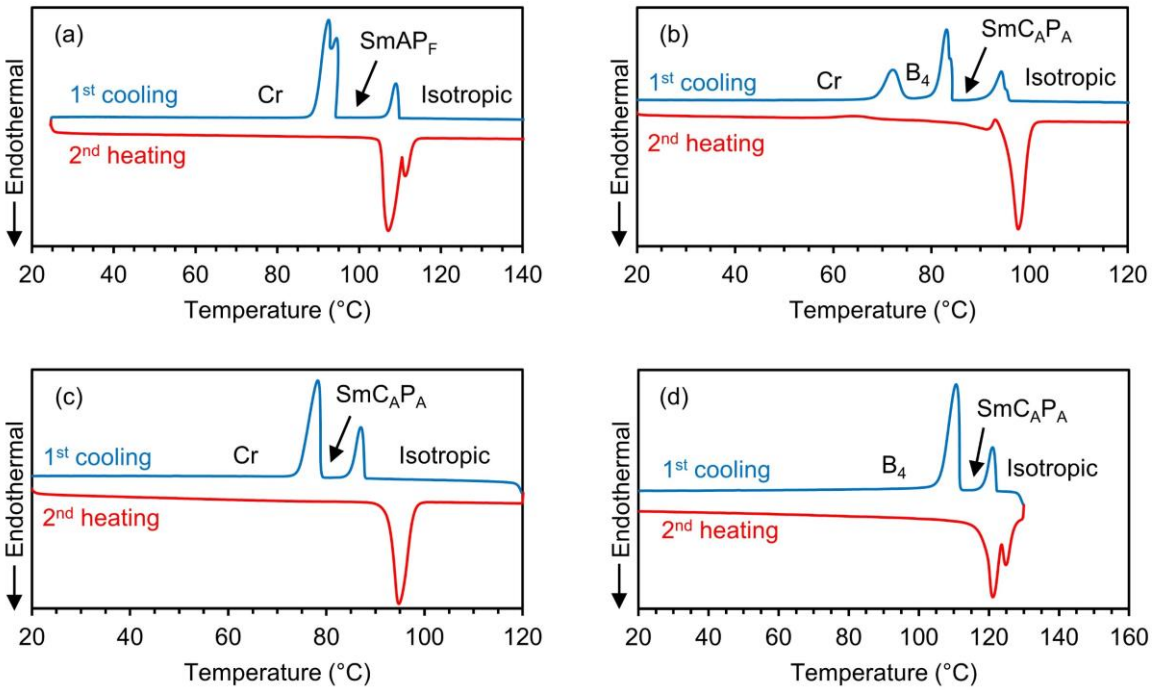

Figure 4-2. DSC thermogram for (a) 2F-Z-C16, (b) 2F-Y-C16, (c) 4F-XY-C16 and (d) C16. Scanning rate is 5 °Cmin^{-1}.

Table 4-2. Transition temperatures (°C) and associated enthalpy changes ($kJmol^{-1}$) (*in italics*) of 2F-Z-C16, 2F-Y-C16, 4F-XY-C16 and C16 collected from cooling DSC thermograms.

	Cr		B_4	SmC_AP_A		$SmAP_F$	Iso
2F-Z-C16	●	-	94.6 (*107.9*)	-	●	109.0 (*20.3*)	●
2F-Y-C16	●	73.0 (*32.7*)	●	83.1 (*46.2*)	●	-	94.2 (*23.4*)	●
4F-XY-C16	●	-		78.3 (*62.3*)	●	-	87.0 (*23.3*)	●
C16	-	-	●	109.2 (*77.6*)	-	-	120.0 (*21.9*)	●

4.3.3. Structure and properties of polar phases

4.3.3.1. $SmAP_F$ phase of 2F-Z-C16

Figure 4-3(a) shows the oriented XRD pattern taken for the homeotropically aligned $SmAP_F$ phase of 2F-Z-C16 with a beam parallel to the layer. The layer reflections with the spacing of 59.0 Å appear on the meridian, and the outer broad reflections with a spacing of 4.6 Å are observed at the portions lying above and below the equator.[13] This indicates that the molecules with a bent conformation lie perpendicularly to the layer. The spacing data is shown as Table 4-3.

Figure 4-4(a) shows the polarization reversal current observed in the $SmAP_F$ phase. By applying a triangular voltage wave, the $SmAP_F$ shows one current peak on a half cycle as shown in Figure 4-4(a), which identifies the ferroelectricity. The reversal polarization estimated as the integral of the current peak in a half cycle is 0.56 μCcm^{-2}. As found in Figures 4-4(b)–(d), the $SmAP_F$ shows well defined fan-shaped textures, which is not essentially changed during switching. No change of birefringence color is also characteristic, indicating that the polar direction (or bent direction) of molecule in the homogeneously aligned smectic layers are perpendicular to the cell surface invariably on field-OFF and field-ON. In addition, no rotation of extinction positions indicates the perpendicular alignment of molecules to the layer. Thus, smectic phase is identified as $SmAP_F$ although the observed layer spacing of 59.0 Å is somewhat smaller than the calculated length, 64.2 Å.

The ferroelectricity is also proved from SHG activity. Here, the same glass cell as the optoelectric one was used and the SHG was observed by the incidence angle of 45 degrees to the cell surface. The SHG intensities are plotted against temperature in Figure 4-5(a). On cooling from the isotropic phase, SHG appears on entering to the $SmAP_F$ phase and is invariably detected through $SmAP_F$ region. The SHG activity is remained on the crystallization, which suggests the Cr phase has also no inversion center.

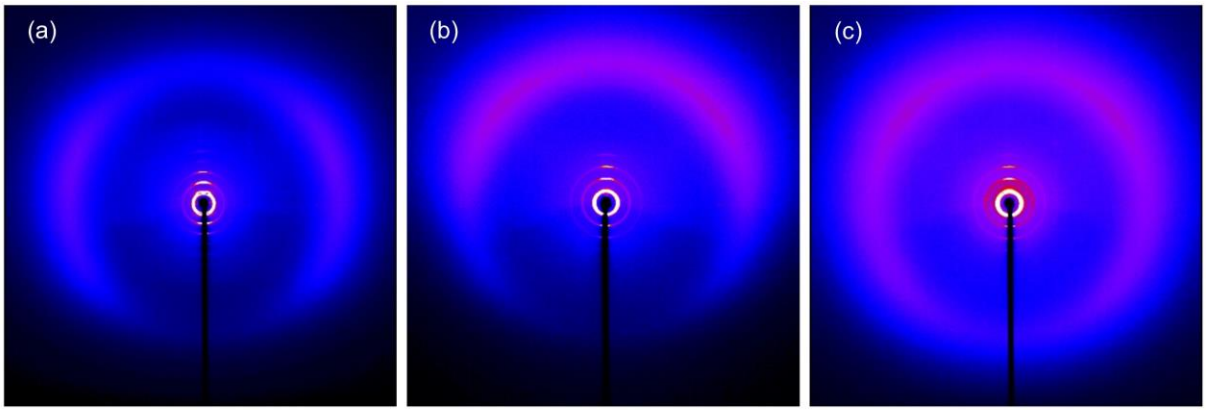

Figure 4-3. XRD pattern observed for homeotropically aligned (a) $SmAP_F$ of 2F-Z-C16, (b) SmC_AP_A of 2F-Y-C16 and (c) SmC_AP_A of 4F-XY-C16, with irradiation of X-ray beam parallel to smectic layer.

Table 4-3. Spacing elucidated from (001) reflection for smectic, B_4 and Cr phases of 2F-Z-C16, 2F-Y-C16, 4F-XY-C16 and C16.

	Spacing (Å)			
	Cr	**B_4**	**SmC_AP_A**	**$SmAP_F$**
2F-Z-C16	59.4	-	-	59.0
2F-Y-C16	57.2	58.5	51.3	-
4F-XY-C16	50.9	-	50.8	-
C16	-	63.4	56.9	-

The SHG intensity of $SmAP_F$ depends on the irradiation angle to the cell surface. For example, on field-ON, no significant SHG is detected by the irradiation with an angle of 90 degrees to the cell as shown in Figure 4-5(b). This is reasonable because polar bent directions are oriented perpendicularly to the cell's surface. No SHG is also maintained even on field-OFF, meaning the maintenance of the perpendicular orientation of bent axes which corresponds to that speculated from the optical microscopic observation. Such an orientation behavior is compared with that of the $SmAP_F$ formed from the mixtures of C4 and C16 in a previous paper.[14] In the homogeneously aligned $SmAP_F$ phases of mixtures, the polar bent axes standing up to the cell on field-ON tends to lie parallel to the cell surface on field-OFF.

The different orientation behavior of polar axes between the fluorine-substituted molecules and ordinary molecules is due to the difference in the anchoring effect to the ITO coated cell. The contact between the fluorine-substituted mesogens and the coated ITO is suggested to be unfavorable, and even on field OFF, the polar direction stands up or down to the cell surface to reduce the contact. This anchoring effect is another significant effect of the fluorine substitution.

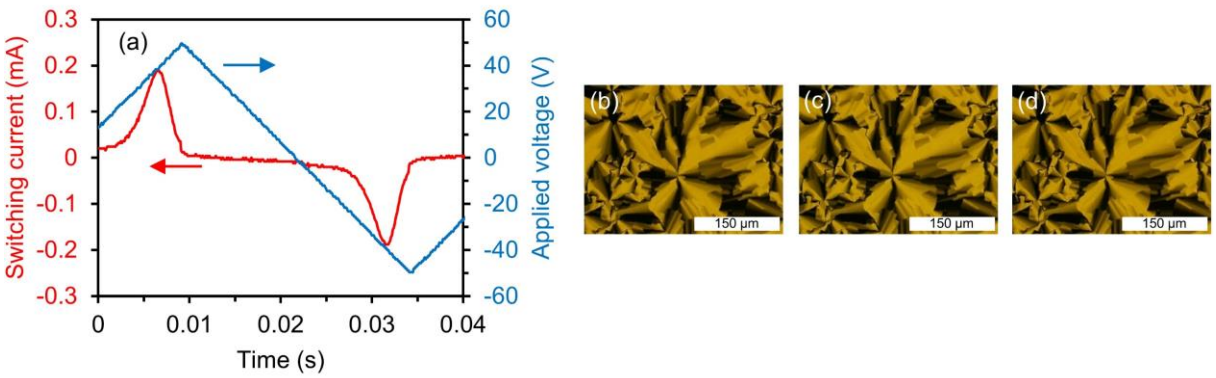

Figure 4-4. (a) Polarization reversal current for the $SmAP_F$ phase of 2F-Z-C16 by applying a triangle wave field (100 V_{pp}, 20 Hz) to a 3 μm-thick cell. POM textures at (b) -50 V, (c) 0 V and (d) 50 V, measured in a 3 μm-thick cell.

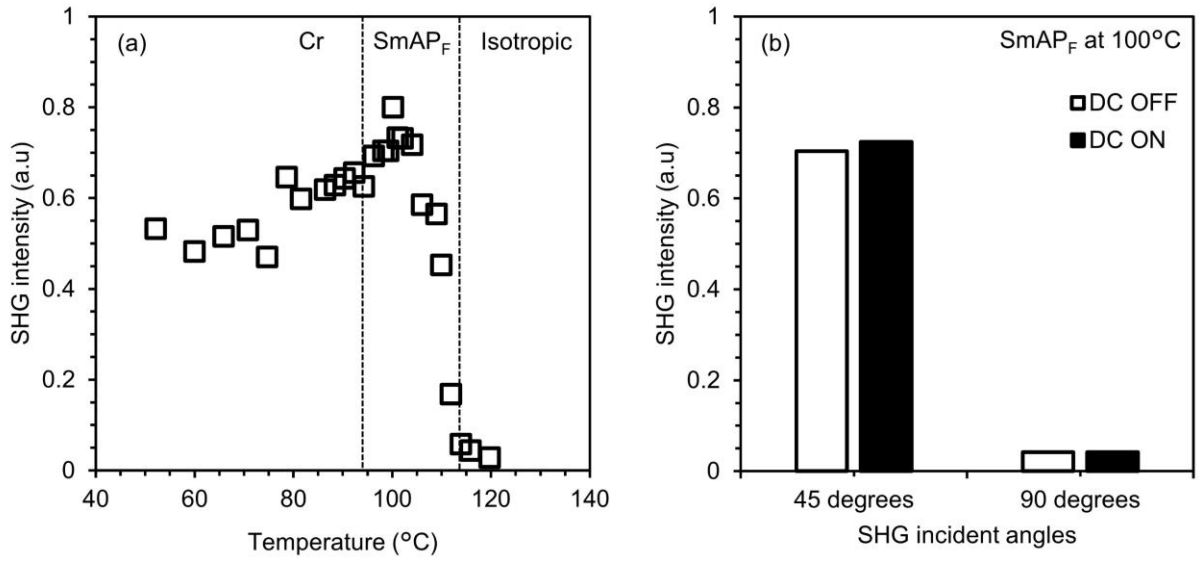

Figure 4-5. (a) Temperature dependence of SHG intensity observed in the $SmAP_F$ phase of 2F-Z-C16 with incident angle of 45 degree and without external electric field. (b) Relative SHG intensities observed with the incident angles of 45 and 90 degrees on field-OFF and field-ON.

4.3.3.2. SmC_AP_A phase of 2F-Y-C16 and 4F-XY-C16

Figures 4-3(b) and (c) show XRD pattern of homeotropically aligned SmC_AP_A for 2F-Y-C16 and 4F-XY-C16. The spacing data is shown as Table 4-3. The elucidated layer spacings of both phases are around 51 Å, which are fairly smaller than the molecular length. Thus, SmC structure with the average molecular axes tilted to the layer normal is likely. From a simple comparison of the layer spacing and molecular length, the tilt angles are elucidated around 37°.

The switching behavior of SmC_AP_A of 4F-XY-C16 is shown in Figure 4-6(a). Similar behavior is observed for 2F-Y-C16 (refer to Figure 4-7(a)). By applying the triangular wave voltage, two switching current peaks on a half cycle are observed, which indicates the

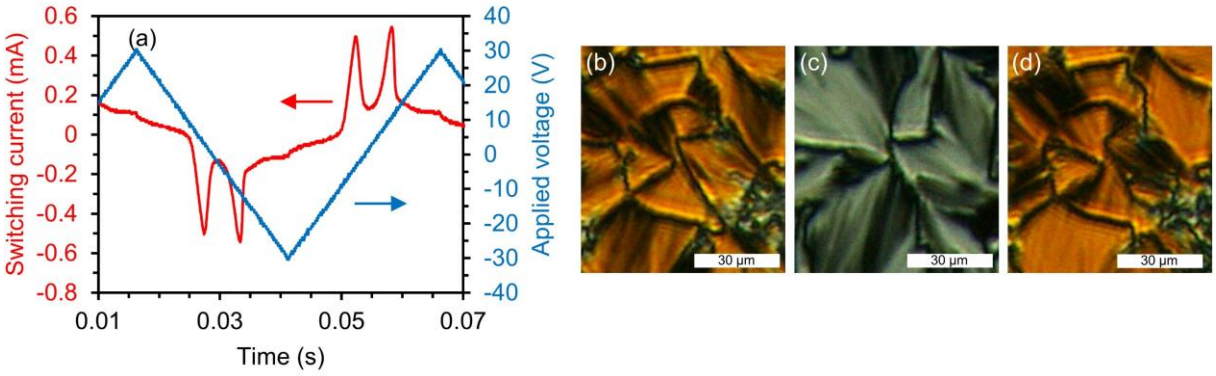

Figure 4-6. (a) Polarization reversal current of 4F-XY-C16 for the SmC_AP_A phase by applying a triangle wave field (60 V_{pp}, 20 Hz), measured in a 3 μm-thick cell. POM textures at (b) -30 V, (c) 0 V and (d) 30 V, measured in a 3 μm-thick cell.

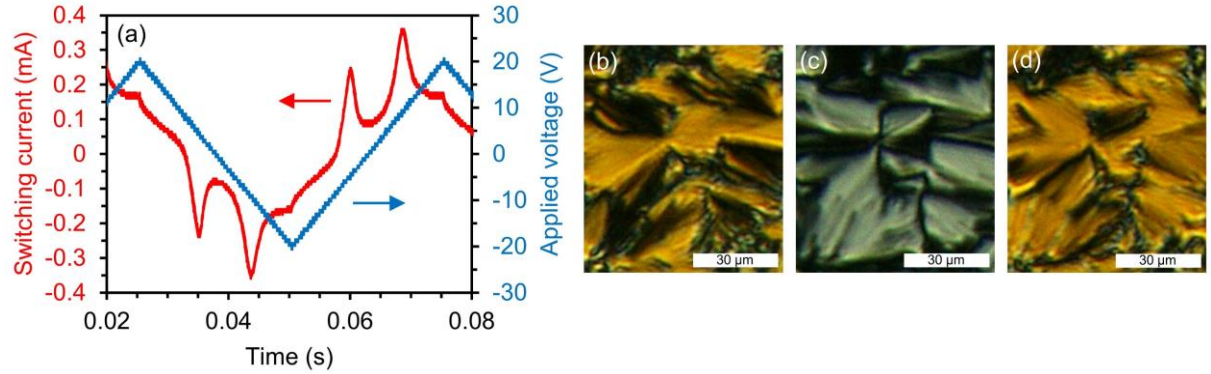

Figure 4-7. (a) Polarization reversal current of 2F-Y-C16 for the SmC_AP_A phase by applying a triangle wave field (40 V_{pp}, 20 Hz), measured in a 3 μm-thick cell. POM textures at (b) -20 V, (c) 0 V and (d) 20 V, measured in a 3 μm-thick cell.

antiferroelectricity. The reversal polarization estimated as the integral of two switching current peaks is about 1.64 μCcm^{-2} for 2F-Y-C16 and 2.42 μCcm^{-2} for 4F-XY-C16. The antiferroelectric switching is also clarified from the rotation of the extinction direction in the optical microscopic observation (see Figures 4-6(b)–(d) and 4-7(b)–(d))). The rotation angle between two ferro-states is roughly 70°, indicating the tilt angle of 35°. These tilt angles correspond well to the tilt angles of 37° obtained from a comparison of the molecular length and layer spacing.

4.3.3.3. Relationship between the molecular dipole moment and reversal polarization

In Figure 4-8, the values of reversal polarization are plotted against the dipole moments of one side mesogen. Somewhat linear relationship can be observed, showing a reasonable trend that a higher dipole moment value results a more enhanced P_s value. The expected P_s can be calculated as[15],

$$P_s = N\mu \qquad (4-1)$$

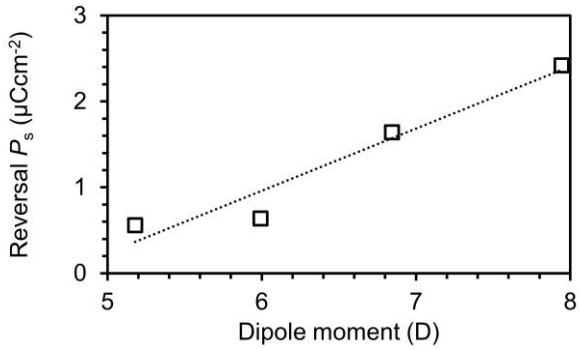

Figure 4-8. Linear correlation between the reversal polarization and dipole moment of one side mesogen. The dotted line is guide for the eyes.

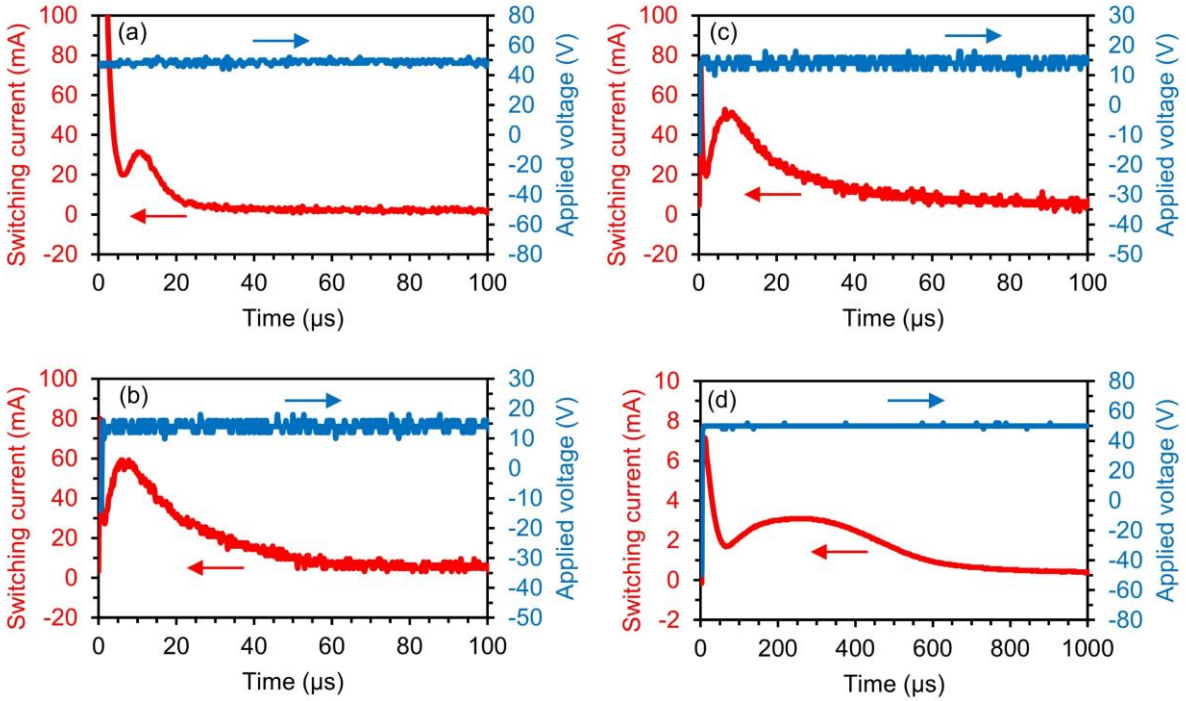

Figure 4-9. Polarization reversal current responses observed (a) for the $SmAP_F$ phase of 2F-Z-C16 by applying a square-wave field (100 V_{pp}, 20 Hz), (b) for the SmC_AP_A phase of 2F-Y-C16, (c) for the SmC_AP_A phase of 4F-XY-C16 by applying a square-wave field (30 V_{pp}, 20 Hz) and (d) for the SmC_AP_A phase of C16 by applying a square-wave field (100 V_{pp}, 20 Hz), measured in a 3 μm-thick cell.

the angle of two mesogens in the bent shape is roughly 120°, dipole moment of molecules is nearly half to that of the one-side mesogen (refer to Figure 4-1). Under the assumption that the density of smectic phase may be around 1.1 gcm^{-3}, expected P_s is 1.64 μCcm^{-2} for 4F-XY-C16. This is interestingly compared with the observed reversal polarization which corresponds to twice the P_s. The observed P_s is 1.21 (= 2.42 / 2) μCcm^{-2} for 4F-XY-C16, which is slightly smaller than the expected P_s.

Figure 4-9 shows the polarization current curve with the rectangular wave field at a frequency of 20 Hz. All the smectic phases show the well-defined switching peak. The switching rates elucidated as time at the top of peak are very short. These are 11.2 μs for 2F-Z-C16, 5.6 μs for 2F-Y-C16, and 6.4 μs for 4F-XY-C16, which are less than one twentieth of 254.0 μs for C16. Such a distinctly short switching time is due to the fluorine substitution, that is a decrease in viscosity as a result of the weakening of the intermolecular force.[5,8]

4.3.4. Dielectric properties

The dielectric data of smectic phases in 2F-Z-C16, 2F-Y-C16, 4F-XY-C16 and C16, are shown in Figures 4-10(a) and (b) where the real (ε') and imaginary (ε'') parts of the dielectric constants are plotted against the frequencies of 10^1 Hz to 10^7 Hz, respectively. Two relaxation modes can be observed in this frequency range. One is the low frequency (LF) mode, which is observed at approximately ~5 kHz in the SmC_AP_A phases of 2F-Y-C16 and 4F-XY-C16. The huge dielectric constants and low relaxation frequencies (f_r) reveal that the mode is the collective fluctuation mode of polarization, which is typically observed in the antiferroelectric phases.[16,17] Another is the high frequency (HF) mode appearing at approximately 100 kHz, which is observed in the $SmAP_F$ phase of 2F-Z-C16 and SmC_AP_A phase of C16. This HF mode is associated with the non-collective molecular rotation around the short axes of mesogens as commonly observed in conventional LC phases.[1,16–19] Here, it should be noted that the LF mode is not observed for the ferroelectric $SmAP_F$ phase of 2F-Z-C16. The explanation for this will be given later.

The dielectric spectra were analyzed by fitting with the following Cole-Cole equation[20]:

$$\varepsilon^* = \varepsilon' - i\varepsilon'' = \varepsilon_\infty + \frac{\Delta\varepsilon}{1 + (i\omega\tau)^{1-\alpha}} \quad 0 < \alpha < 1, \qquad (4-2)$$

where ω is the angular frequency, $\Delta\varepsilon$ (= ε_s - ε_∞) is the dielectric strength, and ε_s and ε_∞ are the "static-frequency" and "infinite-frequency" dielectric constants, respectively. $\tau = 1/(2\pi f_r)$ is the relaxation time (where f_r is the relaxation frequency), and α is the distribution parameter of

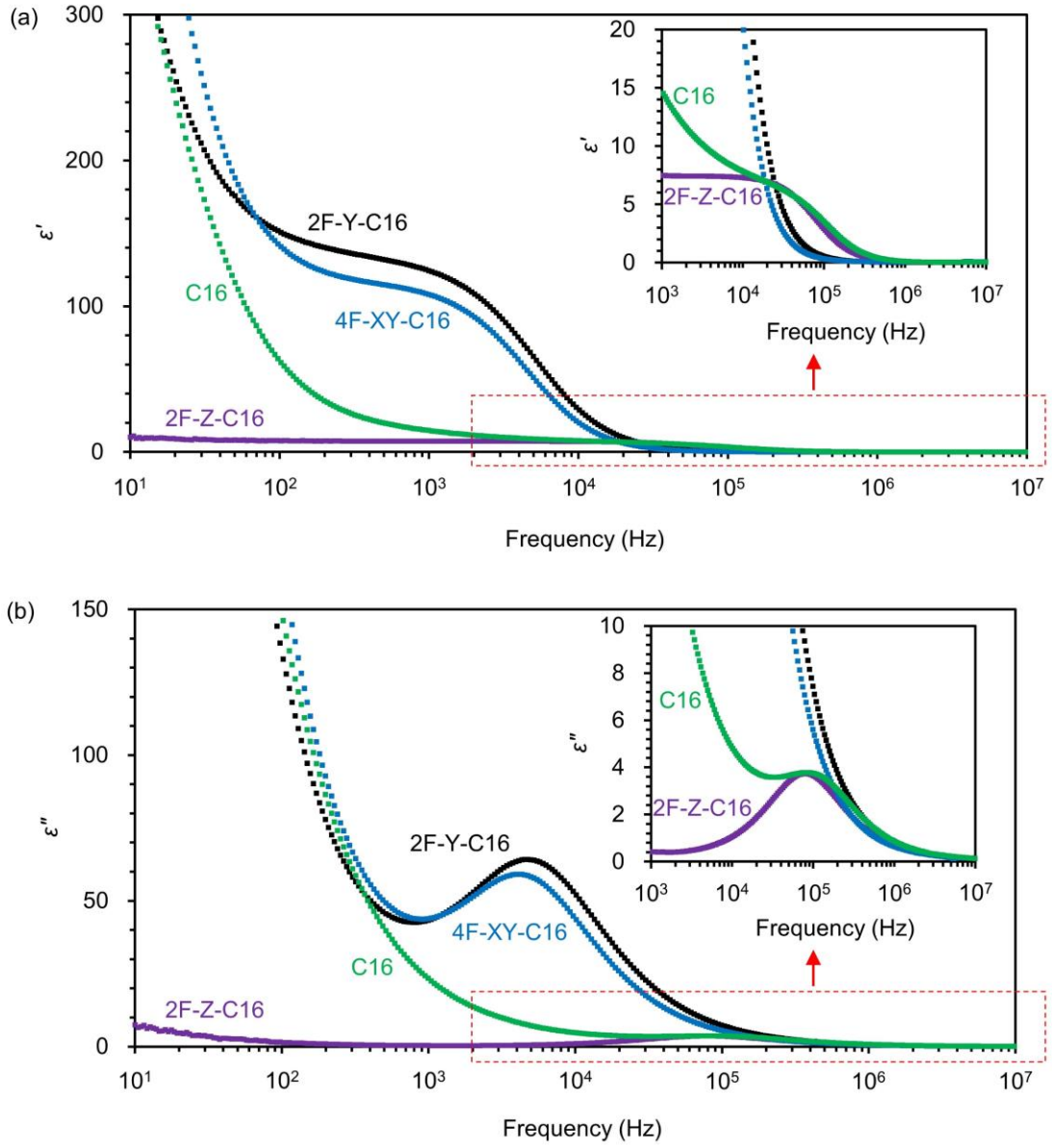

Figure 4-10. Frequency dependences of (a) the real (ε') part and (b) imaginary (ε'') part of the complex dielectric constants for the $SmAP_F$ phase of 2F-Z-C16, the SmC_AP_A phase of 2F-Y-C16, the SmC_AP_A phase of 4F-XY-C16 and the SmC_AP_A phase of C16, measured in a 3 μm-thick cell. In the insets, the vertical axis is expanded to show clearly the dielectric relaxation modes of the 2F-Z-C16 and C16 at around 10^5 Hz.

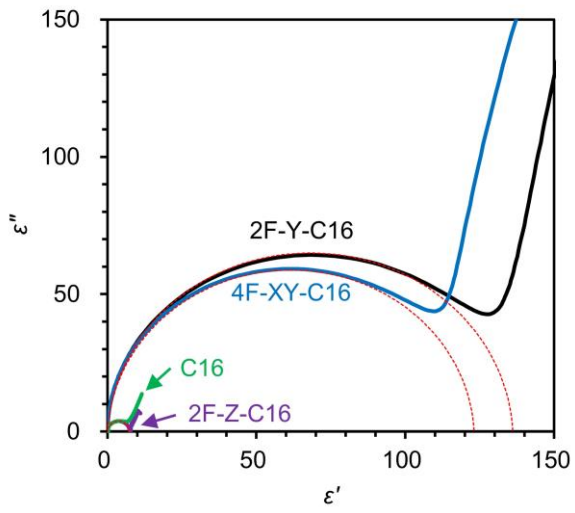

Figure 4-11. Cole-Cole plots for the $SmAP_F$ phase of 2F-Z-C16, the SmC_AP_A phase of 2F-Y-C16, the SmC_AP_A phase of 4F-XY-C16 of and the SmC_AP_A phase of C16 based on the data of Figures 4-10(a) and (b). The dotted curves are obtained by fitting Equation (4-2).

Table 4-4. List of the Cole-Cole parameters, the $\Delta\varepsilon$, f_r and α, collected from the data of Figures 4-10 and 4-11.

	$\Delta\varepsilon$	f_r (Hz)	α
2F-Z-C16	7	7.8×10^4	0
2F-Y-C16	136	4.7×10^3	0.03
4F-XY-C16	123	4.1×10^3	0.03
C16	7	8.2×10^4	0

relaxation time. Figure 4-11 shows the Cole-Cole plots for the collective and non-collective modes. The determined parameters, $\Delta\varepsilon$, f_r and α, in the Cole-Cole equation are listed in Table 4-4. One noticeable point is that the $\Delta\varepsilon$ for the LF mode of the SmC_AP_A phase are large; 136 for 2F-Y-C16 and 123 for 4F-XY-C16. On the other hand, the $SmAP_F$ phase from 2F-Z-C16 and SmC_AP_A phase from C16 show $\Delta\varepsilon$ values less than 10, which is usually obtained as the non-collective rotational mode around the short axis of molecules.

The temperature dependence of the relaxation frequency, f_r, for the non-collective mode of the $SmAP_F$ phase of 2F-Z-C16 and SmC_AP_A phase of C16 follows the standard Arrhenius equation[21,22], and the activation energies of 40 $kJmol^{-1}$ and 81 $kJmol^{-1}$, respectively, are obtained. These values are comparable to those reported.[16] On the other hand, the f_r of the SmC_AP_A phase from 2F-Y-C16 and 4F-XY-C16 is nearly temperature independent as expected for the collective mode (see Figure 4-12).[1,17]

One may consider that the LF mode of the SmC_AP_A cannot be dielectrically detected since

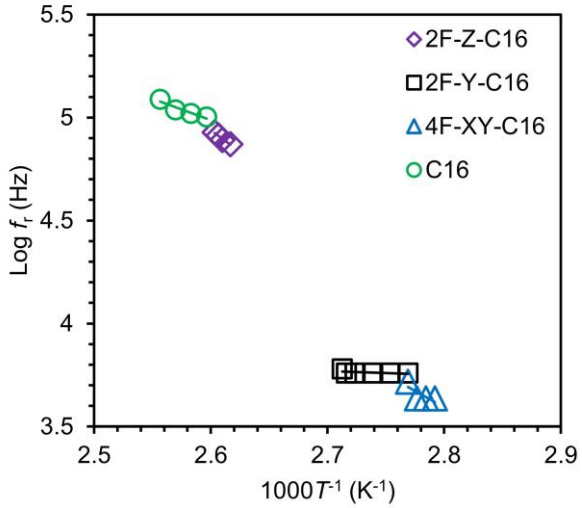

Figure 4-12. Logarithm of the dielectric relaxation frequencies as a function of inverse absolute temperature for 2F-Z-C16, 2F-Y-C16, 4F-XY-C16 and C16, measured in a 3 μm-thick cell.

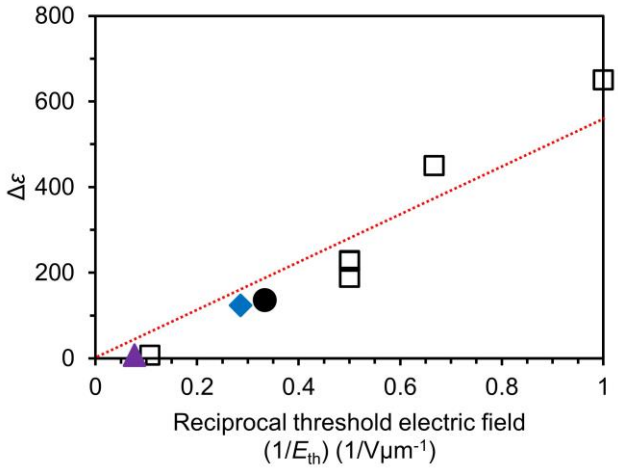

Figure 4-13. Linear correlation between the $\Delta\varepsilon$ and reciprocal E_{th}. The data for 2F-Z-C16, 2F-Y-C16 and 4F-XY-C16 are presented by closed circle, square, and triangle, respectively. As a reference, the open squares are the data collected from Chapter 3 on dimeric molecules. The dotted line is guide for the eyes.

all the polar directions of layers turn around the molecule and keeping their antipolar order form layer to layer. One of the plausible explanations for this is provided that an anti-phase fluctuation of dipoles is likely to occur in adjacent layers; the molecules in neighboring layers fluctuate with a different sign of angle ($\Delta\psi$) that resulting in a temporary non-zero cancellation of neighboring dipoles.[23,24]

On the other hand, it seems curious that the ferroelectric $SmAP_F$ of 2F-Z-C16 does not exhibit the LF mode, referring to the previous reports that $SmAP_F$ in C4 and C16 mixtures exhibit the LF mode giving a huge $\Delta\varepsilon$ of 2000 (see Chapter 2 and 3). However, this can be well understood according to a linear relationship between the reciprocal of the E_{th} and $\Delta\varepsilon$, which is established in Chapter 3. The lower E_{th} (i.e., energy barrier between two polar states) is, the more the

collective fluctuation mode of dipoles is enhanced. The corresponding plots of the $\Delta\varepsilon$ and reciprocal E_{th} of 2F-Y-C16, 2F-Z-C16 and 4F-XY-C16 are given in Figure 4-13, together with the data previously collected. The values fall on a linear line. The E_{th} of the $SmAP_F$ of 2F-Z-C16 is 13.0 $V\mu m^{-1}$, which is much higher than that (0.7 $V\mu m^{-1}$) of the $SmAP_F$ in mixtures of C4 and C16. For such a high value of E_{th}, the $\Delta\varepsilon$ becomes almost zero, in other words, the LF mode is prohibited. The SmC_AP_A of C16 has also a high E_{th} of 9.3 $V\mu m^{-1}$ and then no LF mode is observed, while the LF is clearly detected for the SmC_AP_A phases of 4F-XY-C16 and 2F-Y-C16 with relatively small E_{th} of 3.0–3.5 $V\mu m^{-1}$.

In order to obtain the information of electric-field-effects on the polar order, dielectric measurement was performed under DC bias fields. Figure 4-14 shows the variation of the $\Delta\varepsilon$ and f_r with the DC bias field observed in the SmC_AP_A from 2F-Y-C16 and 4F-XY-C16. The DC bias behavior of the SmC_AP_A phase from 2F-Y-C16 and 4F-XY-C16 is the same as that observed for the $SmAP_A$ phase in Chapter 3. For example, the $\Delta\varepsilon$ and f_r are almost constant up to 2 $V\mu m^{-1}$ for 4F-XY-C16. On further increase of the DC field to 3.5 $V\mu m^{-1}$, a local maximum is observed in the $\Delta\varepsilon$, and a local minimum is observed in the f_r at 3 $V\mu m^{-1}$. The maximum $\Delta\varepsilon$ at 3 $V\mu m^{-1}$ is around 600, which is four times larger than that of the initial value, and the corresponding f_r becomes shorter. Finally, the $\Delta\varepsilon$ becomes zero at around 3.5–4.0 $V\mu m^{-1}$, which is nearly equal to the E_{th} of 3.5 $V\mu m^{-1}$. This behavior is similar to that observed for $SmAP_A$ in the mixtures of C4 and C16 in Chapter 3. Possibly, with the increase of DC bias field, the SmC_AP_A structure partly transforms to the SmC_SP_F structure, and then with a further increase, the suppression of dipoles' fluctuation occurs.

It should be noted that such an enhancement behavior is not observed in the $SmAP_F$ of 2F-Z-C16 and the SmC_AP_A of C16. These two smectic phases invariably show only the non-collective mode even when the DC bias field up to 15 $V\mu m^{-1}$ (larger than E_{th}) is applied.

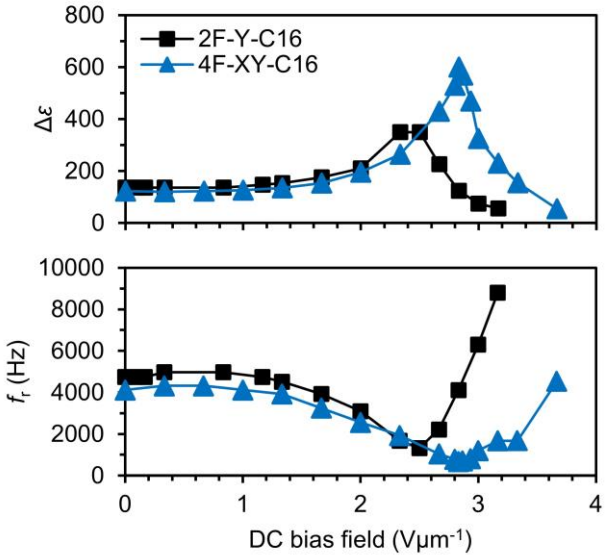

Figure 4-14. DC bias field dependence of the $\Delta\varepsilon$ and f_r for the collective mode in the SmC_AP_A phases of 2F-Y-C16 and 4F-XY-C16, measured in a 3 μm-thick cell.

4.4. Concluding Remarks

Bent-shaped dimeric molecules with fluorine substitution to a standard bent-shaped dimeric molecule (C16) were synthesized. Effects of the fluorine substitution, such as the substituted position and number of the fluorine, were examined on the polar mesophase structures and properties. In all materials, the polar smectic phases are formed; $SmAP_F$ from 2F-Z-C16, and SmC_AP_A from 2F-Y-C16 and 4F-XY-C16. As one of the significant effects, the transition temperatures decrease by 10–30 °C without significantly changing the temperature span of smectic phase. Another effect is observed on the switching rate to the ferroelectric state. The rates are around 10 μs, which are significantly shorter than 250 μs of C16. The decrease in the intermolecular force and the decrease in the viscosity may be attributed to these effects. Further effect was observed on the orientation behavior to the ITO-coated cell. On the ITO cell, the non-fluorine substituted bent-shaped dimeric molecules tend to be aligned homogeneously with both the molecular axes and bent (polar) axes parallel to the surface. In contrast, the fluorine substituted molecules are homogeneously aligned with the bent (polar) direction perpendicular to the surface. This difference of surface anchoring effect is due to the trend that the fluorine dislikes the contact with ITO electrodes.

The ferroelectricity of $SmAP_F$ in 2F-Z-C16 was clarified from microscopic texture, switching behavior and SHG measurement. The fan-shaped texture of $SmAP_F$ and its color are not essentially changed on field-ON and field-OFF. No rotation of extinction direction is also characteristic. This is due to the maintenance of the perpendicular orientation of polar direction to the cell on both of field-ON and field-OFF. Observations of one current peak on a half cycle of triangular wave voltage application and the SHG activity without the electric field also clarify the $SmAP_F$ phase. In the dielectric measurements, the $SmAP_F$ phase does not show the collective mode of polarization at all, but only the non-collective mode. This is in contrast to the fact that the $SmAP_F$ treated in Chapters 2 and 3 shows the huge collective mode giving $\Delta\varepsilon$ of 2000. The reason may be due to the high energy barrier for rotation of dipoles as suggested from the high E_{th} of around 13 $V\mu m^{-1}$, which is much larger than 0.7 $V\mu m^{-1}$ of the $SmAP_F$ treated in Chapter 3.

The SmC_AP_A phases were formed from 2F-Y-C16 and 4F-XY-C16. The tilting of molecules to the layer is well elucidated from the facts that the layer spacing is appreciably smaller than the molecular length and that the extinction direction in microscopic fan-shaped texture is significantly rotated on field-ON. The antiferro-electric structure is identified from the observation of two current peaks on a half cycle of triangular voltage. The reversal polarizations of 1.64 μCcm^{-2} for 2F-Y-C16 and 2.42 μCcm^{-2} for 4F-XY-C16 are much larger than 0.64 μCcm^{-2} of C16. This is due to the increment of dipole moment of molecule; the dipole moments estimated for one-side mesogen are 6.85 D and 7.94 D for 2F-Y-C16 and 4F-XY-C16, respectively, while the value is 5.99 D for C16. Fluorine substitution on the aromatic core can thus increase the dipole moment of molecule and simultaneously P_s. It should be noted that 2.42 μCcm^{-2} of 4F-XY-C16 is much larger compared to those so far reported in the dimeric and

bent-shaped banana molecules.[1,9,25–27] In the dielectric measurements, these SmC_AP_A show the LF mode at around 5 kHz and with $\Delta\varepsilon = \sim 150$. This is in contrast with the fact that the $SmAP_F$ of 2F-Z-C16 and SmC_AP_A of C16 do not show the LF mode. The low E_{th} of around 3 $V\mu m^{-1}$ in electric switching is considered to be the reason for the exhibition of the LF mode.

References

(1) Guo, L.; Gorecka, E.; Pociecha, D.; Vaupotič, N.; Čepič, M.; Reddy, R. A.; Gornik, K.; Araoka, F.; Clark, N. A.; Walba, D. M., et al. Ferroelectric behavior of orthogonal smectic phase made of bent-core molecules. *Phys. Rev. E* **2011**, *84*, 031706.

(2) Kumar, J.; Prasad, C. Ferroelectric nematic and ferrielectric smectic mesophases in an achiral bent-core azo compound. *J. Phys. Chem. B* **2018**, *122*, 2998–3007.

(3) Reddy, R. A.; Sadashiva, B. K. Influence of fluorine substituent on the mesomorphic properties of five-ring ester banana-shaped molecules. *Liq. Cryst.* **2003**, *30*, 1031–1050.

(4) Shreenivasa Murthy, H. N; Sadashiva, B. K. Influence of a fluorine substituent on the mesomorphic properties of unsymmetrical five-ring bent-core compounds. *J. Mater. Chem.* **2004**, *14*, 2813–2821.

(5) Hird, M. Fluorinated liquid crystals – properties and applications. *Chem. Soc. Rev.* **2007**, *36*, 2070–2095.

(6) Li, J.; Nishikawa, H.; Kougo, J.; Zhou, J.; Dai, S.; Tang, W.; Zhao, X.; Hisai, Y.; Huang, M.; Aya, S. Development of ferroelectric nematic fluids with giant-ε dielectricity and nonlinear optical properties. *Sci. Adv.* **2021**, *7*, eabf5047.

(7) Bedel, J. P.; Rouillon, J. C.; Marcerou, J. P.; Laguerre, M.; Nguyen, H. T.; Achard, M. F. Novel mesophases in fluorine substituted banana-shaped mesogens. *Liq. Cryst.* **2000**, *27*, 1411–1421.

(8) Yokokoji, O.; Shimizu, K.; Inoue, S. 5,6-Difluoro-1H-indene derivatives: novel core structure of liquid crystals with high Δn and $\Delta\varepsilon$. *Liq. Cryst.* **2009**, *36*, 1–6.

(9) Izumi, T.; Kang, S.; Niori, T.; Takanishi, Y.; Takezoe, H.; Watanabe, J. Smectic mesophase behavior of dimeric compounds showing antiferroelectricity, frustration and chirality. *Jpn. J. Appl. Phys.* **2006**, *45*, 1506–1514.

(10) Frisch, M.; Trucks, G.; Schlegel, H.B.; Scuseria, G. E.; Robb, M. A.; Cheeseman, J. R.; Scalmani, G.; Barone, V.; Mennucci, B.; Petersson, G. A., et al. Gaussian 09, revision a. 02. Wallingford (CT): Gaussian. Inc; 2009. p. 200.

(11) Hagar, M.; Ahmed, H. A.; Alhaddad, O. A. Experimental and theoretical approaches of molecular geometry and mesophase behaviour relationship of laterally substituted azopyridines. *Liq. Cryst.* **2019**, *46*, 1440–1451.

(12) Thisayukta, J.; Takezoe, H.; Watanabe, J. Study on helical structure of the B_4 phase formed from achiral banana-shaped molecule. *Jpn. J. Appl. Phys.* **2001**, *40*, 3277–3288.

(13) Watanabe, J.; Hayashi, M. Thermotropic liquid crystals of polyesters having a mesogenic p,p'-bibenzoate unit. 2. X-ray study on smectic mesophase structures of BB-5 and BB-6.

Macromolecules **1989**, *22*, 4083–4088.

(14) Izumi T.; Naitou, Y.; Shimbo, Y.; Takanishi, Y.; Takezoe, H.; Watanabe, J. Several types of bilayer smectic liquid crystals with ferroelectric and antiferroelectric properties in binary mixture of dimeric compounds. *J. Phys. Chem. B* **2006**, *110*, 23911–23919.

(15) Peercy, P. S. Measurement of the "soft" mode and coupled modes in the paraelectric and ferroelectric phases of KH_2PO_4 at high pressure, *Phys. Rev. B* **1975**, *12*, 2725– 2740.

(16) Hiraoka, K.; Takezoe, H.; Fukuda, A. Dielectric relaxation modes in the antiferroelectric smectic CA* phase, *Ferroelectrics* **1993**, *147*, 13–25.

(17) Fuente, M.; Dunmur, D. Dielectric Properties of Liquid Crystals. In *Handbook of liquid crystals*, 2nd ed.; Goodby, J.; Collings, P.; Kato, T.; Tschierske, C.; Gleeson, H.; Raynes, P., Eds.; Wiley-VCH Verlag GmbH & Co KGaA: Germany, 2014; pp 1−46.

(18) Khened, S.; Prasad, S.; Shivkumar, B.; Sadashiva, B. K. Dielectric studies of Goldstone mode and soft mode in the vicinity of the A-C* transition. *J. Phys. II France* **1991**, *1*, 171–180.

(19) Hatano, J.; Hanakai, Y.; Furue, H.; Uehara, H.; Saito, S.; Murashiro, K. Phase sequence in smectic liquid crystals having fluorophenyl group in the core. *Jpn. J. Appl. Phys.* **1994**, *33*, 5498–5502.

(20) Cole, K.; Cole, R. Dispersion and absorption in dielectrics I, alternating current characteristics, *J. Chem. Phys.* **1941**, *9*, 341–351.

(21) Marik, M.; Jana, D.; Majumder, K.; Chaudhuri, B. K. Dielectric behavior in B1 and B2 phases composed of unsymmetrical bent shaped liquid crystal molecules. *Mol. Cryst. Liq. Cryst.* **2015**, *606*, 111–125.

(22) Różański, S. Dielectric properties of liquid crystal formed by laterally fluorine-substituted banana-shaped molecules, *Phase Transit.* **2018**, *91*, 1007–1016.

(23) Buivydas, M.; Gouda, F.; Lagerwall, S. T.; Stebler, B. The molecular aspect of the double absorption peak in the dielectric spectrum of the antiferroelectric liquid crystal phase. *Liq. Cryst.* **1995**, *18*, 879–886.

(24) Zennyoji, M.; Takanishi, Y.; Ishikawa, K.; Thisayukta, J.; Watanabe, J.; Takezoe, H. Electrooptic and dielectric properties in bent-shaped liquid crystals. *Jpn. J. Appl. Phys.* **2000**, *39*, 3536–3541.

(25) Jákli, A.; Lavrentovich, O. D.; Selinger, J. V. Physics of liquid crystals of bent-shaped molecules. *Rev. Mod. Phys.* **2018**, *90*, 045004.

(26) Gomola, K.; Guo, L.; Dhara, S.; Shimbo, Y.; Gorecka, E.; Pociecha, D.; Mieczkowski, J.; Takezoe, H. Syntheses and characterization of novel asymmetric bent-core mesogens exhibiting polar smectic phases. *J. Mater. Chem.* **2009**, *19*, 4240–4247.

(27) Watanabe, J.; Izumi T.; Niori, T.; Zennyoji, M.; Takanishi, Y.; Takezoe, H. Smectic mesophase properties of dimeric compounds 2 distinct formation of smectic structures with antiferroelectric ordering and frustration. *Mol. Cryst. Liq. Cryst.* **2000**, *346*, 77–86.

CHAPTER 5

Three Distinct Polar Phases, Isotropic, Nematic, and Smectic-A Phases, Formed from a Fluoro-Substituted Dimeric Molecule with Large Dipole Moment

5.1. Introduction

As mentioned in Chapter 4, a clear linear relationship between dipole moment and spontaneous polarization (P_s) was found in fluorine-substituted dimeric molecules. An increase in dipole moment also leads not only to an increase in the P_s but also to an increase in dielectric strength ($\Delta\varepsilon$).[1] The longitudinal dipole moment is increased by attaching the polar groups to the aromatic mesogens. A typical method is the fluorine substitution. By using the cyanobiphenyl, McDonnell et al. reported that the fluorine substitution is an effective method to increase the dipole moment.[2] Furthermore, Nishikawa et al. also reported that DIO with fluorine possesses a large dipole moment of 9.4 D, resulting in the high dielectric constant of 10000 and the high P_s of 4.4 μCcm^{-2}.[1] Similar results have been reported in fluorine-substituted bent-shaped dimeric molecules; an increase in the number of aromatic rings and fluorine substitution was found to result an increase in the dipole moment.[3-5]

In this chapter, based on this strategy, a di-5(3FM-C4) molecule (see Figure 5-1) with 3 benzene rings having one fluorine substitution in each is prepared and the ferroelectric properties is examined.

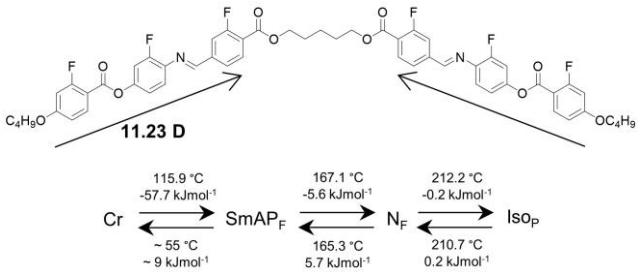

Figure 5-1. Molecular structure and phase sequence of di-5(3FM-C4T). The transition temperatures and enthalpy changes are taken from the DSC 2nd heating and 1st cooling runs. The dipole moment value along the long axis of one-side mesogen is calculated by density functional theory. The arrows represent the direction of the dipole moment.

5.2. Experimental Section

5.2.1. Materials

Unless otherwise noted, reagents and solvents were purchased from commercial suppliers and used without further purification.

5.2.2. Measurements

Nuclear magnetic resonance (NMR) spectroscopy measurements were carried out on a Bruker AVANCE-500 spectrometer (500 MHz for ^{1}H, 470 MHz for ^{19}F and 126 MHz for ^{13}C). Chemical shifts (δ) are expressed relative to the resonances of the residual non-deuterated solvent for ^{1}H ($CDCl_3$: $^{1}H(\delta)$ = 7.26 ppm and DMSO-d_6: $^{1}H(\delta)$ = 2.49 ppm), the resonances of the residual solvent for ^{13}C ($CDCl_3$: $^{13}C(\delta)$ = 77.16 ppm and DMSO-d_6: $^{13}C(\delta)$ = 39.52 ppm), the resonance of CF_3COOH as external standard for ^{19}F (CF_3COOH: $^{19}F(\delta)$ = –76.55 ppm). Absolute values of the coupling constants are given in Hertz (Hz), regardless of their sign. Multiplicities are abbreviated as singlet (s), doublet (d), doublet of doublets (dd), triplet (t), quartet (q), multiplet (m) and broad (br). The elemental analyses (C, H, N) were carried out on a MICRO CORDER JM10 and the element analysis (O) were carried out on a vario MICRO cube. The phase transition temperatures were determined by differential scanning calorimetry (DSC) (PerkinElmer DSC8500) at a rate of 5 °Cmin^{-1} under 1st cooling and 2nd heating run. Optical microscopic, electro-optical, dielectric and SHG investigations were performed using glass cells coated with indium tin oxide (ITO) electrodes, which is commercially available from EHC Co., Ltd. Furthermore, the ITO cell coated with polyimide was used to promote homogeneous alignment of nematic LC specifically for the microscopic observation of texture. The area of the ITO electrodes was 100 mm^2, and the cell thicknesses of the ITO electrodes were 3 μm. Observation of the texture and identification of the mesophases were carried out using a polarizing optical microscope (POM) (OLYMPUS BX53) equipped with a hot stage and a temperature controller (Mettler Toledo FP 82HT). X-ray diffraction (XRD) measurements were performed using D8 DISCOVER (BRUKER) with Cu K_α radiation. The sample was contained in a capillary tube with the diameter of 1 mm and the alignment of molecules was performed under the magnetic field applied perpendicularly to the capillary tube. The polarization reversal current was observed by applying a triangular wave voltage using a high-speed amplifier (FLC Electronics, F20A) connected to a function generator (NF Electronic Instruments, WF1945B). The SHG measurement was performed using a 10 Hz Nd:YAG laser (Minilite-II) of λ = 1064 nm as a fundamental beam, and in the *p*-in and *p*-out polarization combinations. The incidence angle of the laser to the sample cell settled in a heater block was 45°. The SHG signal was detected by a photomultiplier tube (Hamamatsu model-R1924A) and the outputs from the photomultiplier tube were accumulated by a BOXCAR integrator (Stanford Research Systems). Note that prior to the SHG measurement, a triangular wave application (40 V_{pp}, 1 Hz) treatment was processed at the temperature of the $SmAP_F$ phase. The SHG measurements of all phases were performed without an external electric field. The

complex dielectric constants were measured in a frequency range between 10^0 Hz and 10^7 Hz with an impedance analyzer (NF Electronic Instruments, FRA51615) and with the electric voltage of 1 V_{pp}.

5.2.3. Synthesis

The fluoro-substituted molecule of di-5(3FM-C4T) was newly synthesized in this chapter. The general synthesis procedure (see Scheme 5-1) and the characterization results for all synthesized compounds are provided below.

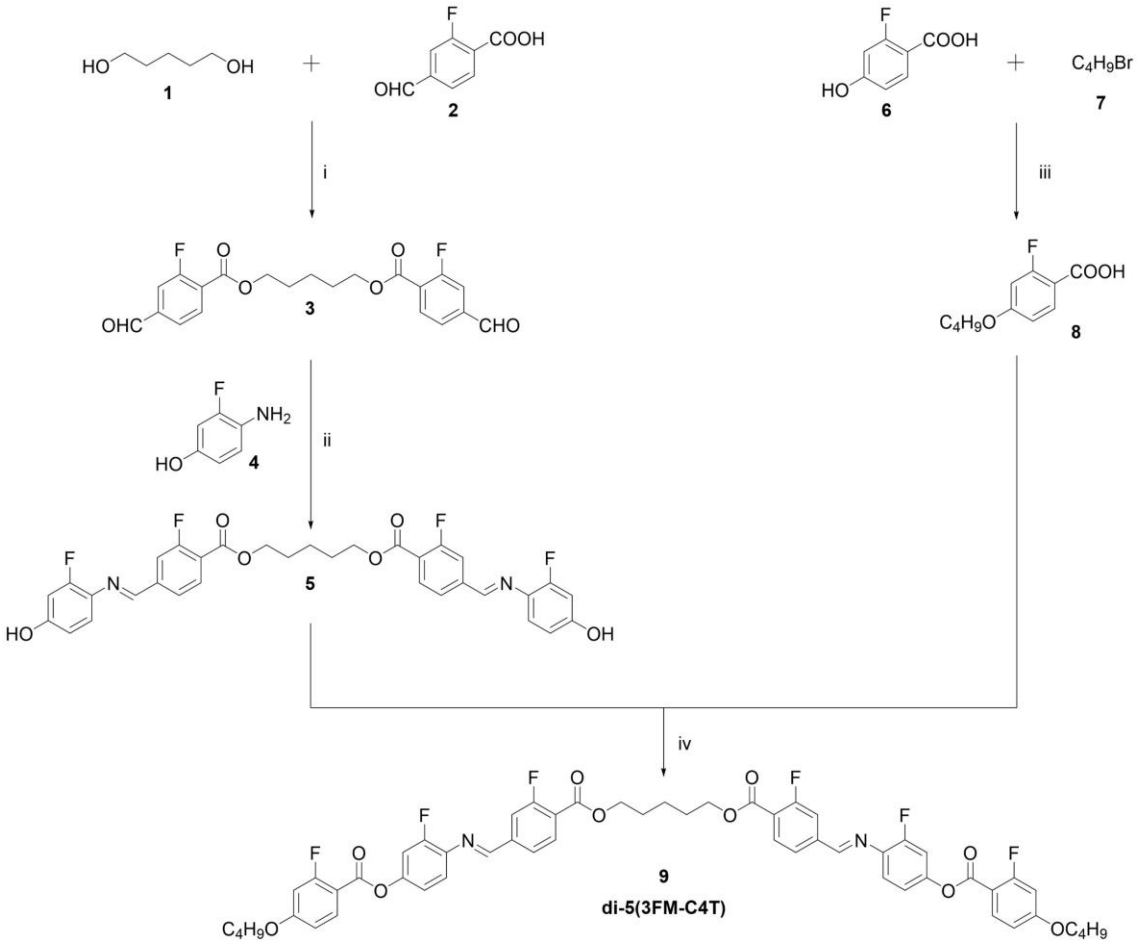

Scheme 5-1. Synthetic route for the preparation the fluorine-substituted bent-shaped dimeric molecules. Reagents and conditions: (i) 1-(3-dimethylaminopropyl)-3-ethylcarbodiimideethanol, ethyl acetate, 4-dimethylaminopyridine, room temperature, 15 hours, (ii) ethanol, reflux, 4 hours, (iii) potassium hydroxide, ethanol, water, reflux, 15 hours, (iv) 1-(3-dimethylaminopropyl)-3-ethylcarbodiimideethanol, tetrahydrofuran, 4-dimethylaminopyridine, room temperature, 15 hours.

5.2.3.1. Synthesis of 3

In a flask equipped with a magnetic stirrer and a nitrogen inlet were prepared. 1,5-pentanediol (**1**) (1.23 g, 11.81 mmol), 2-fluoro-4-formylbenzoic acid (**2**) (3.97 g, 23.62 mmol), 1-(3-dimethylaminopropyl)-3-ethylcarbodiimideethanol (4.40 g, 28.34 mmol), and ethyl acetate (39.80 g). 4-dimethylaminopyridine (0.35 g, 2.83 mmol) were then added to the solution at room temperature. The solution was stirred at room temperature for 15 hours. Then, the solution was diluted with water and ethyl acetate. The organic layer was extracted with water. The solvent was evaporated, and residue was purified by chromatography on silica gel using chloroform eluent to give **3** (1.24 g, 26 %) as a white solid.

For **3**, ^{1}H NMR (500 MHz, $CDCl_3$, 25 °C): δ (ppm) 10.05 (s, 2H, C*H*O), 8.09 (t, J = 7.3 Hz, 2H, Ar-*H*), 7.72 (d, J = 7.9 Hz, 2H, Ar-*H*), 7.62 (d, J = 10.1 Hz, 2H, Ar-*H*), 4.41 (t, J = 6.4 Hz, 4H, COOCH_2), 1.91-1.85 (m, 4H, $COOCH_2CH_2$), 1.68-1.62 (m, 2H, $COOCH_2CH_2CH_2$). ^{19}F NMR (470 MHz, $CDCl_3$, 25 °C): δ (ppm) –107.65 (t, J = 8.2 Hz, 2F, Ar-*F*). ^{13}C NMR (125 MHz, $CDCl_3$, 25 °C): δ (ppm) 190.14, 163.65, 163.62, 163.02, 160.93, 140.78, 140.72, 132.97, 124.96, 124.93, 124.04, 123.95, 117.23, 117.05, 65.62, 28.14, 22.47.

5.2.3.2. Synthesis of 5

In a flask equipped with a magnetic stirrer, a reflux condenser and a nitrogen inlet were placed **3** (0.93 g, 2.30 mmol), 4-amino-3-fluorophenol (**4**) (0.73 g, 5.76 mmol) and ethanol (14.98 g). The solution was stirred and heated under reflux for 4 hours. The solution was concentrated by using a rotary evaporator. The residue was recrystallized from ethanol/water (1/1) to give **5** (1.30 g, 90 %) as a red solid.

For **5**, ^{1}H NMR (500 MHz, DMSO-d_6, 25 °C): δ (ppm) 10.10 (s, 2H, Ar-O*H*), 8.72 (s, 2H, N=C*H*), 7.99 (t, J = 7.7 Hz, 2H, Ar-*H*), 7.81 (dd, J = 8.2, 1.3 Hz, 2H, Ar-*H*), 7.31 (t, J = 9.0 Hz, 2H, Ar-*H*), 6.69-6.65 (m, 4H, Ar-*H*), 4.34 (t, J = 6.3 Hz, 4H, COOCH_2), 1.83-1.77 (m, 4H, $COOCH_2CH_2$), 1.61-1.55 (m, 2H, $COOCH_2CH_2CH_2$). ^{19}F NMR (470 MHz, DMSO-d_6, 25 °C): δ (ppm) –109.95 (t, J = 9.1 Hz, 2F, Ar-*F*), –122.26 (t, J = 10.9 Hz, 2F, Ar-*F*). ^{13}C NMR (125 MHz, DMSO-d_6, 25 °C): δ (ppm) 163.66, 163.64, 162.58, 160.53, 158.64, 158.55, 158.09, 157.05, 156.11, 142.88, 142.81, 132.71, 129.84, 129.76, 124.50, 122.11, 122.09, 120.44, 120.35. 116.50, 116.31, 112.27, 112.25, 103.94, 103.76, 65.40, 28.03, 22.34.

5.2.3.3. Synthesis of 8

In a flask equipped with a magnetic stirrer, a reflux condenser and a nitrogen inlet were placed with addition of 2-fluoro-4-hydroxybenzoic acid (**6**) (2.09 g, 13.41 mmol), 1-bromobutane (**7**) (2.02 g, 14.75 mmol), 85% potassium hydroxide (1.95 g, 29.51 mmol), ethanol (48.90 g) and water (16.50 g). The solution was stirred and heated under reflux for 15 hours. The solution was poured into water and acidified by adding concentrated hydrochloric acid. The precipitate was filtered and washed with hexane. The product was dried at 50 °C *in vacuo* to give **8** (1.71 g, 60 %) as a white solid.

For **8**, ^{1}H NMR (500 MHz, $CDCl_3$, 25 °C): δ (ppm) 7.97 (t, J = 8.7 Hz, 1H, Ar-*H*), 6.73 (dd, J = 8.8, 2.3 Hz, 1H, Ar-*H*), 6.65 (dd, J = 12.9, 2.4 Hz, 1H, Ar-*H*), 4.01 (t, J = 6.5 Hz, 2H, OCH_2), 1.80-1.76 (m, 2H, OCH_2CH_2), 1.53-1.46 (m, 2H, $OCH_2CH_2CH_2$), 0.99 (t, J = 7.4 Hz, 3H, CH_2CH_3). ^{19}F NMR (470 MHz, $CDCl_3$, 25 °C): δ (ppm) –104.85 (t, J = 10.5 Hz, 1F, Ar-*F*). ^{13}C NMR (125 MHz, $CDCl_3$, 25 °C): δ (ppm) 169.44, 169.41, 165.32, 165.15, 165.06, 163.24, 134.06, 134.05, 110.82, 110.80, 102.87, 102.67, 68.50, 30.94, 19.13, 13.76.

5.2.3.4. Synthesis of 9

In a flask equipped with a magnetic stirrer and a nitrogen inlet were placed, and **5** (0.30 g, 0.48 mmol), **8** (0.20 g, 0.95 mmol), 1-(3-dimethylaminopropyl)-3-ethylcarbodiimideethanol (0.15 g, 0.95 mmol), and tetrahydrofuran (5.93 g). 4-dimethylaminopyridine (0.01 g, 0.10 mmol) were added to the solution at room temperature. The solution was stirred at room temperature for 15 hours. The solution was evaporated and the residue was washed with ethanol. The residue was purified by chromatography on activated alumina using chloroform eluent, and recrystallized from chloroform/ethanol (1/1) to give **9** (di-5(3FM-C4T)) (0.18 g, 36 %) as a yellow solid.

For **9**, ^{1}H NMR (500 MHz, $CDCl_3$, 25 °C): δ (ppm) 8.56 (s, 2H, N=C*H*), 8.04-7.98 (m, 4H, Ar-*H*), 7.73-7.69 (m, 4H, Ar-*H*), 7.21 (t, J = 8.8 Hz, 2H, Ar-*H*), 7.11-7.04 (m, 4H, Ar-*H*), 6.75 (dd, J = 8.9, 2.3 Hz, 2H, Ar-*H*), 6.66 (dd, J = 12.7, 2.4 Hz, 2H, Ar-*H*), 4.42 (t, J = 6.3 Hz, 4H, $COOCH_2$), 4.02 (t, J = 6.5 Hz, 4H, OCH_2), 1.92-1.86 (m, 4H, $COOCH_2CH_2$), 1.84-1.78 (m, 4H, OCH_2CH_2), 1.71-1.65 (m, 2H, $COOCH_2CH_2CH_2$), 1.55-1.48 (m, 4H, $OCH_2CH_2CH_2$), 1.00 (t, J = 7.4 Hz, 6H, CH_2CH_3). ^{19}F NMR (470 MHz, $CDCl_3$, 25 °C): δ (ppm) –104.30 (t, J = 10.4 Hz, 2F, Ar-*F*), –108.56 (t, J = 8.7 Hz, 2F, Ar-*F*), –122.75 (t, J = 9.9 Hz, 2F, Ar-*F*). ^{13}C NMR (125 MHz, $CDCl_3$, 25 °C): δ (ppm) 165.10, 165.07, 165.01, 164.05, 164.02, 163.10, 162.99, 162.11, 162.08, 161.02, 160.15, 156.06, 154.05, 149.49, 149.41, 141.76, 136.45, 136.37, 133.82, 132.56, 124.43, 124.41, 122.34, 121.31, 121.23, 118.07, 116.55, 116.36, 111.00, 110.93, 110.91, 110.84, 109.36, 109.28. 102.96, 102.76, 68.57, 65.26, 30.96, 28.18, 22.51, 19.14, 13.79. Elemental analysis: calculated for $C_{55}H_{48}F_6N_2O_{10}$, C 65.34, H 4.79, N 2.77, O 15.83; found, C 65.38, H 4.82, N 2.75, O 15.87%.

5.2.4. Calculation of molecular length and dipole moment

The molecular parameter such as the molecular length and dipole moment was calculated by density functional theory. It was carried out by Gaussian 09 software, selecting DFT/B3LYP methods using 6-31G (d,p) basis.[6] The geometries were optimized by minimizing the energies with respect to all geometrical parameters without imposing any molecular symmetry constraints.

5.3. Results

5.3.1. Molecular parameters obtained by density functional theory

The dipole moment of its one-side mesogenic core is estimated as 11.23 D (see Figure 5-1), which is relatively larger than those previously reported.[1] Detail dipole moment components (μ_x, μ_y, μ_z) are 9.33, -4.99 and 3.76, respectively. Here, the resultant dipole moment (μ) is represented by $(\mu_x^2 + \mu_y^2 + \mu_z^2)^{1/2}$.

5.3.2. Transition behaviors

The DSC thermograms are shown in Figure 5-2 and their thermodynamic DSC data based on 1st cooling and 2nd heating are listed in Figure 5-1. As described later in details, di-5(3FM-C4T) forms the polar isotropic (Iso_P), N_F and $SmAP_F$ phases. On cooling process, the highest temperature Iso_P phase is transformed to the N_F phase at 211 °C, showing a very small, but obvious DSC peak. The enthalpy change is less than 0.2 $kJmol^{-1}$. The N_F - $SmAP_F$ phase transition is observed at 165 °C with the substantial enthalpy change of 5.7 $kJmol^{-1}$. On further cooling, no clear transition to crystal (Cr) is detected although some broad and small peaks are observed at around 55 °C. The crystallization takes place after a prolonged stay below room temperature or by some mechanical or electrical stimulus. The resulting Cr melts at 116 °C on heating. In some cases, the supercooling nature of the LC phase and the lower crystal melting temperatures are observed due to the fluorine-substituted molecules with weaker intermolecular forces.[5] It is interesting to note that the N_F phase as well as the $SmAP_F$, Iso_P phases are enantiotropic, giving a wide accessible temperature range while almost all N_F phases reported are monotropic.[1,7-16]

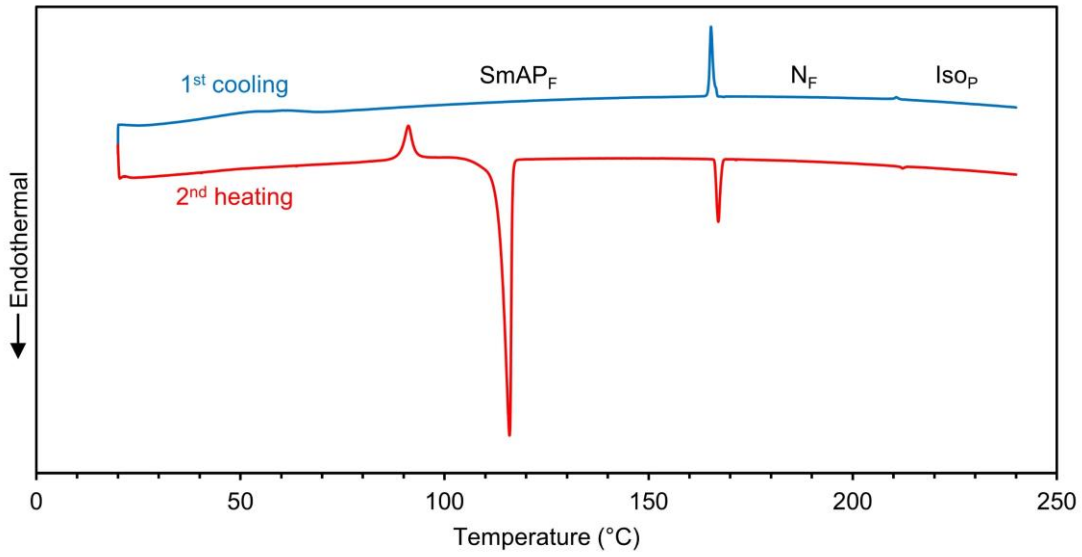

Figure 5-2. DSC thermogram of di-5(3FM-C4T). Scanning rate is 5 $°Cmin^{-1}$.

5.3.3. Optical microscopic observation

The transitions between the Iso_P, N_F and $SmAP_F$ phases can be well detected by optical microscopic observation as shown in Figure 5-3. Here, the observation was done in two types of cells. One is the ITO coated cell (ITO-cell) and another is the ITO-cell further coated by polyimide (PI-ITO-cell). In the ITO-cell, the N_F phase is aligned homeotropically and then the texture is completely dark like that in the Iso_P phase (see Figures 5-3(a) and (b)). In the PI-ITO-cell, on the other hand, the N_F phase is aligned homogeneously presenting the typical birefringent Schlieren texture (Figure 5-3(e)) and then, the transition to the Iso_P phase was clearly detected by the disappearance of the birefringence (compare Figures 5-3(d) and (e)). On cooling from the N_F phase, the $SmAP_F$ phase appears as a homogeneous fan-shaped texture (see Figures 5-3(c) and (f)), which is well developed regardless of the homeotropic and homogeneous orientation in the preceding N_F phase. This preferential homogeneous alignment suggests that the molecules in this phase assume the bent-shaped conformation as shown in Chapters 2, 3 and 4.

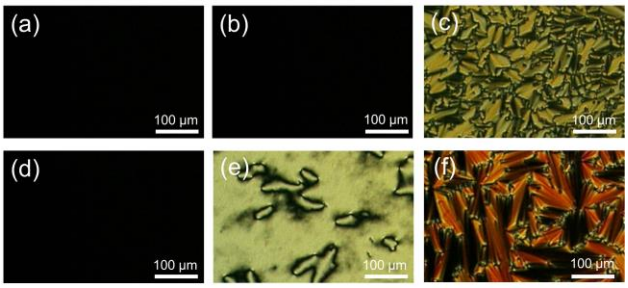

Figure 5-3. Microscopic textures of (a) the Iso_P, (b) N_F and (c) $SmAP_F$ phases in a 3 μm-thick ITO-cell. Microscopic textures of (d) the Iso_P, (e) N_F and (f) $SmAP_F$ phases in a 3 μm-thick PI-ITO-cell.

5.3.4. X-ray measurements

Figure 5-4 shows the two-dimensional XRD patterns taken in different phases. Here, the material is contained in the glass tube, and the magnetic field was applied perpendicularly to the tube. In Figure 5-4, the magnetic field is in a vertical direction.

Comparing the X-ray patterns in Figures 5-4(a) and (b), the uniaxial orientation due to the magnetic field is successfully achieved in the N_F phase while no orientation in the Iso_P phase as expected. Its oriented X-ray pattern includes a streak with the spacing of 25 Å on the meridian (magnetic field direction) and outer broad reflections with a spacing of 4.5 Å on the equator, indicating that N_F phase is composed of molecules with the rod-shaped conformation, but not the bent-shaped one. The 25 Å meridional streak roughly corresponds to the length (24.3 Å) of the one-sided mesogenic core.

Figures 5-4(c)–(e) show the XRD patterns of the $SmAP_F$ phase. Despite of the uniaxial orientation of the preceding N_F phase, the $SmAP_F$ phase exhibits multiple different orientation

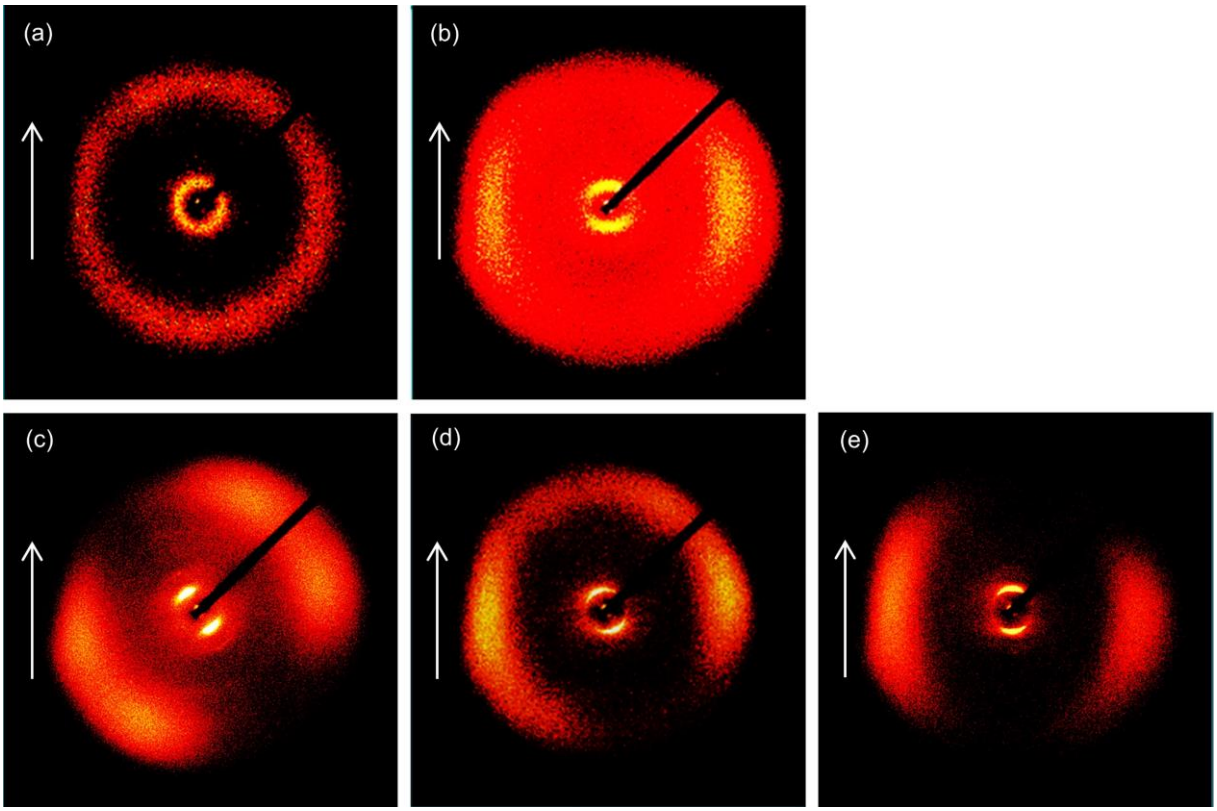

Figure 5-4. XRD patterns of di-5(3FM-C4T) taken under the magnetic field (given by the arrow): (a) the Iso_P phase at 220 °C, (b) the N_F phase at 195 °C and (c)-(e) the $SmAP_F$ phase at 150 °C. For the $SmAP_F$ phase, three representative patterns are presented (refer to the text).

patterns although all of them include a sharp layer refection with a spacing of 23.4 Å and an outer broad reflection with a spacing of 4.5 Å. In Figures 5-4(c)–(e), three representative patterns are presented. In Figure 5-4(c), the layer reflection appears in a tilt direction of 30° from meridional line (magnetic field direction), and the broad outer reflections split into two portions; one set of the reflections are placed on the equator while another set of the reflections is on the position tilted by ~60° from the equator. In Figure 5-4(e), the layer reflection appears on meridian and the broad outer reflection appears on the equator. The central pattern of Figure 5-4(d) shows intermediate characteristics between these twos.

From Figure 5-4(c), it is obvious that the $SmAP_F$ phase is constructed by the bent-shaped molecules[17-19] in a way that the bent molecules are aligned perpendicularly to the layer, the side wing mesogens are tilted by 30° to the layer, and the normal of the smectic layer is tilted by 30° to the magnetic field direction. The reason why various patterns appear in the $SmAP_F$ phase under the magnetic field will be discussed later.

5.3.5. Switching behaviors

Ferroelectricity can be determined from the observation of a polarization reversal current under the application of a triangular wave voltage. Typical switching current data and the optical microscopic textures as observed in the ITO cell are shown in Figures 5-5–5-7.

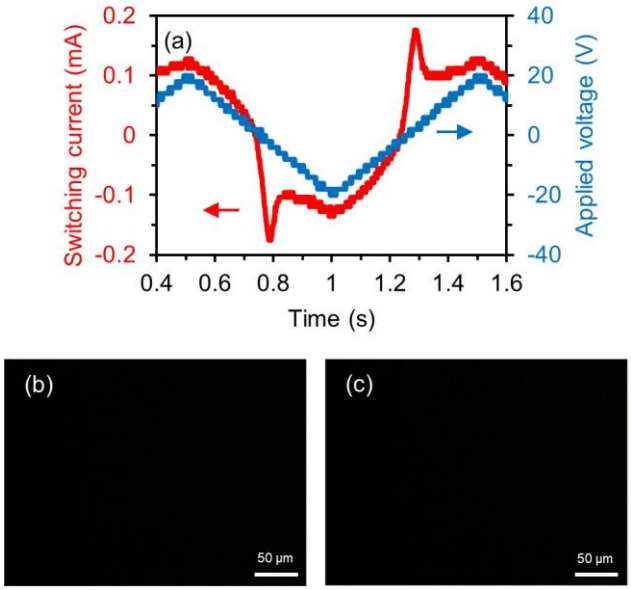

Figure 5-5. (a) Polarization reversal current for the N_F phase at 180 °C measured by applying a triangle wave field (40 V_{pp}, 1 Hz), in a 3 μm-thick ITO-cell. (b) and (c) are the optical microscopic textures in the same cell on field-OFF and field-ON, respectively.

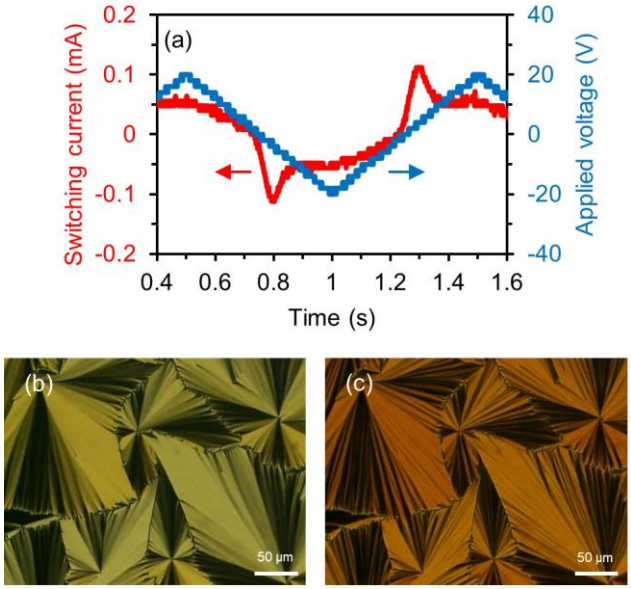

Figure 5-6. (a) Polarization reversal current for the $SmAP_F$ phase at 150 °C measured by applying a triangle wave field (40 V_{pp}, 1 Hz), in a 3 μm-thick ITO-cell. (b) and (c) are the optical microscopic textures in the same cell on field-OFF and field-ON, respectively.

At first, the data on the N_F phase is explained. By applying a triangular voltage wave, the N_F phase shows one current peak on a half cycle (see Figure 5-5(a)), which is typical for the ferroelectricity. The microscopic texture under the high voltage is totally dark on field-ON (see Figure 5-5(c)), meaning that the polarization direction corresponds to the n-director. The reversal polarization estimated as the integral of the current peak in a half cycle is around 8 μCcm^{-2}. In Figure 5-8, the reversal P_s and threshold electric field (E_{th}) are plotted against the

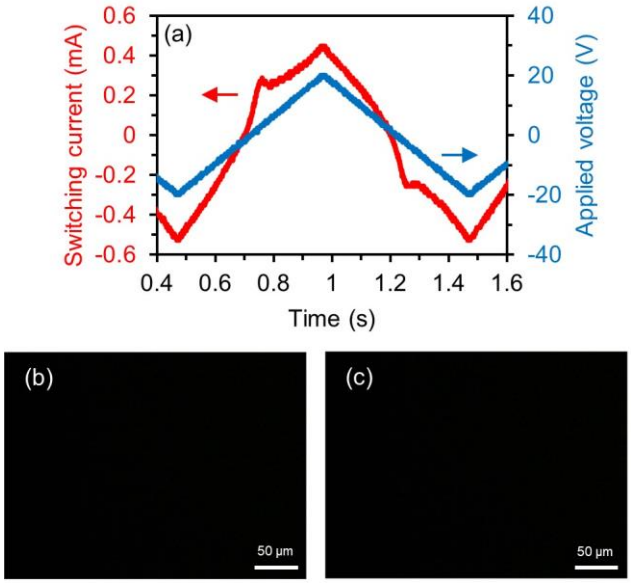

Figure 5-7. (a) Polarization reversal current for the Iso$_P$ phase at 220 °C measured by applying a triangle wave field (40 V_{pp}, 1 Hz), in a 3 μm-thick ITO-cell. (b) and (c) are the optical microscopic textures in the same cell on field-OFF and field-ON, respectively.

temperature. It is found that except near the transition temperature to other phases, the huge polarization of around 8 μCcm^{-2} is maintained in the N_F phase temperature range. The E_{th} is relatively low, 1 Vμm^{-1}.

The ferroelectric switching is also observed in the SmAP$_F$ phase (see Figure 5-6(a)). The reversal polarization is somewhat temperature dependent and is about 4.5 μCcm^{-2} as an average, which is nearly half of that of the N_F phase (see Figure 5-8). Figures 5-6(b) and (c) indicate the textures under the field-OFF and ON. On field-ON, neither of the fan-shapes of the texture nor the extinction positions change, but only the birefringence colors change from yellow to red. This characteristic texture change is attributable to the biaxial nature of the SmAP$_F$ phase composed of the bent-shaped molecules: initially, both of the molecular axis and bent (polar) direction of the bent-shaped molecules lie parallel to the cell's surface, while on field-On, the bent direction becomes perpendicular to the cell as shown in Chapters 2, 3 and 4. In this SmAP$_F$ phase, the E_{th} is increased from 1 to 3.5 Vμm^{-1} with a decrease of the temperature from 160 °C to 100 °C, which can be considered to be a thermally activated phenomenon.[20] If it is treated as having an Arrhenius-like thermal activation,[20] the pseudo-activation energy can be obtained as 28 kJmol^{-1}.

It is interesting to note that the Iso$_P$ phase still exhibits electric switching maintaining the dark texture as found in Figure 5-7(a). Although the P_s gradually decreases with the temperature, the switching behavior remains observable up to 250 °C where the thermal decomposition becomes a factor to be noticed (see Figure 5-8). The persistency of the polar structure can also be detected from the SHG and dielectric measurements as shown later.

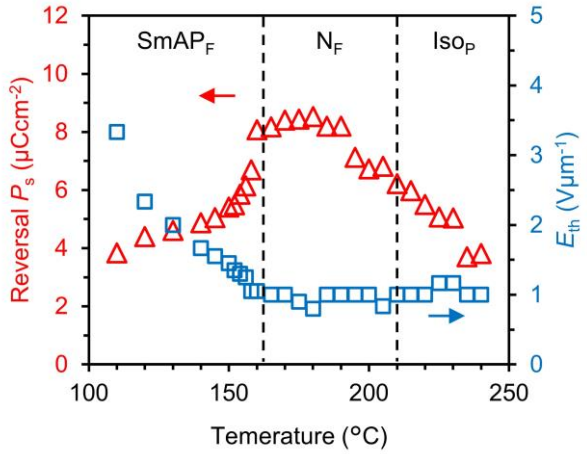

Figure 5-8. Temperature variation of the reversal P_s and E_{th} as measured in a 3 μm-thick ITO cell over a wide temperature range from 100 °C to 240 °C.

5.3.6. SHG measurements

The SHG was observed by an incidence angle of 45° to the surface of the ITO-cell, and the relative SHG intensities are plotted against the temperature in Figure 5-9. As expected, a significant SHG is observed in the N_F and $SmAP_F$ phases. Here again, the SHG activity is invariably detected in the Iso_P phase, although it disappears in the Cr phase.

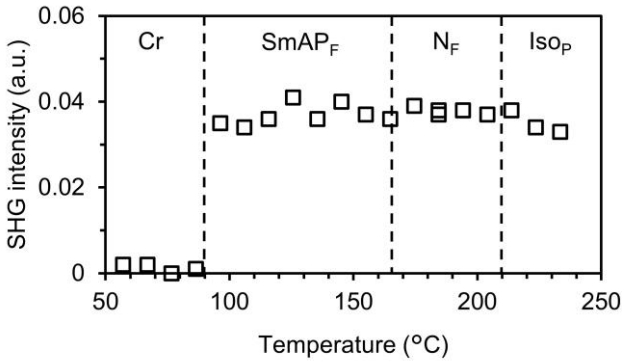

Figure 5-9. Temperature dependence of the SHG intensity observed in a 3 μm-thick ITO cell with an incident angle of 45° and without the external electric field.

5.3.7. Dielectric properties

The representative dielectric data of the N_F, $SmAP_F$ and Iso_P phases with the 3 μm thick-ITO cell are shown in Figures 5-10(a) and (b), respectively, where the real (ε') and imaginary (ε'') parts of the dielectric constants are plotted against the frequencies of 10^0 Hz to 10^7 Hz. Detailed data of the real (ε') and imaginary (ε'') parts of the dielectric constant plotted against temperature and frequency are shown in Figure 5-11.

Two relaxation modes can be observed here. One is the low-frequency (LF) mode, which is

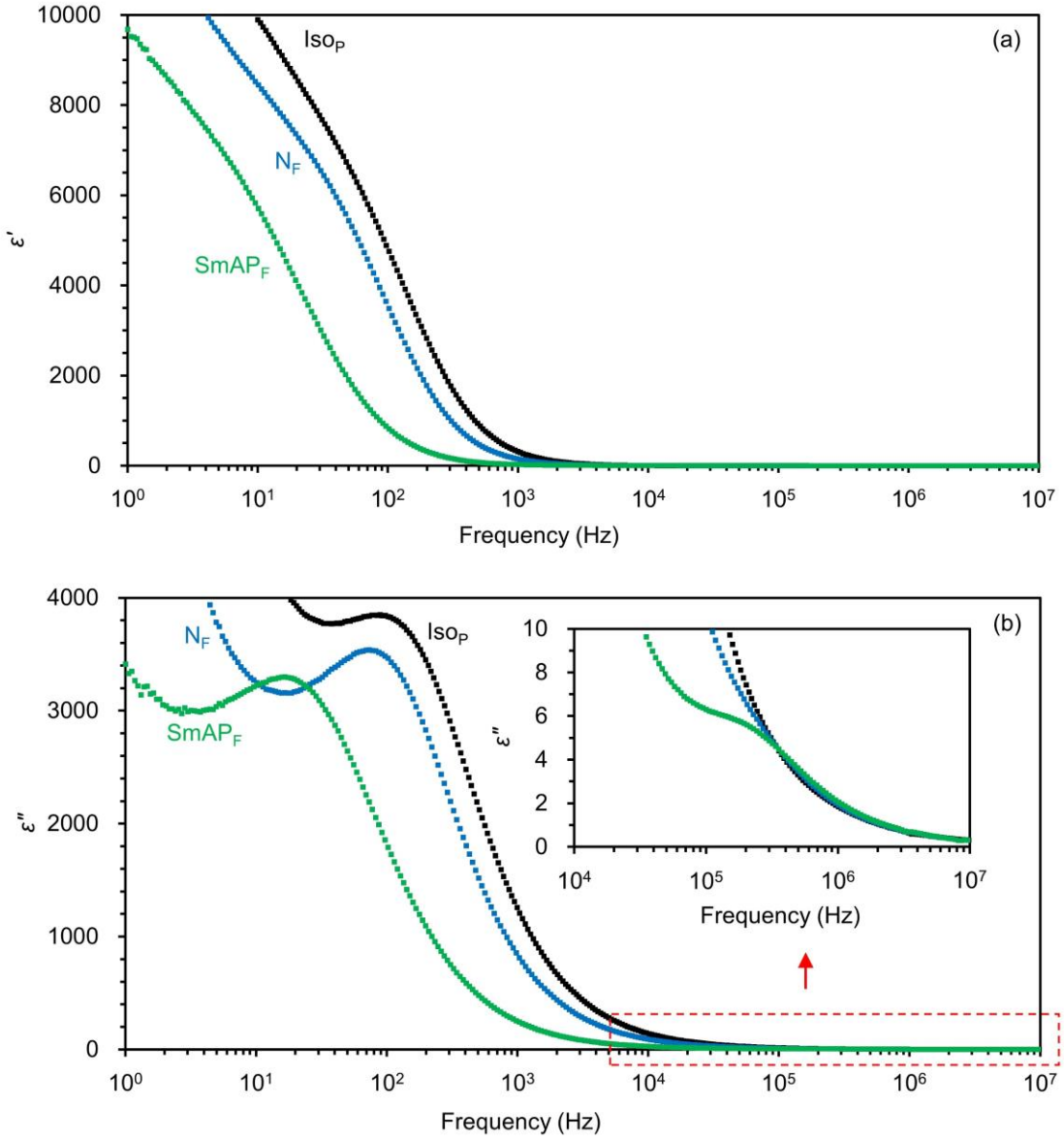

Figure 5-10. Frequency dependences of (a) the real (ε') part and (b) imaginary (ε'') part of the complex dielectric constants for the Iso$_P$ phase at 220 °C, the N$_F$ phase at 180 °C and the SmAP$_F$ phase at 120 °C from di-5(3FM-C4T), measured in a 3 μm-thick ITO-cell. In the insets, the horizontal and vertical axis are expanded to show details of the high frequency mode at around 10^5 Hz.

observed at 10~10^2 Hz in the N$_F$, SmAP$_F$ and Iso$_P$ phases. The huge dielectric constants and low relaxation frequencies (f_r) reveal that the LF mode is attributed to the collective fluctuation of polarization, which is typically observed in the ferroelectric phases.[1,11,16,21-23] Another is the high-frequency (HF) mode appearing at approximately 10^5 Hz, which is detected in the SmAP$_F$ phase (see enlarged view in the inset of Figure 5-10(b). In the N$_F$ and Iso$_P$ phases, this HF mode is likely to be buried by the large LF mode, but it becomes observable by a shift of the HF mode to the higher frequency side in the SmAP$_F$ phase. This HF mode is associated with the non-collective molecular rotation around the short axes of mesogens as commonly observed in

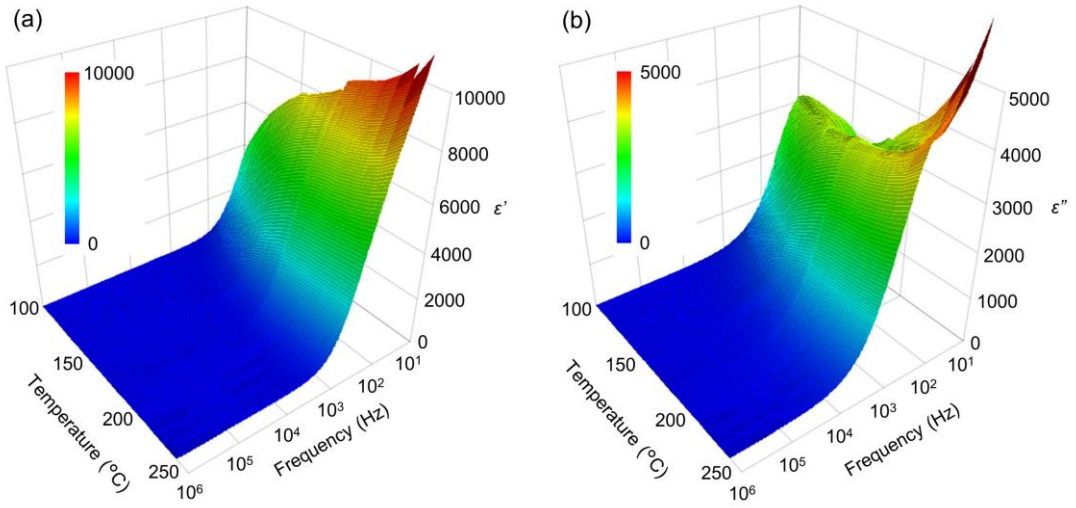

Figure 5-11. Frequency and temperature dependences of (a) the real (ε') and (b) imaginary (ε'') parts of the complex dielectric constants for the Iso_P, N_F and the $SmAP_F$ phases from di-5(3FM-C4T), measured in a 3 μm-thick ITO-cell.

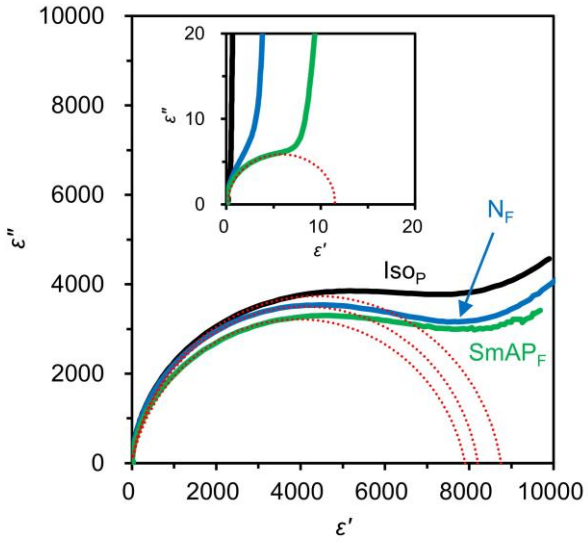

Figure 5-12. Cole-Cole plots for the Iso_P, N_F, $SmAP_F$ phases of di-5(3FM-C4T) based on the data in Figures 5-10(a) and (b). The dotted curves are obtained by fitting equation (5-1). In the insets, the horizontal and vertical axes are expanded to show details of the high frequency mode.

conventional LC phases.[21-24]

The dielectric spectra were analyzed by fitting with the following Cole-Cole equation[25]:

$$\varepsilon^* = \varepsilon' - i\varepsilon'' = \varepsilon_\infty + \frac{\Delta\varepsilon}{1 + (i\omega\tau)^{1-\alpha}} \quad 0 < \alpha < 1, \qquad (5-1)$$

where ω is the angular frequency, $\Delta\varepsilon$ (= ε_s - ε_∞) is the dielectric strength, and ε_s and ε_∞ are the "static-frequency" and "infinite-frequency" dielectric constants, respectively. $\tau = 1/(2\pi f_r)$ is the relaxation time (where f_r is the relaxation frequency), and α is the distribution parameter of relaxation time. Figure 5-12 shows the Cole-Cole plots for the LF and HF modes. The

determined parameters, $\Delta\varepsilon$, f_r and α, in the Cole-Cole equation are listed in Table 5-1. It is important to note here that the $\Delta\varepsilon$ is extremely huge (approximately 8000) for the LF collective mode of the N_F, $SmAP_F$ and Iso_P phases. It is known that a value of the $\Delta\varepsilon$ for the collective mode increases with the cell thickness.[21,23] When it is compared with cells having the same cell thickness, the $\Delta\varepsilon$ of 8000 in 3 μm-cell is larger than those reported for bent-shaped[3-5,22,23] and rod-shaped molecules.[1,9,11-13]

Figure 5-13 shows the temperature dependence of the $\Delta\varepsilon$ and f_r, respectively. Through the wide temperature zone from the $SmAP_F$ to Iso_P phases, the $\Delta\varepsilon$ is almost constant at around 8000. On the other hand, the f_r decreases with the decreasing temperature in the N_F and $SmAP_F$ phases, both of which can be considered to be a thermally activated phenomenon like standard Arrhenius one.[26,27] The Arrhenius plots reveal good linear relationships (see Figure 5-14), giving the activation energies of 13 and 45 $kJmol^{-1}$ for the N_F and $SmAP_F$ phases, respectively. These values are comparable with those obtained for other bent-core compounds.[26-30]

Table 5-1. List of the Cole-Cole parameters, $\Delta\varepsilon$, f_r and α, collected from the data in Figures 5-10 and 5-12.

	$SmAP_F$		**N_F**	**Iso_P**
	LF	**HF**	**LF**	**LF**
$\Delta\varepsilon$	7.9×10^3	12	8.2×10^3	8.8×10^3
f_r (Hz)	19	1.5×10^5	73	89
α	0.13	0	0.10	0.10

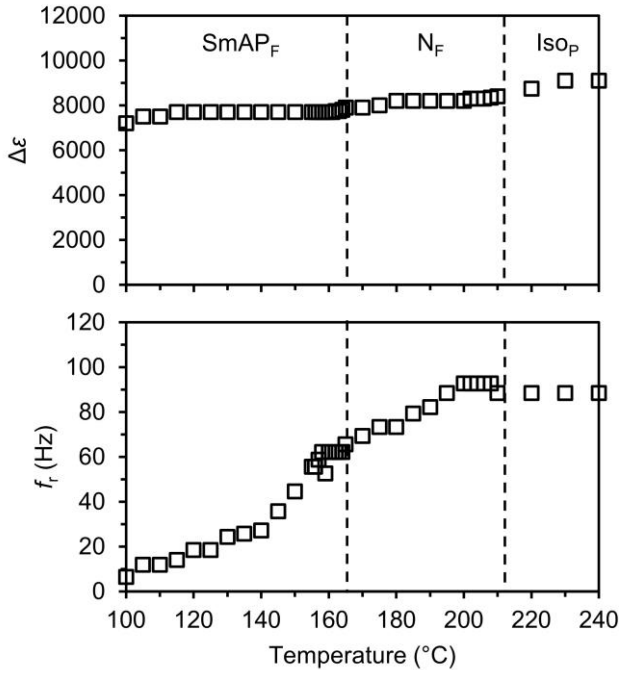

Figure 5-13. Temperature dependence of the estimated $\Delta\varepsilon$ and f_r in di-5(3FM-C4T), measured in a 3 μm-thick ITO-cell.

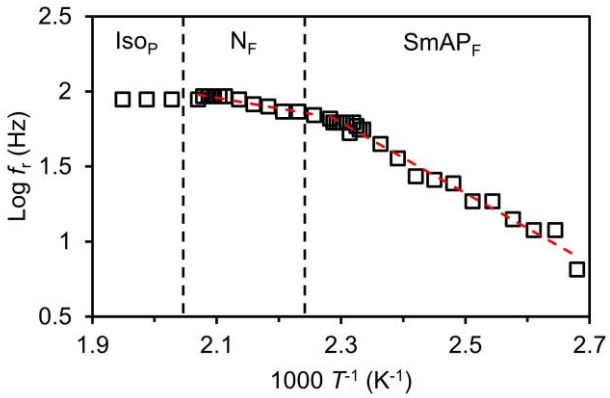

Figure 5-14. Temperature dependence of the logarithm f_r as a function of inverse absolute temperature of di-5(3FM-C4T), measured in a 3 μm-thick ITO cell. The dashed lines are guide for the eye.

Overall results clearly indicate that the nematic and smectic phases in di-5(3FM-C4) are ferroelectric. Furthermore, the polar structure is maintained even in optically isotropic liquid.

5.4. Discussion

In twin dimers, the molecular axis is not generally coincided with the axis of side-wing mesogenic cores because of the conformational constraint of the spacer alkyl chain.[31] The situation is the same in main-chain polymers.[17,18] The plausible conformation to produce the uniaxial LC order can be envisaged from conformational analysis. It has been performed on spacer group of twin dimer, X-CO-O$(CH_2)_n$O-CO-X, and main-chain polyesters having repeat unit of -[X-CO-O$(CH_2)_n$O-CO]-, where X is the aromatic mesogenic core. Spatial orientations of a given mesogenic core have been elucidated in a Cartesian coordinate system fixed to the preceding core.[16] In the LC field, the orientation angle defined by unit vectors attached to two successive rigid cores is important and has been evaluated for each conformation of the intervening flexible segment.[31] When the number of methylene units *n* in the flexible segment

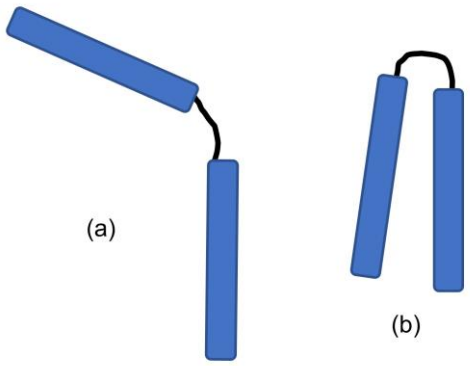

Figure 5-15. Two possible bent-shaped (a) and U-shaped (b) conformations, assumed by the twin molecules with the central alkyl spacer of odd-numbered carbons.

is even, the angle θ is found to be distributed in ranges of 0-30° (30-40 %) and 85-130° (60-70 %). In this case, hence, the conformation that comforts to the uniaxial LC field exists. When n = odd as in the present dimeric material, the major portion of the calculated angle θ (80 %) is distributed over a range of 50-90°. This is the reason why the twin dimer with n = odd assumes occasionally bent shape in the LC field as illustrated in Figure 5-15(a), forming the ferroelectric and anti-ferroelectric smectic LCs,[19,32-36] and the twist bend nematic LCs.[37-43] On the other hand, to some degree (~20%), orientations are also permitted in the angle $\theta > 160°$. In this case, one mesogenic core is folded back nearly antiparallel to the other mesogenic one (see Figure 5-15(b)). It is called U-shaped conformer, and has never been assumed by main-chain polymers and twin dimer with a pentamethylene spacer, although it sometimes appears when 3-methyl pentamethylene is used as a spacer.[44,45] U-shaped conformations were also reported for bent-shaped molecules with an o-phenylene unit within the aliphatic spacer.[46]

Keeping this conformational constraint in mind, let's speculate how the twin molecules with n = 5 can form the N_F phase with the polarization along the n-director. At first, one envisages that twin molecules taking a bent conformation form the nematic LC. It is so-called twist bent nematic LC (N_{TB}).[37-43] In the present case, however, the N_{TB} is unlikely because two mesogens within a molecule give the oppositely directed components of dipole moment along n-director, which cannot yield the polarity along the director. The plausible molecular conformation is of U-shaped one. This U-shaped molecule possesses the parallel alignment of two mesogens and then a polar head-tail character, which allows to produce the ferroelectricity as illustrated in Figure 5-16(a). Its molecular length indeed corresponds to that elucidated from the XRD observation.

The expected P_s for N_F comprising of the U-shaped molecules can be calculated as follows[47]:

$$P_s = N\mu \qquad (5-2)$$

where N is the number of dipoles per unit volume, and μ is the electric dipole moment of one-side mesogen. Since the molecule assume the U-shaped conformation, N is twice the number of molecules per unit volume. Under the assumption that the density of the N_F phase may be around 1.1 gcm^{-3}, the P_s is calculated as 5.0 μCcm^{-2}. The observed P_s of 4.3 (= 8.6 / 2) μCcm^{-2} is slightly smaller than the expected P_s.

Here, a simple question arises why the twin molecules in the nematic LC field assume the unusual U-shaped conformation, but not the bent-shaped one. If the polar association is the top priority as a consequence of interaction of the huge dipole moment,[48,49] then the answer is likely to be because only the U-shaped molecules are capable to produce the polarity along n-director in the uniaxial nematic field.

The $SmAP_F$ phase is formed from the molecules with the bent conformation in such a well-known manner that bent molecules are packed perpendicularly to the layer with the same directionality of bent (polar) direction parallel to the layer. It is illustrated in Figure 5-16(b) as elucidated from the characteristic XRD pattern of Figure 5-4(c). Only a change of the

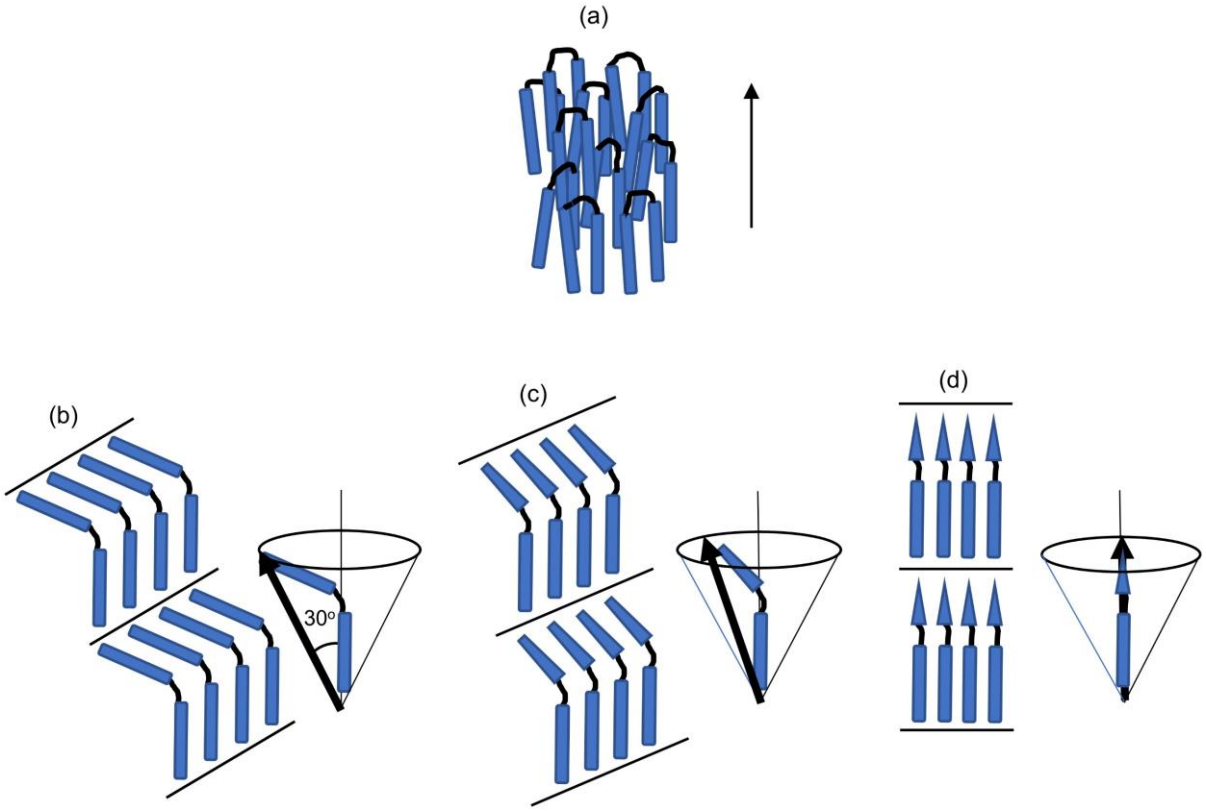

Figure 5-16. Illustrations of the molecular alignment in the N_F (a) and $SmAP_F$ phases (b)-(d), as elucidated from the XRD pattern under the magnetic field. In the N_F phase, the molecules assume U-shaped conformation with a polar head-tail character, and then uniaxially aligned with the same directionality of polarization to produce the ferroelectricity. The n-director corresponds to the magnetic field. The transformation to the $SmAP_F$ phase composed of the bent-shaped molecules occurs in such a way that the axis of one-side mesogen corresponds to the n-director of the preceding N_F phase (magnetic direction), in other words, the normal of smectic layer (solid arrow) is inclined with the azimuthal angle of 30° to the magnetic field, but in freely selected elevation direction. Then, the X-ray beam enters with different angles to the bent plane of the molecules. In (b), (c) and(d), three representative orientations corresponding to the XRD patterns of Figures 5-4(c), 5-4(d) and 5-4(c) are illustrated, respectively.

birefringence color on switching as observed in Figures 5-6(b) and (c) is due to the polar direction parallel to the layer. The reversal polarization of around 4 μCcm^{-2} is half of that (around 8 μCcm^{-2}) in the N_F phase, which is due to the halved dipole moment in the bent molecule with a bent angle of 120° in a comparison of the U-shaped molecule.

The transition of the N_F phase to the $SmAP_F$ phase is hence accompanied with the conformation change of U-like conformer to a bent-shaped one. As described above, during this transition, the XRD patterns of the $SmAP_F$ phase appear differently irrespective of uniaxial orientation of the proceeding N_F phase. This different appearance can be explained when the conformation change occurs in such a way that the axis of one of mesogen coincides to the nematic director as described in Figure 5-16(b)–(d). At this occasion, other side-wing mesogens

are inclined in a direction of the azimuthal angle of 60°, but in a freely selected elevation direction. In other words, a smectic layer structure is formed such that its layer normal lies along the azimuthal direction of 30° to the magnetic field direction. Then, the X-ray beam enters with different angles to the bent plane of molecules as described in Figures 5-16(b)–(d), leading to the various oriented patterns in Figures 5-4(c)–(e). With the X-ray beam orthogonal to the plane, the bent plane in Figure 5-4(c) lies perpendicularly to the X-ray beam, while in Figure 5-4(e), it is parallel. All other patterns including the pattern of Figure 5-4(d) are with different irradiation angles.

In the $SmAP_F$ phase, the smectic layer should be constructed by each molecule with the micro segregation of a central alkyl spacer part and an alkyl tail part, and strictly speaking, the spacing of the first layer reflection should correspond to the molecular length of around 47.0 Å.[34] However, the observed layer spacing, 23.4 Å, is half of that. The lack of the first order layer reflection is likely due to the nearly equal length of the alkyl tail and central alkyl spacer.

The Iso_P phase, in contrast to the normal isotropic phase, exhibits the electric switching and SHG activity, suggesting the polar structure. Although the reversal P_s deceases with the increasing temperature, it remains 4 μCcm^{-2} still at 240 °C, 30 °C higher than the N_F phase temperature. The collective fluctuation of polarization in the dielectric mode is invariably observed as well: the $\Delta\varepsilon$ and f_r are almost the same as those in the N_F phase. Probably, this Iso_P phase possesses some special polar aggregation of molecules in short-range domains.[50-52] The SHG detection suggests that the domain size may be larger than the wavelength of YAG laser, but no information on this has been obtained from the small-angle XRD. Here, one might have a simple question whether any transition of the Iso_P to normal Iso phase is present or not? At least in the present dimer, the polar structure is invariably detected up to 300 °C where the thermal decomposition becomes too significant to be ignored. This interesting Iso_P phase is currently being researched.

5.5. Conclusions

Di-5-(3FM-C4) with the fluorine-substituted mesogenic core as a side wing linked by pentamethylene spacer was synthesized. It is characteristic that the side wing mesogenic core has huge dipole moment of 11.23 D. This material forms three polar phases, Iso_P, N_F and $SmAP_F$ phases, as clarified from the electric switching, SHG, and dielectric measurements.

For the N_F phase, the dimeric molecules assuming U-shaped conformation behaves as polar rod-shaped molecules, and their polar association produces the polarity along n-director. The reversal P_s is approximately 8 μCcm^{-2}, which corresponds to that calculated from the dipole moment of one side mesogenic core of 11.23 D. The $SmAP_F$ phase, on the other hand, is composed of bent-shaped molecules. Hence, the transition from the N_F includes the conformational change of the molecule. XRD observation indicates that it occurs in such a way that one mesogenic axis of the bent-shaped dimeric molecule matches the n-director of the preceding N_F phase. The reversal P_s is around 4 μCcm^{-2}, half of that in the N_F phase, which also

corresponds to the value calculated from the bent-shaped conformation of the molecule. Note that this reversal P_s is the largest value among conventional bent-shaped LCs. The polarization reversal current and SHG activity are also observed in the highest temperature Iso_P phase. The reversal P_s decreases with the increasing temperature, but it remains a high value of 4 μCcm^{-2} at 240 °C, which is 30 °C higher than the N_F phase temperature. The structure analysis is still under investigation.

Three polar phases exhibit the collective polarization fluctuation mode at around 100 Hz in the dielectric measurement, giving the high dielectric constant over 8000 derived from the large dipole moment.

References

(1) Nishikawa, H.; Shiroshita, K.; Higuchi, H.; Okumura, Y.; Haseba, Y.; Yamamoto, S.; Sago, K.; Kikuchi, H. A fluid liquid-crystal material with highly polar order. *Adv. Mater.* **2017**, *29*, 1702354.

(2) McDonnell, D. G.; Raynes, E. P.; Smith, R. A. Dipole moments and dielectric properties of fluorine substituted nematic liquid crystals. *Liq. Cryst.* **1989**, *6*, 515–523.

(3) Dantlgraber, G.; Shen, D.; Diele, S.; Tschierske, C. Antiferroelectric Switchable Mesophases of Nonchiral Bent-Core Liquid Crystals Containing Fluorinated Central Cores. *Chem. Mater.* **2002**, *14*, 1149–1158.

(4) Murthy H. N. S.; Sadashiva, B. K. Influence of a fluorine substituent on the mesomorphic properties of unsymmetrical five-ring bent-core compounds. *J. Mater. Chem.* **2004**, *14*, 2813–2821.

(5) Hird, M. Fluorinated liquid crystals – properties and applications. *Chem. Soc. Rev.* **2007**, *36*, 2070–2095.

(6) Frisch, M.; Trucks, G.; Schlegel, H. B.; Scuseria, G. E.; Robb, M. A.; Cheeseman, J. R.; Scalmani, G.; Barone, V.; Mennucci, B.; Petersson, G. A., et al. Gaussian 09, revision a. 02. Wallingford (CT): Gaussian. Inc; 2009. p. 200.

(7) Mandle, R. J.; Cowling, S. J.; Goodby, J. W. A nematic to nematic transformation exhibited by a rod-like liquid crystal. *Phys. Chem. Chem. Phys.*, **2017**, *19*, 11429–11435.

(8) Mandle, R. J.; Cowling, S. J.; Goodby, J. W. Rational Design of Rod-Like Liquid Crystals Exhibiting Two Nematic Phases. *Chem. Eur. J.* **2017**, *23*, 14554–14562.

(9) Mertelj, A.; Cmok, L.; Sebastián, N.; Mandle, R. J.; Parker, R. R., Whitwood, A. C.; Goodby, J. W.; Čopič, M. Splay Nematic Phase. *Phys. Rev. X* **2018**, *8*, 041025.

(10) Chen, X.; Korblova, E.; Dong, D.; Wei, X.; Shao, R.; Radzihovsky, L.; Glaser, M. A.; Maclennan, J. E.; Bedrov, D., et al. First-principles experimental demonstration of ferroelectricity in a thermotropic nematic liquid crystal: Polar domains and striking electro-optics. *Proc. Natl. Acad. Sci. U.S.A.* **2020**, *117*, 14021–14031.

(11) Sebastián, N.; Cmok, L.; Mandle, R. J.; Fuente, M.; Olenik, I. D.; Čopič, M.; Mertelj, A. Ferroelectric-Ferroelastic Phase Transition in a Nematic Liquid Crystal. *Phys. Rev. Lett.*

2020, *124*, 037801.

(12) Manabe, A.; Bremer, M.; Kraska, M. Ferroelectric nematic phase at and below room temperature. *Liq. Cryst.* **2021**, *48*, 1079–1086.

(13) Li, J.; Nishikawa, H.; Kougo, J.; Zhou, J.; Dai, S.; Tang, W.; Zhao, X.; Hisai, Y.; Huang, M.; Aya, S. Development of ferroelectric nematic fluids with giant-ε dielectricity and nonlinear optical properties, *Sci. Adv.* **2021**, *7*, eabf5047.

(14) Mandle, R. J.; Cowling, S. J., Goodby, J. W. Structural variants of RM734 in the design of splay nematic materials. *Liq. Cryst.* **2021**, *48*, 1780–1790.

(15) Saha, R.; Nepal, P.; Feng, C.; Hossain, M. S.; Fukuto, M.; Li, R.; Gleeson, J. T.; Sprunt, S.; Twieg, R. J.; Jákli, A. Multiple ferroelectric nematic phases of a highly polar liquid crystal compound. *Liq. Cryst.* **2022**, *49*, 1784–1796.

(16) Yadav, N.; Panarin, Y. P.; Vij, J. K.; Jiang, W.; Mehl, G. H. Polar nature of the ferro-electric nematic studied by dielectric spectroscopy. ArXiv 2203.04944 (2022)

(17) Watanabe, J.; Hayashi, M.; Nakata, Y.; Niori, T.; Tokita, M. Smectic liquid crystals in main-chain polymers. *Prog. Polym. Sci.* **1997**, *22*, 1053–1087.

(18) Watanabe, J.; Hayashi, M. Thermotropic liquid crystals of polyesters having a mesogenic p,p'-bibenzoate unit. 2. X-ray study on smectic mesophase structures of BB-5 and BB-6. *Macromolecules* **1989**, *22*, 4083–4088.

(19) Watanabe, J.; Komura, H.; Niori, T. Thermotropic liquid crystals of polyesters having a mesogenic 4,4-bibenzoate unit Smectic mesophase properties and structures in dimeric model compounds. *Liq. Cryst.* **1993**, *13*, 455–465.

(20) Zhu, W.; Hayden, J.; He, F.; Yang, J.I.; Tipsawat, P.; Hossain, M.D.; Maria, J.P.; McKinstry, S.T. Strongly temperature dependent ferroelectric switching in AlN, $Al_{1-x}Sc_xN$, and $Al_{1-x}B_xN$ thin films. *Appl. Phys. Lett.* **2021**, *119*, 062901.

(21) Ozaki, M.; Yoshino, K.; Sakurai, T.; Mikami, N.; Higuchi, R. Dielectric properties of new stable ferroelectric liquid crystals with large spontaneous polarization, *J. Chem. Phys*. **1987**, *86*, 3648–3654.

(22) Zennyoji, M.; Takanishi, Y.; Ishikawa, K.; Thisayukta, J.; Watanabe, J.; Takezoe, H. Electrooptic and dielectric properties in bent-shaped liquid crystals, *Jpn. J. Appl. Phys.* **2000**, *39*, 3536–3541.

(23) Guo, L.; Gorecka, E.; Pociecha, D.; Vaupotič, N.; Čepič, M.; Reddy, R. A.; Gornik, K.; Araoka, F.; Clark, N. A.; Walba, D. M., et al. Ferroelectric behavior of orthogonal smectic phase made of bent-core molecules. *Phys. Rev. E* **2011**, *84*, 031706.

(24) Fuente, M.; Dunmur, D. Dielectric Properties of Liquid Crystals. In *Handbook of liquid crystals*, 2nd ed.; Goodby, J.; Collings, P.; Kato, T.; Tschierske, C.; Gleeson, H.; Raynes, P., Eds.; Wiley-VCH Verlag GmbH & Co KGaA: Germany, 2014; pp 1−46.

(25) Cole, K.; Cole, R. Dispersion and absorption in dielectrics I, alternating current characteristics, *J. Chem. Phys.* **1941**, *9*, 341–351.

(26) Marik, M.; Jana, D.; Majumder, K.; Chaudhuri, B. K. Dielectric behavior in B1 and B2

phases composed of unsymmetrical bent shaped liquid crystal molecules. *Mol. Cryst. Liq. Cryst.* **2015**, *606*, 111–125.

(27) Różański, S. Dielectric properties of liquid crystal formed by laterally fluorine-substituted banana-shaped molecules, *Phase Transit.* **2018**, *91*, 1007–1016.

(28) Kumar, J.; Prasad, C. Ferroelectric nematic and ferrielectric smectic mesophases in an achiral bent-core azo compound. *J. Phys. Chem. B* **2018**, *122*, 2998–3007.

(29) Turlapati, S.; Khan, R. K.; Ghosh, S.; Tadapatri, P.; Pratibha, R.; Rao, N. V. S. Existence of polar switching in the nematic and orthogonal smectic phases in novel four-ring bent-core compounds. *J. Appl. Phys.* **2016**, *120*, 174101.

(30) Salamon, P.; Eber, N.; Buka, A.; Gleeson, J. T.; Sprunt, S.; Jakli, A. Dielectric properties of mixtures of bent-core and a calamitic liquid crystal. *Phys. Rev. E* **2010**, *81*, 031711.

(31) Abe, A. Configurational aspects of the odd-even effect in thermotropic liquid crystalline polyesters. *Macromolecules* **1984**, *17*, 2280–2287.

(32) Watanabe, J.; Niori, T.; Choi, S. W.; Takanishi, Y.; Takezoe, H. Antiferroelectric Smectic Liquid Crystal Formed by Achiral Twin Dimer with Two Mesogenic Groups Linked by Alkylene Spacer, *Jpn. J. Appl. Phys.* **1998**, *37*, L401–L403.

(33) Watanabe, J.; Izumi T.; Niori, T.; Zennyoji, M.; Takanishi, Y.; Takezoe, H. Smectic mesophase properties of dimeric compounds 2 distinct formation of smectic structures with antiferroelectric ordering and frustration. *Mol. Cryst. Liq. Cryst.* **2000**, *346*, 77–86.

(34) Izumi, T.; Kang, S.; Niori, T.; Takanishi, Y.; Takezoe, H.; Watanabe, J. Smectic mesophase behavior of dimeric compounds showing antiferroelectricity, frustration and chirality. *Jpn. J. Appl. Phys.* **2006**, *45*, 1506–1514.

(35) Izumi, T.; Naitou, Y.; Tokita, M.; Watanabe, J. Frustrated smectic phase appearing as transitional state between single-layer and antiferroelectric bilayer smectic phases in binary mixtures of dimeric compounds. *Jpn. J. Appl. Phys.* **2006**, *45*, 4991–4993.

(36) Izumi T.; Naitou, Y.; Shimbo, Y.; Takanishi, Y.; Takezoe, H.; Watanabe, J. Several types of bilayer smectic liquid crystals with ferroelectric and antiferroelectric properties in binary mixture of dimeric compounds. *J. Phys. Chem. B* **2006**, *110*, 23911–23919.

(37) Dozov, I. On the spontaneous symmetry breaking in the mesophases of achiral banana-shaped molecules. *Europhys. Lett.*, **2001**, *56*, 247–253.

(38) Memmer, R. Liquid crystal phases of achiral banana-shaped molecules: a computer simulation study. *Liq. Cryst.* **2002**, *29*, 483–496.

(39) Panov, V.P.; Nagaraj, M.; Vij, J.K.; Panarin, Y.P.; Kohlmeier, A.; Tamba, M.G.; Lewis, R.A.; Mehl, G.H. Spontaneous periodic deformations in nonchiral planar-aligned bimesogens with a nematic-nematic transition and a negative elastic constant. *Phys. Rev. Lett.* **2010**, *105*, 167801.

(40) Beguin, L.; Emsley, J. W.; Lelli, M.; Lesage, A.; Luckhurst, G. R.; Timimi, B. A.; Zimmermann, H. *J. Phys. Chem. B* **2012**, *116*, 27, 7940–7951.

(41) Henderson, P.A.; Imrie, C.T. Methylene-linked liquid crystal dimers and the twist-bend

nematic phase. *Liq. Cryst.* **2011**, *38*, 1407–1414.

(42) Cestari, M.; Diez-Berart, S.; Dunmur, D.A.; Ferrarini, A.; de la Fuente, M.R.; Jackson, D.J.B.; Lopez, D.O.; Luckhurst, G.R.; Perez-Jubindo, M.A.; Richardson, R.M.; et al. Phase behavior and properties of the liquid-crystal dimer 1″,7″-bis (4-cyanobiphenyl-4′-yl) heptane: A twist-bend nematic liquid crystal. *Phys. Rev. E* **2011**, *84*, 31704.

(43) Kang, S.; Lee, E.; Li, T.; Liang, X.; Tokita, M.; Nakajima, K.; Watanabe, J. Two-Dimensional Skyrmion Lattice Formation in a Nematic Liquid Crystal Consisting of Highly Bent Banana Molecules. *Angew. Chem. Int. Ed.* **2016**, *55*, 11552–11556.

(44) Naito, Y.; Ishige, R.; Itoh, M.; Tokita, M.; Watanabe, J. Smectic A Formation by Twin Dimers Assuming U-shaped Conformation. *Chem. Lett.* **2008**, *37*, 880–881.

(45) Ishige, R.; Tokita, M.; Naito, Y.; Zhang, C.Y.; Watanabe, J. Unusual Formation of Smectic A Structure in Cross-Linked Monodomain Elastomer of Main-Chain LC Polyester with 3-Methylpentane Spacer. *Macromolecules* **2008**, *41*, 2671–2676.

(46) Rahman, M. D.; Biswas, T. K.; Sarkar, S. M.; Yusoff, M. M.; Malek, M. N. F. A.; Tschierske, C. New U-shaped liquid crystals azobenzene derived from catechol for photoswitching properties. *J. Mol. Liq.* **2015**, *202*, 125–133.

(47) Peercy, P. S. Measurement of the “soft” mode and coupled modes in the paraelectric and ferroelectric phases of KH_2PO_4 at high pressure, *Phys. Rev. B* **1975**, *12*, 2725– 2740.

(48) M. Born. Über anisotrope Flüssigkeiten. Versuch einer Theorie der flüssigen Kristalle und des elektrischen Kerr-Effekts in Flüssigkeiten. Sitzungsber. *Preuss. Akad Wiss.* **1916**, *30*, 614–650.

(49) Yu, C. J.; Yu, M.; Lee, S. D. Phase Diagram for Ferroelectric Nematic Ordering of Hard Spherocylinders with Longitudinal Dipoles. *Jpn. J. Appl. Phys.* **2002**, *41*, L102–L104.

(50) Stinson, T. W.; Lister J. D.; Pretransitional phenomena in the isotropic phase of a nematic liquid crystal. *Phys. Rev. Lett.* **1970**, *25*, 503.

(51) Gennes, P. G. Short Range Order Effects in the Isotropic Phase of Nematics and Cholesterics. *Mol. Cryst. Liq. Cryst.* **1971**, *12*, 193–214.

(52) Phuong, N. H.; Schmid, F.; Local structure in nematic and isotropic liquid crystals. *J. Chem. Phys.* **2003**, *119,* 1214.

CHAPTER 6

General Conclusions

In the following, the results obtained in each chapter of this thesis are summarized, and the molecular design for the dielectric strength ($\Delta\varepsilon$) and spontaneous polarization (P_s) enhancement in the bent-shaped dimeric molecules are proposed.

In Chapter 1, "General Introduction", it was stated that high $\Delta\varepsilon$ and P_s are essential for the realization of high-performance flexible electrochemical devices using ferroelectric liquid crystals (LCs). By reviewing the conventional research on ferroelectric LCs, the bent-shaped dimeric molecules were selected from the viewpoint of the variety of LCs alignment structures and the low temperature of the LCs phase, and the significance of the research for the establishment of the molecular design in high $\Delta\varepsilon$ and P_s was shown.

In Chapter 2, “Huge Dielectric Constants of the Ferroelectric Smectic-A Phase in Bent-Shaped Dimeric Molecules”, in order to grasp the $\Delta\varepsilon$ of the ferroelectric phase in the bent-shaped dimeric molecules and obtain the molecular design for the $\Delta\varepsilon$ enhancement, the dielectric relaxation properties of the ferroelectric smectic-A ($SmAP_F$) phase formed by mixtures of bent-shaped dimeric molecules with different alkyl chain lengths was analyzed. The $SmAP_F$ phase exhibited a collective mode with cooperative dipole orientation at about 500 Hz. The $\Delta\varepsilon$ increases dramatically with increasing LC cell thickness. It exceeds 7000 for a 50 μm-thick cell, which is much higher than the $\Delta\varepsilon$ reported for the other bent-shaped molecules. As the cell thickness increases, the LC domain size increases. This means that the number of interacting dipole moments is increasing. From this result, it is clarified that the highly cooperative orientation of the dipole moment in the bent-shaped dimeric molecules brings about a huge $\Delta\varepsilon$.

In Chapter 3, “Electric Switching Behaviors and Dielectric Relaxation Properties in Ferroelectric, Antiferroelectric and Paraelectric Smectic Phases of Bent-Shaped Dimeric Molecules”, in order to obtain the molecular design for the $\Delta\varepsilon$ enhancement, the relationship between the dielectric relaxation properties and electrical switching behaviors in the $SmAP_F$, antiferroelectric smectic-A ($SmAP_A$) and antiferroelectric smectic-C (SmC_AP_A) phases was analyzed. In the $SmAP_F$ phase, a small threshold electric field (E_{th}) of less than 1 $V\mu m^{-1}$ for ferroelectric switching is characteristic and the E_{th} decreases with increasing cell thickness. In dielectric measurements, a collective mode appears at a low frequency of about 500 Hz and has a large $\Delta\varepsilon$ over 1500 in a 3 μm-thick cell. The $\Delta\varepsilon$ greatly depends on the cell thickness, and

increases up to 10000 in a 80 μm-thick cell, while the collective mode frequency decreases from 500 Hz to 200 Hz. In the $SmAP_A$ phase, although the E_{th} is higher than in the $SmAP_F$ phase, still low at about 2 $V\mu m^{-1}$ for a 3 μm-thick cell. A similar cell thickness dependence is also observed, with the E_{th} decreasing to 0.6 $V\mu m^{-1}$ for an 80 μm-thick cell. In the dielectric measurements, the $SmAP_A$ phase is a cell thickness dependence similar to the $SmAP_F$ phase, with the $\Delta\varepsilon$ increasing to 200 for the 3 μm-thick cell and 2000 for the 80 μm-thick cell. Another antiferroelectric phase, the SmC_AP_A phase, has the E_{th} of 10 $V\mu m^{-1}$ in a 3 μm-thick cell and a very low $\Delta\varepsilon$ of 8. A plot of the obtained $\Delta\varepsilon$ versus the reciprocal E_{th} revealed that all the data were on a straight line. The lower E_{th} (i.e., the energy barrier between the two polar states) enhances the cooperative orientation of the dipoles, resulting in higher $\Delta\varepsilon$.

In Chapter 4, "Spontaneous Polarization Characteristics in Polar Smectic Phases of Fluoro-Substituted Bent-Shaped Dimeric Molecules", in order to obtain the molecular design for the P_s enhancement, three types of the bent-shaped dimeric molecules are synthesized by fluorine substitution on the mesogenic unit and, the effect of fluorine substitution on the polar smectic phase was analyzed. The fluorine-substituted dimeric molecules form the $SmAP_F$ and SmC_AP_A phases, respectively, depending on the fluorine-substituted position. The fluorine substitution lowers the transition temperature by 10-30 °C without significantly changing the temperature range of the smectic phase. This behavior is speculated to be due to a decrease in intermolecular force. The fluorine substitution can also increase the dipole moment of the molecule. The estimated dipole moments of the one-sided mesogens in the non-fluorinated dimeric molecule (C16), the two fluorinated dimeric molecule (2F-Y-C16) and the four fluorinated dimeric molecule (4F-XY-C16) are 5.99, 6.85 and 7.94 D, respectively. Furthermore, the reversal P_s of C16, 2F-Y-C16 and 4F-XY-C16 were 0.64, 1.64 and 2.42 μCcm^{-2}, respectively. A clear proportional relationship was observed by plotting the obtained P_s against the dipole moment of the one-sided mesogen. From this result, it was clarified that fluorine substitution to the mesogenic unit increases the dipole moment of the molecule, resulting in a high P_s value.

In Chapter 5, "Three Distinct Polar Phases, Isotropic, Nematic and Smectic-A Phases Formed from Fluoro-Substituted Dimeric Molecule with Large Dipole Moment", a novel dimeric molecule with large dipole moment was developed to enhance the P_s and $\Delta\varepsilon$. A dimeric molecule, di-5(3FM-C4T), with fluorine-substituted mesogenic cores as side wings connected by a pentamethylene spacer was synthesized and demonstrated for the P_s and $\Delta\varepsilon$. Due to effective fluorine substitution, the mesogenic core has a huge dipole moment of 11.23 D. From polarization switching, second harmonic generation and dielectric measurements, it was found to form the $SmAP_F$, ferroelectric nematic (N_F) and polar isotropic (Iso_P) phases. The N_F phase is composed of U-shaped molecules that behave like rod-shaped molecules. The P_s is about 8 μCcm^{-2}, reflecting the huge dipole moment of the mesogenic core. On the other hand, the $SmAP_F$ phase is formed by bent-shaped molecules. The N_F-$SmAP_F$ phases transition has a structural change from a rod-shaped to a bent-shaped molecule, which is induced by a pentamethylene spacer in the dimeric molecule. The P_s of the $SmAP_F$ phase is about 4 μCcm^{-2},

which is half that of the N_F phase as expected from the bent-shaped molecule, but is the highest among conventional bent-shaped LC molecules. The highest temperature Iso_P phase still exhibits the polar structure and may have polar aggregations of molecules in small domains. Three polar phases were found to have a high $\Delta\varepsilon$ of 10000 reflecting the huge dipole moment and the oriented structure.

From the above, it is important to increase the dipole moment, increase the number of interacting dipole moments, and decrease the E_{th} for the ferroelectric switching as the molecular design for the huge $\Delta\varepsilon$. Furthermore, it is suggested that increasing the dipole moment is important as the molecular design for huge P_s. The dipole moment, which is common to the $\Delta\varepsilon$ and P_s enhancement, is effectively increased by substituting the highly electronegative fluorine used in this thesis in the director direction of the molecule.

Acknowledgments

This study was carried out in Sone & Chang Laboratory at Tokyo Institute of Technology. Numerous people have contributed to this study.

First, I deeply thank Professor Masato Sone, Professor Junji Watanabe, Professor Hiroki Ishizaki, Associate Professor Tso-Fu Mark Chang, and Associate Professor Sungmin Kang for their precise advice and continuous encouragement.

Further, I deeply thank Professor Takaaki Manaka for the precise advice of SHG analysis. I deeply thank Professor Masatoshi Tokita for usage of XRD and the triangular wave voltage device. I would also like to thank Materials Analysis Division, Open Facility Center, Tokyo Institute of Technology, for NMR measurement, element analysis, DSC analysis. I would like to express my gratitude to Dr. Yasukazu Yoshida of LG Japan Lab Co., Ltd. for allowing to me carry out this study and for the encouragement.

Lastly, I express thanks to my wife, parents and children for their deep encouragements and support throughout the study.

Publication Lists

Papers included in This Thesis

1. **Shigemasa Nakasugi**, Sungmin Kang, Junji Watanabe, Hiroki Ishizaki, Masato Sone. Huge dielectric constants of the ferroelectric smectic-A phase in bent-shaped dimeric molecules. *Mater. Adv.*, **2021**, *2*, 7017-7023.
2. **Shigemasa Nakasugi**, Sungmin Kang, Junji Watanabe, Masato Sone, Hiroki Ishizaki. Dielectric Relaxation Behavior of Schiff Base Dimeric Molecules. *IEEJ Trans. Fundam. Mater.*, **2022**, *142*, 152-158.
3. **Shigemasa Nakasugi**, Sungmin Kang, Tso-Fu Mark Chang, Hiroki Ishizaki, Masato Sone, Junji Watanabe. Electric Switching Behaviors and Dielectric Relaxation Properties in Ferroelectric, Antiferroelectric, and Paraelectric Smectic Phases of Bent-Shaped Dimeric Molecules. *J. Phys. Chem. B* **2022**, *126*, 4967-4976.
4. **Shigemasa Nakasugi**, Sungmin Kang, Tso-Fu Mark Chang, Takaaki Manaka, Hiroki Ishizaki, Masato Sone, Junji Watanabe. Spontaneous Polarization Characteristics in Polar Smectic Phases of Fluoro-Substituted Bent-Shaped Dimeric Molecules. *J. Phys. Chem. B* **2022**, *126*, 8119-8127.
5. **Shigemasa Nakasugi**, Sungmin Kang, Tso-Fu Mark Chang, Takaaki Manaka, Hiroki Ishizaki, Masato Sone, Junji Watanabe. Three Distinct Polar Phases, Isotropic, Nematic and Smectic-A Phases Formed from Fluoro-Substituted Dimeric Molecule with Large Dipole Moment. *J. Phys. Chem. B* **2023**, *127*, 6585-6595.

Other Papers

1. K. Fu, **S. Nakasugi**, Y. Takagahara, L. Li, T. Hayakawa, M. Jikei, M. Tokita, M. Kakimoto, J. Watanabe. Synthesis of New Type of Dendritic Molecule and its Columnar Self-Assembly Having a Potential as Molecular Cavity. *J. Mol. Struct.*, **2005**, *739*, 125-130.
2. Teruaki Hayakawa, **Shigemasa Nakasugi**, Masaaki Kakimoto, Masatoshi Tokita, Junji Watanabe. Synthesis and characterization of self-assembling amphiphilic aromatic amide dendrons. *High Perform Polym*, **2006**, *18*, 761-775.
3. Jin Li, Ide Yasuaki, **Shigemasa Nakasugi**, Motoki Misumi, Hiroshi Yanagita, Fumihiro Suzuki, Georg Pawlowski, JoonYeon Cho, Huirong Yao, Takanori Kudo, Munirathna Padmanaban, YoungJun Her, Yi Cao. A chemical underlayer approach to mitigate shot noise in EUV contact hole patterning. *Proc. SPIE*, **2014**, *9051*, 905117.
4. Go Noya, Yusuke Hama, Maki Ishii, **Shigemasa Nakasugi**, Takanori Kudo, Munirathna Padmanaban. Planarization of topography with spin-on carbon hard mask. *Proc. SPIE*, **2016**, *9779*, 97791.

Domestic Conference

1. 中杉 茂正, 高河原 康子, 李 莉, 寺境 光俊, 早川 晃鏡, 柿本 雅明, 付 凱, 渡辺 順次. 両親媒性芳香族ポリアミドデンドロンの合成と構造特性. 第 53 回高分子学会年次大会, 2004 年 5 月.
2. 中杉 茂正, 高河原 康子, 李 莉, 寺境 光俊, 早川 晃鏡, 柿本 雅明, 付 凱, 渡辺 順次. 両親媒性芳香族アミドデンドロンの合成と自己組織化構造の構築. 第 53 回高分子学会討論会, 2004 年 9 月.
3. 中杉 茂正, 高河原 康子, 李 莉, 寺境 光俊, 早川 晃鏡, 柿本 雅明, 付 凱, 戸木田 雅利, 渡辺 順次. 両親媒性芳香族アミドデンドロンの合成と自己組織化構造の形成. 第 13 回日本ポリイミド・芳香族系高分子会議, 2004 年 11 月.
4. 中杉 茂正, 高河原 康子, 李 莉, 付 凱, 寺境光俊, 戸木田 雅利, 早川 晃鏡, 渡辺 順次, 柿本 雅明. 両親媒性芳香族アミドデンドロンの合成と自己集合構造の形成. 第 54 回高分子学会年次大会, 2005 年 5 月.
5. 中杉 茂正, 姜 聲敏, 渡辺 順次, 石崎 博基, 曽根 正人. 二量体分子における強誘電性スメクチック-A 相の誘電緩和挙動. 令和 3 年電気学会基礎・材料・共通部門大会, 2021 年 9 月.
6. 石崎 博基, 孝治 慎之助, 中杉 茂正. 疎水性イオン液体/可塑剤重量比における PVC-Gel アクチュエータ特性に及ぼす影響. 令和 3 年電気学会基礎・材料・共通部門大会, 2021 年 9 月.